Development of A Novel Ultra-High Vacuum Diffusion Apparatus for Investigating Knudsen Diffusion in Complex Pore Channels

Haiyue Yu

Submitted in part fulfilment of the requirements for the degree of

Doctor of Philosophy at University College London

Department of Chemical Engineering

University College London

2021

Declaration

I, Haiyue Yu, confirm that the work presented in this thesis is my own. Where information has been derived from other sources, I confirm that this has been indicated in the thesis.

…………………………

Signature

…………………………

Date

Abstract

Disordered porous materials with rough surfaces are widely used in several industrial applications, such as fuel cells, heterogeneous catalysis, molecular separation, and oil and gas recovery. Many of these processes are diffusion-controlled, due to narrow pore size. In porous catalysts, molecules diffuse through the pore network and react on the active sites of the pore walls. This indicates that the shape and surface morphology of the pores may affect catalytic performance. Knudsen diffusion plays a crucial role in catalysts where gaseous molecular transport is dominated by molecule–wall collisions. Consequently, the pore geometry of disordered porous materials, including the pore shapes and pore wall roughness, has attracted significant research interest. However, the high cost and limited availability of techniques for building a system that can simulate the Knudsen regime in complex pores with rough inner surface representative of porous catalysts have hindered the practical investigation of the effect of the pore morphology on Knudsen diffusion.

In this study, to address these limitations and accurately measure the Knudsen diffusivity in complex pore channels, a unique vacuum diffusion apparatus was designed and employed. The inherent characteristics of the novel apparatus enabled the system to rapidly simulate the Knudsen regime, emulating the complexity of actual porous media, and to accurately measure the relevant data for calculations. In addition, this high-vacuum diffusion apparatus was used to investigate Knudsen diffusion in complex pore channels with various lengths, pore shapes, and surface roughness. The measurement of the Knudsen diffusivity in the channels with various lengths and shapes was guided by computer simulations and theoretical calculations to validate the functioning and the accuracy of the apparatus. Three fractal surface channels (with $N = 1$, 2, and 3 generations) were fabricated using a three-dimensional printer *via* selective laser sintering, and the effect of the surface roughness of the fabricated channels on the Knudsen diffusion can be analysed in the unique apparatus. The

developed ultra-high vacuum diffusion apparatus enables us to experimentally probe Knudsen diffusion in complex geometries more directly than has ever been achieved.

Impact statement

The modelling of catalyst geometries has emerged as a crucial research field in the study of porous catalysts. In the past 30 years, researchers have employed computational simulations and analytical calculations to investigate the effect of a catalyst geometry on the Knudsen diffusivity, to analyse its effects on product distributions and yields during heterogeneous catalysis. Although these calculations provide theoretical insights, no practical design tools have been developed to directly demonstrate the effect of catalyst geometry on Knudsen diffusion at the nanoscale. This is complicated by the fact that the geometry, including the pore shape, surface morphology, and network topology, of real porous materials is intricate at multiple length scales.

To obtain direct insight on the effect of catalyst geometry on Knudsen diffusion, in this study, a novel ultra-high vacuum diffusion apparatus (UHV-DA) was successfully designed and constructed. This unique apparatus enabled the accurate control of pressure to simulate the Knudsen regime. In addition, a rapid prototyping technique (three-dimensional (3D) printing) was employed to realise complex controlled geometrical environments in the apparatus. The high vacuum conditions provided by the apparatus enabled the accurate testing of the effect of the catalyst geometry on the Knudsen regime using precise manipulation. The obtained results could be directly compared to those of analytical calculations.

The developed apparatus provides the tool to investigate the fundamentals of Knudsen diffusion in complex pore channels. During the experimental measurements, the activities in a disordered porous material under low-pressure conditions were simulated on a macroscopic scale. In addition, 3D-printed macroscopic models of a fractal pore and other complex porous media were fabricated. The experiments enables the validation of the Knudsen diffusion theory in realistic, rough fractal pores, for the first time.

Acknowledgements

On 19 February 2015, I sent an email to "m.coppens@ucl.ac.uk" hoping to hear back about the possibility to study at UCL as a PhD student, and I received my answer on 25 February 2015 less than a week. A month later, I submitted my application to UCL, received the offer within two months and identified me as a member of Centre for Nature Inspired Engineering at UCL until today. For this incredible experience that followed, I would like to give sincere thanks to my supervisor, Professor Marc-Olivier Coppens, for giving me this opportunity to being a PhD student with a great project. It is no exaggeration to say that his expertise, enthusiasm and view of the big picture made me who I am now. I appreciate his kind help and support in both my research work and my PhD life.

I would like to thank my research group, Centre for Nature Inspired Engineering, for giving me uninterruptible academic support in the past 4 years. It was my honour to work with so many brilliant and nice people, Kaiqiao Wu, Zhiyi Meng, Han Wu and other people in CNIE, who gave me unconditional help during my study. I would also like to thank Sander Baltussen and Simon Barrass, for all the technical guidance and support they have provided for which I will never forget. I would like to thank Sienna Griffin-Shaw and Martyn Carter for the professional help and suggestions that they provided on 3D printing in Bartlett, UCL.

Finally, I thank my family. Mom and Dad, thank you for giving me unconditional love and financial support. I know all the sacrifice you have made for me. You used to make me proud, and I hope I can make you proud in the future. My darling Junjing, thank you to accept me in your life, be your husband and become a father. I can't describe how fortunate I was to meet you. Your encouragement and trust make me overcome difficulties with full of confidence. You and our daughter light up my life. Thank you, my family, from bottom of my heart, and own you a debt of gratitude and love.

Contents

List of figures

List of tables

CHAPTER

ONE

1 Introduction

The physics of diffusion in disordered porous media has attracted much interest because of its considerable importance to industrial processes, such as heterogeneous catalysis, shale gas exploitations, molecular separations, and oil recovery [1-3]. In heterogeneous catalysis, the molecules diffuse through the pore network and react on the active sites of the pore walls, indicating that geometrical disorder of the pore structure may affect the observed catalytic results. This is because the geometrical disorder of these systems significantly affects molecular transport processes that occur inside the pore network [4]. In meso-porous materials (defined as having a pore diameter between 2 and 50 nm, according to IUPAC [5]), Knudsen diffusion, a type of diffusion that occurs when the mean free path of the molecules is much larger than the pore diameter, is often the predominant transport mechanism for gases. Thus, molecule-wall collisions dominate molecular transport. Therefore, the effect of pore geometry including pore shape and pore wall roughness interest us to investigate, where the studies should be carried out in the Knudsen regime.

In 1909, Knudsen first studied the motion of rarefied gases through a long cylindrical tube, where molecular transport occurs as a result of the collision between gas molecules and the tube wall, rather than intermolecular collisions [6]. In 1910, Smoluchowski demonstrated the effect of pore shape on what became known as

Knudsen diffusion [7]. Another milestone in the description of Knudsen diffusion was attained by Clausing in 1930 [8]; he studied the transmission probability, which is the probability of molecules moving from one side to another in the tube, as a function of tube length. Based on these pioneers' research, an increasing number of researchers have investigated Knudson diffusion in porous media using both experimental and numerical approaches [9, 10], particularly the effect of geometrical complexities on Knudsen diffusion in porous media [11-16].

Despite a significant number of results demonstrating the geometrical effect on Knudsen diffusion, direct experimental insight into the effect of pore surface roughness on Knudsen diffusion in porous media has never been obtained. This may be because of the complexity of actual porous media, in which the effects of pore shape, surface roughness, and pore connectivity are combined. However, modelling suggests the significant effects of pore structures on Knudsen diffusion [4, 17]. Such theoretical results can form the basis for comparison with carefully designed experiments on model pores or porous media to validate the theory. Therefore, we conducted experiments that emulate processes that occur in disordered nanoporous media on a macroscopic scale using a specially designed high vacuum system and 3D-printed channels to investigate features of complex porous media, such as fractal pores. This high-vacuum setup enabled us to validate the Knudsen diffusion theory in complex geometries more directly than has ever been previously conducted.

1.1 Overview of diffusion

Diffusion phenomena correspond to the movement of substances from a region of high concentration to one of low concentration. Already in the early 19th century, they were acknowledged to be related to Brownian motion [18]. However, precise quantitative measurement of diffusion phenomena is difficult, compared with qualitative observation. The first systematic quantitative study of diffusion was performed by Graham in 1829 [19], who focused on gas diffusion. In 1867, Maxwell continued the studies on gaseous diffusion and derived the CO_2 diffusion coefficient in air [20].

Another milestone in diffusion history was achieved when Fick proposed fundamental diffusion laws in 1855, termed the famous first and second Fick's laws [21]. Graham and Fick revealed that gas diffusion was much faster than liquid diffusion. In the early 20th century, the classic atomistic theory of diffusion was developed by Einstein [22]. In Einstein's theory of diffusion, he derived the diffusion equation from a molecular picture of Brownian motion instead of Fick's macroscopic laws, showing that the mean-square displacement of molecules in a fluid is proportional to time and the diffusion coefficient. Based on the conclusions of these pioneers, an increasing number of analytical calculations, quantitative measurements, and computational simulations have been applied to investigate diffusion phenomena in different scenarios [3, 16, 23, 24].

1.2 Gas diffusion in porous media

The diffusion of gas molecules in porous media is a fundamental topic in several fields, such as civil engineering, soil science, pharmaceutical science, and chemical engineering [25-27]. Over the past few decades, numerous theoretical calculations, computational simulations, and experimental investigations have been conducted on gas diffusivity in different porous media [23].

Gas diffusion in porous media involves molecular interactions between gas molecules and collisions between gas molecules and pore walls, which, crucially, depend on features of the diffusing gas species and the intrinsic structure of the porous media [28]. When gas molecules travel through a porous medium with sufficiently wide pores (wider than a few molecular diameters), two main diffusion mechanisms, molecular and Knudsen diffusion, occur and their relative contribution is quantified by the Knudsen number (Kn). The Knudsen number is defined as the ratio of the gas mean free path length to the characteristic length:

$$Kn = \frac{\lambda}{L} \tag{1.1}$$

where L is the characteristic length and λ is the gas mean free path. The latter is the average distance of a molecule traveling between two successive collisions, which can

be calculated according to the kinetic theory of gases using:

$$\lambda = \frac{k_B T}{\sqrt{2}\pi d_{gas}^{2} p}$$
(1.2)

where d_{gas} is the effective diameter of a gas molecule, p is the total pressure, k_B is the Boltzmann constant (1.3807×10^{-23} J/K), and T is the thermodynamic temperature (K).

When Kn is significantly smaller than 0.01, the interactions between gas molecules become a predominant factor, with less frequent collisions occurring with the pore walls, which reflects molecular diffusion. In this regime, Knudsen diffusion becomes negligible compared with other types of diffusion, and the gas is considered to be a continuous medium. When Kn is greater than 10, the gas dynamics are dominated by molecular collisions with the pore walls rather than by intermolecular collisions [29]. Molecular diffusion becomes relatively negligible, which results in Knudsen diffusion. When Kn is in the range of 0.01 and 10, both molecular and Knudsen diffusion govern the transport of the gas molecules; this represents the transition regime. According to Equation 1.2, Kn can also be used to categorise the flow regimes in porous media (Figure 1.1).
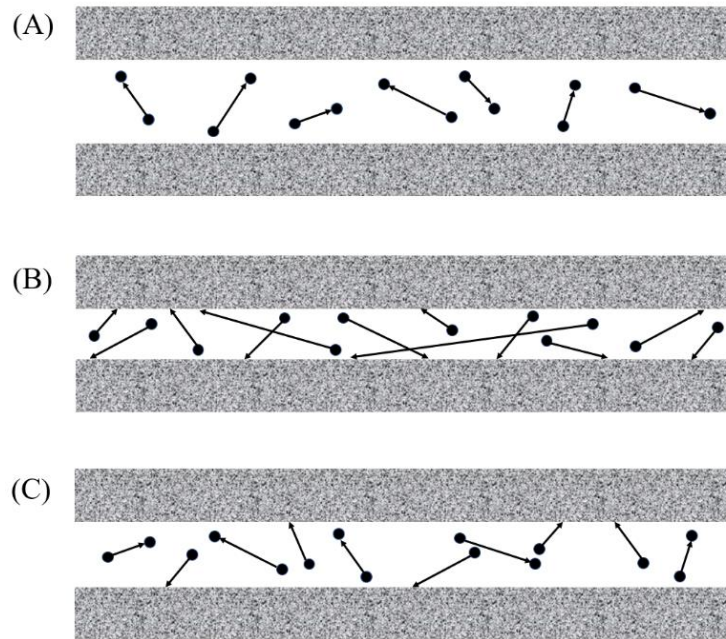
Figure 1.1 Diffusion regime in porous media: (A) molecular diffusion regime, with collisions occurring between molecules; (B) Knudsen diffusion regime, dominated by collisions between molecules and pore walls; (C) transition regime, in which both intermolecular and molecule-wall collisions contribute to the overall diffusion.

1.3 Molecular diffusion

Molecular diffusion is produced by Brownian motion, resulting in the continuum regime, which refers to the relative motion of different gas species. When the mean free path of gas molecules is much smaller than the pore diameter, molecular diffusion constitutes the entire diffusion process. The rate of this diffusion is a function of the temperature and properties of the diffusing particles. Molecular diffusion in porous media occurs in several crucial applications, such as the oil industry, food products, and soil science [1]. Understanding the fundamental mechanisms of molecular diffusion in porous media is essential to optimise product or process performance in these applications.

Fick's laws are typically applied to evaluate gas diffusion in non-porous media, whereas the Stefan-Maxwell equations are used for multi-component diffusion [30]. Although

they are strictly applicable to non-porous media, Fick's laws can also be applied to porous media by introducing correction factors that depend on the porous medium [31]. Fick proposed two laws [21, 32]. The first one describes the relationship between the gas diffusive flux and the concentration gradient under steady-state conditions. The second law relates the concentration gradient to the unsteady diffusive flux, and it was initially applied for non-porous media only.

Fick's first law can also be presented using the chemical potential

$$J = \frac{-Dc}{RT}\frac{d\mu}{dx} \tag{1.3}$$

where D is the diffusion coefficient in the bulk with unit of m^2·s^{-1}, c is the concentration with unit of mol·m^{-3}, μ is the chemical potential with unit of J·mol^{-1}, R is the gas constant with unit of J·K^{-1}·mol^{-1}, T is the temperature with unit of K, x is the diffusion path with unit of m, and J is the flux of the diffusing species with unit of mol·m^{-2}·s^{-1} (an index denoting the diffusing species is omitted here for simplicity).

Fick's second law depicts the effects of concentration changes with time and can be expressed, for a component in an ideal mixture, using Equation 1.4:

$$\frac{\partial c}{\partial t} = D\frac{\partial^2 c}{\partial x^2} \tag{1.4}$$

The previously discussed forms of Fick's laws are only appropriate in the bulk. Fick's first law can also be applied to porous media with modifications, which results in the effective diffusion coefficient correlating to the porosity and tortuosity [33], as shown in Equation 1.5:

$$D_{eff} = \frac{\phi}{\tau}D \tag{1.5}$$

where D_{eff} is the effective diffusion coefficient in porous media, which is defined as the ratio of the average flux to the average concentration gradient [34], ϕ is the porosity of the porous medium, and τ is the tortuosity of the porous medium.

1.4 Knudsen diffusion

1.4.1 Introduction

Knudsen diffusion is also called free molecular flow [35], in which the mean free path of gas molecules is larger than the pore diameter, and the collisions of gas molecules with pore walls become the dominant mechanism. The molecular flux owing to free molecular diffusion can be presented by a generalisation of Fick's first law:

$$J_K = -D_K \frac{dc}{dx} \tag{1.6}$$

where D_K is the Knudsen diffusion coefficient. The Knudsen diffusion coefficient can be estimated using Equation 1.7 for a cylindrical pore [6]:

$$D_K = \frac{d_p}{3} \bar{v} \tag{1.7}$$

where d_p is the mean pore diameter of the porous medium and $\bar{v}$ is the mean speed of the gas molecules. According to the kinetic theory of gases, the diffusivity of Knudsen diffusion can be expressed as

$$D_K = \frac{d_p}{3} \sqrt{\frac{8RT}{\pi M}} \tag{1.8}$$

where M is the molecular weight of the diffusing species. Comparing D_K with the diffusion coefficient of molecular diffusion, the Knudsen diffusion coefficient is not related to the absolute pressure according to Equation 1.8, and is only a function of mean pore size, temperature, and molecular properties. Generally, for heterogeneous reactions in porous media, the conditions of absolute pressure or pore diameter can be between bulk diffusion and Knudsen diffusion, and they can be estimated using Equation 1.9 [33], which is Bosanquet's approximation [36]

$$\frac{1}{D^*} = \frac{1}{D_K} + \frac{1}{D} \tag{1.9}$$

where D^* is the diffusion coefficient in the transition regime. In practice, Knudsen diffusion is only applied to gaseous diffusion, as the mean free path of liquid molecules is very small [37]. Additionally, the Knudsen diffusion phenomena are directly related to the pressure and pore diameter, and they frequently occur in small-diameter pores or under low-pressure conditions according to Equation 1.2.

1.4.2 Knudsen diffusion in porous media

As Knudsen diffusion is often the dominant mechanism for gas transport in mesoporous materials used in catalysis and other applications, it has attracted much interest. The initial theory for Knudsen diffusion was proposed by Knudsen in 1909, on the basis of studies of the motion of a rarefied gases through a long cylindrical tube as a result of the collision between gas molecules and tube walls rather than intermolecular collisions [6]. Although his experiments were for tubes with a circular cross-section, he derived Equation 1.10 for tubes with arbitrary cross-sections:

$$D_K = \frac{4}{3} \frac{\Omega}{P_{peri}} \sqrt{\frac{8RT}{\pi M_i}} \tag{1.10}$$

where Ω is the cross-sectional area, P_{peri} is the perimeter of the cross-section, and M_i is the molecular weight for the i-th species. Following Knudsen's initial research for a long cylindrical tube, an increasing number of studies have used theoretical and numerical simulations to investigate Knudsen diffusion in porous media. The map of pressures and pore diameters corresponding to the Knudsen regime is shown in Figure 1.2
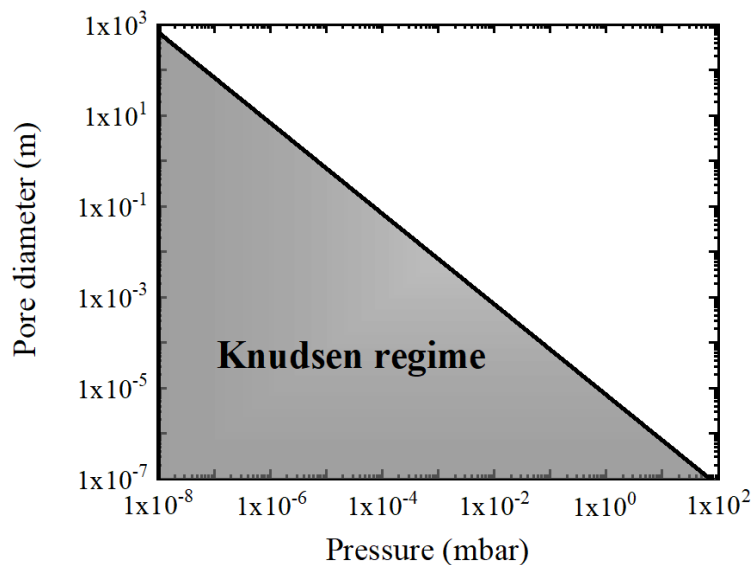
Figure 1.2 Map of pressures and pore diameters corresponding to the Knudsen regime. The boundary is determined by Equations 1.1 and 1.2, assuming nitrogen at ambient temperature (293.15 K). The shadow area represents the Knudsen regime with a Knudsen number larger than 10.

1.4.2.1 Analytical approaches

A year after Knudsen's initial publication, Smoluchowski demonstrated that Knudsen's formula (Equation 1.9) was not always correct and could even result in zero diffusivity for a fixed area with an infinite perimeter, which is counterintuitive. He derived a formula for Knudsen diffusion in a cylindrical tube with a cross-section with an arbitrary shape [7]. In 1932, Clausing defined an important concept, transmission probability, which represents the probability of molecules moving from one side to another [8]. Additionally, Knudsen diffusivity can be easily derived from the transmission probabilities [4]. Moreover, this statistical concept was extensively used in kinetic Monte Carlo simulations from the 1960s on. Additionally, Clausing confirmed Knudsen's assumption that the direction of a molecule leaving the tube's surface follows Lambert's cosine law on the basis of thermodynamic arguments [38]. Based on Clausing's calculation, Dushman proposed an analytical formula to calculate the transmission probability through a rapid, although less accurate estimate [39]. In

1977, Cole recalculated Clausing's approximation, obtained highly accurate results, and summarized the transmission probability in different channels of different shapes [40]. His results are widely used as a reference in physics and vacuum technology. A few years later, Lafferty collected and compared all previously calculated data in his book 'Foundations of Vacuum Science and Technology', which is considered an indispensable resource in the rarefied gas field [41].

Based on these fundamental calculations, in 1961, Evans, Watson and Mason discussed the uniform-pressure diffusion in porous media from the continuum regime to the Knudsen regime [24]. These authors considered porous media as uniformly distributed 'dust' particles to analyse the system using the classical kinetic theory of multicomponent mixtures and to obtain results for diffusion in porous media. In 1965, Wakao and co-workers derived equations to study the pressure gradient effect on different diffusion regimes in a single capillary [42]. The calculated results were in good agreement with experimental data. Kast and Hohenthanner systematically summarized and calculated mass transfer within porous media in various transport modes including continuum, transition, and Knudsen flow [43].

1.4.2.2 Numerical approaches

In 1960, Davis first applied Monte Carlo simulations to investigate the effects of tube structures on Knudsen diffusion [44]. Various shapes of pipes were tested, and the results indicated that a straight cylindrical tube provided the largest transmission probability compared with other geometrical tubes of the same length. Evans et al. later used Monte Carlo simulations to simulate the Knudsen diffusion of gases in a porous solid and predicted the Knudsen diffusivity where the pore properties, including porosity and mean pore size, are known [11].

Over the past few decades, many studies have focused on the effect of geometry on Knudsen diffusion in porous media using Monte Carlo simulations. In 1987, Nakano et al. compared Knudsen diffusion in pores with different types of pore walls: concave,

convex, and cylindrical [12]. Knudsen diffusivities were obtained and significantly affected by the configuration of the pore wall. Burganos and Payatakes investigated gaseous diffusion in pores using converging–diverging geometry and calculated the Knudsen diffusivities in constricted pores using a Monte Carlo simulation [13]. Tomadakis and Sotirchos applied Monte Carlo simulations to study gaseous diffusion in random capillary structures [14]. Unlike analytical approaches, which are only limited to simple structures, to avoid intractable calculations, a numerical approach *via* Monte Carlo simulations can be applied to geometrically complex structures to investigate Knudsen diffusion in more realistic models of porous media.

1.4.3 Knudsen diffusion in fractal pores

After more than a century of investigations, many unsolved problems still exist for Knudsen diffusion in porous media. One of the crucial problems is the effect of pore surface irregularity on Knudsen diffusion. Generally, the pores are represented as cylindrical or spherical channels, and the surface morphology is considered to be smooth. However, actual pore surfaces are rarely smooth, but could be very rough, like a molecular version of the Norwegian coastline (Figure 1.3), with its many fjords [45, 46].

Figure 1.3 Map of Norway including part of Sweden and Finland. Adapted from [47]

Knudsen diffusion is a result of collisions between gas molecules and pore surfaces. Thus, a molecule can enter a fjord (surface irregularity) before colliding with the pore wall [48]. Thereafter, this molecule can either move deeper within a fjord for more collisions or leave the fjord to return to the main pore channel (Figure 1.4). As a result, the residence time for a molecule in a porous medium with surface irregularity will be statistically longer than that in a smooth medium. Therefore, the effect of the actual surface morphology can affect Knudsen diffusion [49].
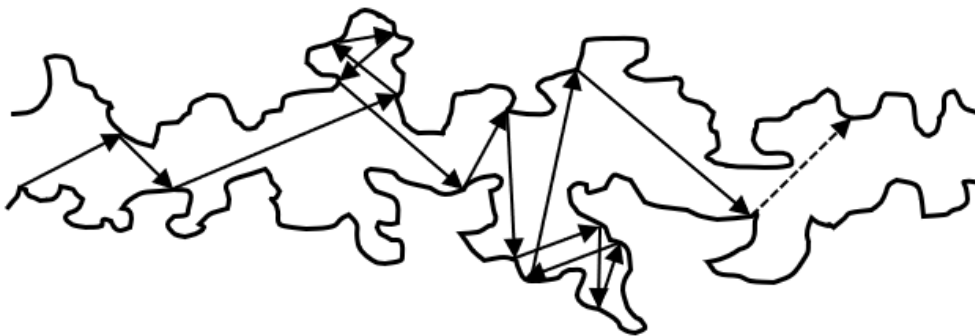
Figure 1.4 Knudsen diffusion in rough pore. Adapted from [50]

1.4.3.1 Fractal geometry

The irregularity of pore surfaces can be easily observed using electron microscopy. To systematically investigate the effect of the irregularity of surfaces on Knudsen diffusion, fractal geometry should be introduced.
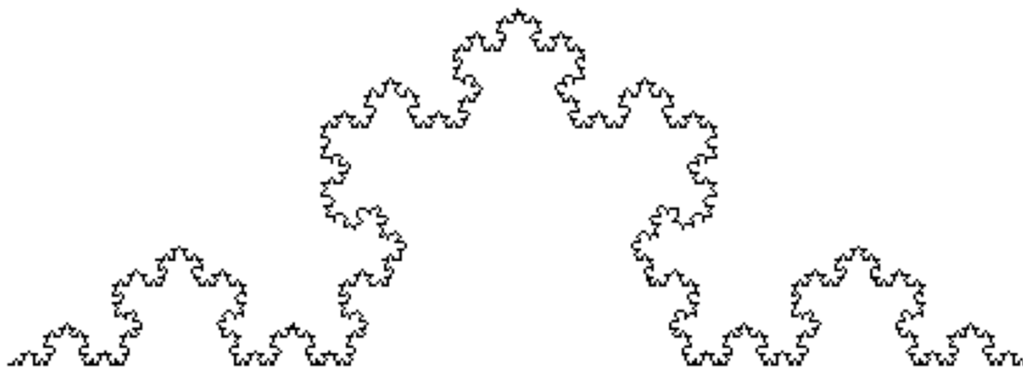
Figure 1.5 Example of a fractal object: a Koch curve [51]

Based on research from the 1950s on, the famous mathematician Benoit Mandelbrot introduced fractal geometry in 1975 to describe irregularly shaped objects in nature, such as coastlines, trees, mountains, etc. [52-54]. He found that these had more akin with mathematical objects that were previously deemed obscure aberrations, like Koch curves or Cantor sets, than with Euclidean objects, like straight lines or cones. Roughly speaking, a fractal is a set with repeatedly similar features across different scales of magnification. Such sets have a so-called fractal dimension that is generally non-integer; it is higher than the topological dimension (0 for a point, 1 for a line, 2 for a surface) and at most the Euclidean dimension of the space they are embedded in (2 for planar objects or 3 for spatial object). A generalised concept of dimension for arbitrary sets was introduced by the German mathematician Felix Hausdorff in 1918 [55], and can be generally applied to fractals, where fractional values are obtained. Fractal dimension is a fundamental parameter to quantitatively characterize fractals as a ratio of the change in detail to the change in scale [53].

Pioneering research by Avnir and Pfeifer observed that the internal surfaces of many porous amorphous materials are similar to fractal coastlines at the molecular scale [56]. Materials with fractal surface features could be formed by an iterative mechanism, like mathematical fractals, but within a finite scaling range [46]. Their studies suggested that fractal geometry could be applied to systematically investigate the effects of surface irregularity on processes in porous media, like diffusion, adsorption and reaction [57].

1.4.3.2 Fractals in porous media

Most of the diffusion studies involving fractal concepts before the 1990s primarily focused on diffusion on or in fractal media, i.e., objects that are fractal themselves. In 1991, Elias-Kohav et al. employed fractal structures as model materials to investigate diffusion-controlled processes [58]. Adler and Thovert summarized the features of fractal porous media and investigated single-phase transport in 1993 [59]. Cai and Sorensen experimentally determined the effect of the morphological properties of a fractal aggregate on diffusivities in the Knudsen regime using static and dynamic light

scattering [60].

The study of the effect of fractal surface morphology on Knudsen diffusion in porous media was underappreciated for many years until 1993. Coppens and Froment analytically predicted the effect of fractal surface morphology on Knudsen diffusion [61]. In 1998, Santra and Sapoval calculated weak effects of fractal surface roughness on Knudsen diffusion in two-dimensional (2D) porous systems [62]. In 2001, Malek and Coppens investigated the effect of pore surface roughness on both self- (gradientless) and transport diffusion (with concentration gradient) in the Knudsen regime in mesoporous media through dynamic Monte Carlo simulations in three-dimensional (3D) rough fractal pores [4]. The results indicated that self-diffusion is roughness-dependent, whereas transport diffusion (or, at least, the transmission probability) is not. In 2006, Coppens and Dammers explained that the transport diffusivity should be the same as the self- diffusivity and roughness dependent, while the transmission probability should be roughness independent [63].

Many studies focused on Knudsen diffusion in pores with a fractal surface over the past two decades, primarily using the Monte Carlo method to simulate diffusion processes. Experimental validation of the effect of fractal surface roughness in the Knudsen regime is still very rare and difficult to achieve. To address this gap and gain more direct insights into the effects of fractal surface roughness on diffusion in the Knudsen regime, at the level of individual pores, a unique measurement system should be designed and constructed.

1.5 Scope of the thesis

The beginning of this thesis has reviewed established theories on gas diffusion in porous media, including molecular diffusion and Knudsen diffusion. Additionally, the literature perspectives on the fractal concept in porous media have been introduced in this chapter. Subsequently, the mechanism of experimentally achieving Knudsen diffusion is presented to translate the theoretical model to an actual physical model. By adjusting the pressure, the dimension of experimental validation can be scaled up from

the nano- to the macroscale to maintain the same diffusion regime. Therefore, vacuum technology has been crucial for this project, and the basic concepts and calculations of vacuum technology are introduced in Chapter 2.

In Chapter 3, the conceptual and practical designs are described to provide a crude design of a vacuum system for Knudsen diffusion measurements based on the theoretical knowledge and empiricism of vacuum technology. In Chapter 4, with the preliminary design, analytical and numerical calculations are conducted to provide more precise predictions for system performance based on actual data. This procedure can significantly minimise unnecessary costs, assist the practical design, and avoid empirical errors during the design process. Chapter 5 presents the integration of the designed vacuum system and highlights the calibrations of the crucial components in the system. In Chapter 6, the Knudsen diffusion coefficient measured using the high vacuum system is described and compared with numerical simulations using COMSOL Multiphysics and pioneering analytical calculations to indicate the accuracy of the system in the Knudsen regime. By changing different geometrical tubes including varying the lengths and tube shapes, the effect of pore length and shape on Knudsen diffusion was investigated and compared with the simulation results.

Chapter 7 presents an investigation of surface roughness. All completed 3D printing-related studies, including the design of the 3D-printed fractal model, fabrication, and vacuum testing, are described and discussed. Although further experimental investigations of Knudsen diffusion in surface roughness pores by the high vacuum system were difficult to complete because of the COVID-19 pandemic, numerical simulations of the roughness effect on Knudsen diffusion were carried out. Finally, a research summary with an outlook on the directions of future research is presented in the concluding chapter.

In summary, this dissertation presents an experimental design of an ultra-high vacuum system to precisely measure the diffusivity and evaluate the geometrical effects on Knudsen diffusion. The system was designed based on the theoretical and mechanistic

understanding of vacuum technology (Chapter 2 to Chapter 5). It was used to evaluate the Knudsen diffusion process under different geometrical conditions (Chapter 6) and eventually aimed to validate the effect of fractal surface roughness in the Knudsen regime (Chapter 7).

CHAPTER

TWO

2 Vacuum technology

As mentioned in Chapter 1, the aim of this thesis was to gain further insight into the effects of geometry on Knudsen diffusion at the level of individual pores. Therefore, the first step in achieving Knudsen diffusion experimentally is to translate a mathematical model from theoretical concepts into an actual physical model on which measurements can be performed. To produce a physical model that represents the mathematical one, the dimensions are scaled up from the nano- to the macroscale, while maintaining the same diffusion regime by adjusting the system pressure, to maintain the ratio between the dimensions of the pore and the mean free path of a gas molecule in the Knudsen regime. Calculated using Equation 1.2, the system pressure must be decreased to below 10^{-4} mbar when the pore size is scaled up to the centimetre level, where the ratio of gas mean free path to pore size is greater than 10, corresponding to the Knudsen regime. As a result, the physical model should be placed in a high-vacuum system to attain the Knudsen regime. Considering the effect of outgassing, the system should be evacuated as much as possible to achieve a pure Knudsen regime. In this chapter, the basic concepts and analytical calculations in vacuum technology are explained.

2.1 Introduction

The concept of vacuum has been studied scientifically since at least the 17th century [64]. The word 'vacuum' has Latin roots [65], and it means 'empty' or 'void'. A perfect vacuum can be described as a space with no particles of any state, including solid, liquid, gas, etc. Achieving a perfect vacuum is practically impossible. Currently, vacuum science has a critical function in many fields, such as physics, chemistry, mechanical engineering, chemical engineering, and astronautics [66]. It is also an essential aspect of many industrial processes, such as mass spectroscopy, gas chromatography, and semiconductor manufacturing [67-69]. In addition, vacuum technology has a large effect on the development and implementation of handling technologies [70].

The broad definition of a vacuum is the pressure of a gas in a closed system being lower than the surrounding atmospheric pressure. Many units of measurement are used, and although the SI unit is the Pascal (Pa), the bar (10^5 Pa) and mbar (10^2 Pa) are often used in vacuum technology [71]. Air is a mixture of gases and contains approximately 10^{25} molecules per cubic meter at 1 bar. To attain a vacuum state, the gas molecules should be removed from the system. As a consequence, the pressure in this system is very low, containing only a small number of particles. In theory, an absolute vacuum should not have any particles in the system, and the pressure should equal zero. However, practically, these conditions are impossible to attain. The vacuum is generally defined as 4 categories in vacuum technology, depicted in Table 2.1.

Table 2.1 Category of vacuum technology [72]

Category	Pressure	Unit	Applications
Rough vacuum	$10^3 - 1$	mbar	Handling technology
Medium vacuum	$1 - 10^{-3}$	mbar	Steel degassing
High vacuum	$10^{-3} - 10^{-7}$	mbar	Electron tube manufacture
Ultra-high vacuum	$10^{-7} - 10^{-14}$	mbar	Particle accelerator

2.2 Basic vacuum concepts

2.2.1 Throughput

Throughput (Q) is defined as the volume of a gas at a known pressure (p) moving through a plane in a known time, and it is considered to be the gas flow rate at a constant temperature. In vacuum technology, the throughput is also called the gas load, with SI units Pa·m^3·s^{-1}.

$$Q = \frac{d(pV)}{dt} \tag{2.1}$$

where p is the pressure of a gas moving through a plane, with unit of Pa; V is the volume of a gas, with unit of m^3; and Q is the throughput with unit of Pa·m^3·s^{-1}. Furthermore, the pressure multiplied by volume is the unit of energy, which indicates that the throughput can be considered to be the flow of energy per unit time, i.e., power. Hence, the throughput indicates the power required for a vacuum system. From the definition of throughput, it can be expressed using the volumetric flow rate at a constant pressure (Equation 2.2).

$$Q = p \cdot V' \tag{2.2}$$

where V' is volumetric flow rate with unit of m^3·s^{-1}. In a vacuum system, all gases follow the ideal gas law, and the volumetric flow rate is expressed by Equation 2.3:

$$V' = \frac{m'RT}{pM} \tag{2.3}$$

where m' is the mass flow rate with units of kg·s^{-1}. Consequently, Q can be converted to the mass flow (Equation 2.4).

$$Q = \frac{m'RT}{M} \tag{2.4}$$

2.2.2 Conductance

When gases flow through a system, gas flow is frequently hindered by the friction from the collision of the gas molecules with the walls. Analogous to the electrical resistance, flow resistance (W) reveals itself *via* a reduced gas flow rate and pressure differences. Instead of flow resistance, its reciprocal, conductance, is generally used in vacuum technology. Conductance is the characteristic of a vacuum system that permits the flow of gas, and it represents the volumetric flow rate. In 1962, Dushman first introduced the concept of conductance [73], which is defined as:

$$C = \frac{Q}{p_u - p_d} \tag{2.5}$$

where C is the conductance with unit of L·s^{-1}, p_u is the upstream pressure with unit of Pa, and p_d is the downstream pressure with unit of Pa. Conductance is analogous to electrical conductance, with Q being the analogue of current and pressure difference being the analogue of voltage difference. Furthermore, if this analogy is applied to a set of components in series, the net conductance is expressed by the relationship

$$\frac{1}{C_{total}} = \frac{1}{C_1} + \frac{1}{C_2} + \cdots + \frac{1}{C_n} \tag{2.6}$$

Additionally, if they connected in parallel, the conductance becomes

$$C_{total} = C_1 + C_2 + ... + C_n \tag{2.7}$$

2.2.3 Pumping speed

Pumping speed is another important concept in vacuum technology. Denoted by S_p, it is defined as the gas volume flowing through the pump inlet port per unit time; therefore, the SI unit of pumping speed is volume per unit time (m^3·s^{-1}). Pumping speed is independent of pressure for many vacuum pumps. Thus,

$$Q = p \cdot S_p \tag{2.8}$$

Owing to the flow resistance caused by vacuum components, the net pumping speed is not always equal to the pumping speed provided by the manufacturer. Thus, the concept of effective pumping speed is introduced, which is defined as the net pumping speed limited by the conductance (Equation 2.9). The pumping speed provided by the manufacturer (S_{manu}) and the conductance of the connection between the vacuum pump and the chamber (C) determine the effective pumping speed (S_{eff}), as follows:

$$\frac{1}{S_{eff}} = \frac{1}{S_{manu}} + \frac{1}{C} \tag{2.9}$$

Therefore, the pumping speed and components' conductance must be considered beforehand when designing a vacuum apparatus. Selecting the proper vacuum components and correct calculation of conductance can result in a system quickly attaining the pressure required, becoming more economical, and minimizing energy use.

2.2.4 Contamination

The chambers and connections in the vacuum system must be as clean as possible during its installation, otherwise the unintended impurities would significantly increase pumping time and lead to a too high ultimate pressure. Contamination is an important topic in vacuum technology, and it can be divided into three categories [74, 75]:

- Contaminant gas loads
- Residual contaminants (seals, grease, and screws)
- Application-related contaminants (process reaction products)

In a well-designed vacuum system, contaminant gas loads are always the dominant contaminant sources. The different contaminant gas loads should be considered under different vacuum regimes (Table 2.2).

Table 2.2 Contaminant gas load for different vacuum range

Vacuum level	Gas loads
Atmospheric	Air
Medium vacuum	Water
High vacuum	Water, CO, H_2
Ultra-high vacuum	H_2, CO, CO_2, CH_4

Water vapour is always the main contaminant gas load for most scenarios in a vacuum system. More than 80% of the water is still left even when the air has been evacuated from the vacuum system, in which water molecules remain adsorbed at the walls [41]. However, these water molecules can be removed through system bake-out and a continuous decrease in the pressure. In these scenarios, CO and H_2 become the predominant gas loads.

Additionally, the vacuum chambers and connections in the system must be grease-free. All seals must be carefully selected. When O-rings are used as seals in the vacuum system, the contaminants trapped within the bulk can gradually diffuse into the chamber. Thus, O-rings must be installed completely dry, and pre-treatment is essential. During the assembly process, clean powder-free and lint-free gloves are essential.

2.3 Fundamental equations of the vacuum system

A vacuum pump has two primary tasks in the vacuum system: evacuating the system from atmospheric pressure to a specified pressure within a relatively short time and maintaining the specified pressure for a certain time. Both tasks result in entirely different requirements for the pumps. In this section, the basic vacuum system calculations are explained as fundamental knowledge for the system design in Chapter 3.

2.3.1 Effective pumping speed

An elementary idealised vacuum system is considered here to derive general design

equations. A schematic diagram of the general chamber-pump vacuum system is shown in Figure 2.1. A vacuum pump is connected to a chamber of volume $V_{chamber}$ at a constant pressure p through a vacuum unit (flange, tube, etc.) with conductance C.
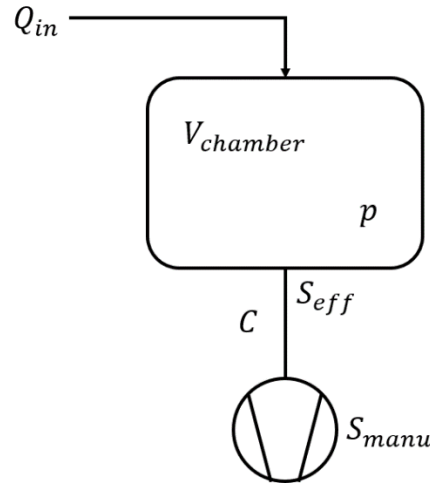
Figure 2.1 Schematic diagram of a general chamber-pump vacuum system. A vacuum pump with pumping speed of S_{manu} is connected to a chamber of volume $V_{chamber}$ at a constant pressure p through a vacuum unit (flange, tube, etc.) with conductance C, leading to an effective pumping speed for the vacuum chamber, S_{eff}. Q_{in} represents the gas inlet sources, including outgassing, leakage, and process gas.

As mentioned in Section 2.2.3, the effective pumping speed (S_{eff}) can be calculated using the pumping speed provided by the manufacturer (S_{manu}) and the conductance of the connection unit (C) through Equation 2.9. Hence, the fraction of the speed of a vacuum pump can be derived as

$$\frac{S_{eff}}{S_{manu}} = \frac{1}{1 + \frac{S_{manu}}{C}} \tag{2.10}$$

The effective pumping speed strongly depends on the conductance between the vacuum chamber and vacuum pump, which must be sufficiently large to avoid the pumping speed being lost. However, considering practical and economic factors, the conductance of the connection unit should be at least larger than the pumping speed (Figure 2.2).

Hence, the ratio between S_{eff} and S_{manu} should be larger than 0.5, indicating a potential election of vacuum flanges and connection units between the chamber and pumps.
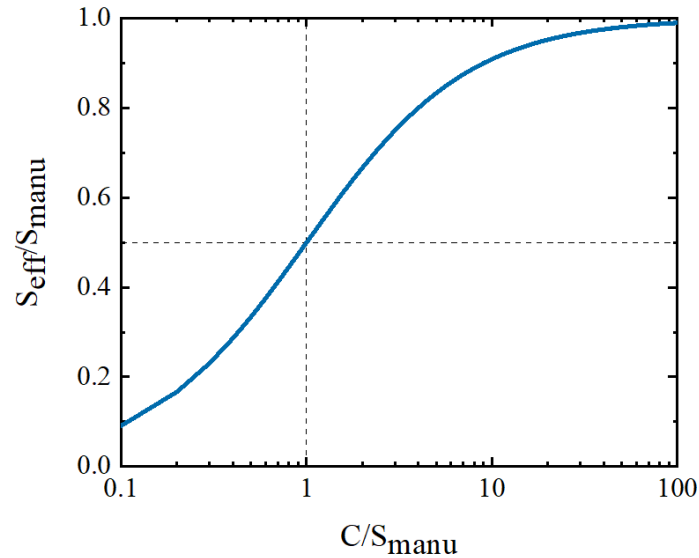
Figure 2.2 Relative pumping speed as a function of the relative conductance between the vacuum chamber and pumps

2.3.2 Pump-down time

To derive the basic pump-down equations, the gas flow (Q_{in}) is considered. Q_{in} consists of outgassing, leaking, initial gas, and purposely processed gas. The details of different sources of gas in a high vacuum system are discussed in Section 2.3.3. The time dependence of the system pressure can be calculated using a differential equation:

$$V \frac{dp}{dt} = Q_{in} - Q_{out} \tag{2.11}$$

where p is the pressure in the constant-volume chamber (Figure 2.1), and Q_{out} is the gas flow pumped out from the chamber using a vacuum pump with unit of $Pa \cdot m^3 \cdot s^{-1}$:

$$Q_{out} = p \cdot S_{eff} \tag{2.12}$$

In actual systems, the pumping speed is a function of the pressure and time during the start-up of the vacuum pump. The flow is time- and pressure-dependent during

outgassing. If the pumping speed and gas flow are assumed constant, then the following expression is obtained (Equation 2.13).

$$p(t) = (p_0 - \frac{Q_{in}}{S_{eff}}) \cdot \exp(-\frac{S_{eff}}{V} t) + \frac{Q_{in}}{S_{eff}}$$

(2.13)

If we neglect the purposely introduced gas flow into the system and evitable leaking, $\frac{Q_{in}}{S_{eff}}$ should be significantly smaller than the system pressure; thus, the gas contained in the vacuum system is removed and the pressure decreases exponentially with time from the atmospheric value, p_0

$$p(t) = p_0 \cdot \exp(-\frac{S_{eff}}{V} t)$$

(2.14)

The general predicted pump-down time from p_0 (atmosphere) to p is

$$t = \frac{V}{S_{eff}} \cdot \ln(\frac{p_0 - \frac{Q_{in}}{S_{eff}}}{p - \frac{Q_{in}}{S_{eff}}})$$

(2.15)

According to these equations, we can estimate the pump-down time before ordering the vacuum components. Figure 2.3 is an example of the pressure–time curve of a vacuum chamber with a volume of 10 L equipped with a vacuum pump with a pumping speed of 100 L/s. The flow into the system is 10^{-6} mbar·L/s.
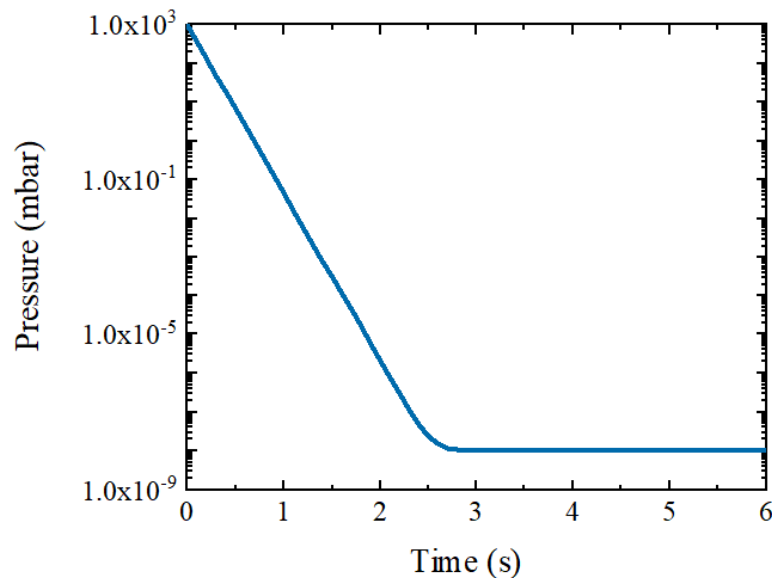
Figure 2.3 Pump-down curve for a 10-L system with pumping speed 100 L/s, and a flow into the system of 10^{-6} mbar·L/s.

In the above assumption, the chamber is pumped using a vacuum pump beginning from an atmospheric pressure of 10^3 mbar and rapidly decreasing to 10^{-8} mbar within 3 s. The result illustrates that the vacuum pump can efficiently pump the system to a high vacuum in a relatively short time, and the gas temperature, flow, and pumping speed are kept constant during the pump-down process as well as a small amount of flow into the system (e.g. outgassing, more on this in Section 2.3.3.1).

2.3.3 Sources of gases in a vacuum system

When pumping down a system to high vacuum conditions, one of the most crucial considerations is the gas load of the system [76]. Several gas sources exist in a high vacuum system, such as outgassing, leakage, initial gas, and process gas (Figure 2.4) [77]. Vacuum system walls and components in the system can release gas that is frozen, trapped, or adsorbed in the materials. Air infiltrates the vacuum system because of defects in the connection, or it permeates through the seals. Additional gas can sometimes be introduced when the required pressure must be attained. All these contributions have a significant effect on the pump-down time, pumping speed, and

ultimate pressure that the system can attain [41]. To create an accurate conceptual design, these contributions of gas sources in a high vacuum system must be known and estimated.
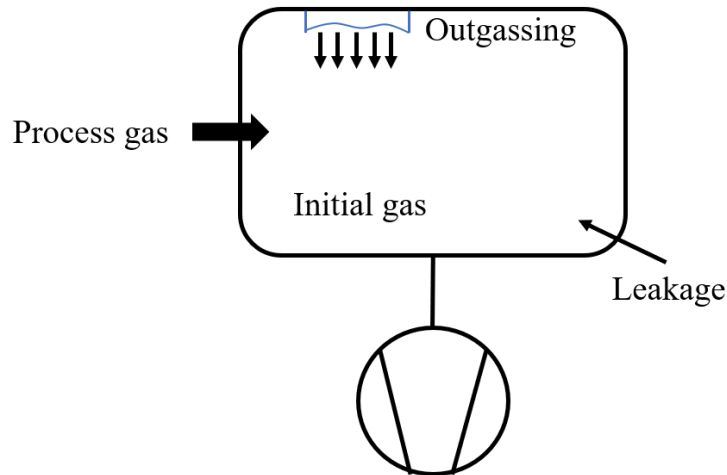
Figure 2.4 Contributions of gas loads in a vacuum system. Outgassing is the volume of trapped gas leaving the vacuum surface. Leakage results from an unintended path for gases. Initial gases are the original gases in the vacuum system. Process gas is a source introduced into the vacuum system on purpose.

2.3.3.1 Outgassing

Outgassing is considered to be the most important contribution to the gas load at approximately 90% of the total for a vacuum system, which is the volume of gas leaving a certain region of the surface per the unit time [78]. There are four main sources of outgassing: vaporisation, diffusion, desorption, and permeation [79, 80].

- Vaporisation: the release of molecules from surface material in the vacuum system;
- Diffusion: the release of gas molecules from the bulk material of the vacuum chamber;
- Desorption: the release of adsorbed gas molecules from the surface;
- Permeation: the release of molecules from the external side of the system

The outgassing rates depend not only on material properties, but also on material

surface preparation, circumstanced humidity and exposure durations to the atmosphere [66]. A major concern of the outgassing flow from materials in most applications is water vapour, along with N_2 and CO_2. Different species contributions to outgassing depend on the pressure range (Table 2.2).

Outgassing flow rate can often be approximated as follows:

$$Q = a_{1h} \cdot t^{-\alpha} \cdot A_{surface} \tag{2.16}$$

where $A_{surface}$ is the geometrical surface area, a_{1h} is the specific outgassing rate after 1 h of pumping, t is the time in units of hours, and α is the decay exponent. The values of α frequently range from approximately 0.2 to 1.2, depending on the material type.

Table 2.3 Category of decay exponent α [41]

Decay exponent α	Materials
0.2 – 0.7	Porous surfaces
0.4 – 0.8	Polymers
1	Metals, glasses and ceramics
1.1 – 1.2	Clean metal surfaces

The different outgassing mechanisms indicate the value of α. The value of diffusion-controlled outgassing from the bulk of the materials is approximately 0.5, and the desorption from surfaces (limited contribution from bulk) is approximately 1. The decay exponents of metals, glasses, and ceramics are approximately 1 (Table 2.3). However, the details of the surface preparation and cleaning process have a crucial effect on the metal outgassing rate, which can cause the decay exponent to be significantly lower than 1.

Compared with metals, polymer materials typically exhibit significantly higher outgassing rates and smaller decay exponents in the range of 0.4 to 0.8, which indicates diffusion-controlled outgassing. In addition to water vapour, polymer materials can

release volatile organic substances during the outgassing process. As a result, the outgassing rate of a polymeric wall is lower than 1 and primarily contributes to the total gas load. The pump-down time can be significantly longer.

In addition, the calculation of the gas load for a vacuum system has some practical limitations. Outgassing measurements are typically performed on a small sample of a simple-geometric-shaped plate, which is easy to manage and clean [81]. In practice, vacuum components frequently cannot be considered to be standard outgassing samples. Hence, the outgassing rate of the same material will increase and cause a smaller decay exponent. The National Aeronautics and Space Administration (NASA) has measured and recorded the outgassing rates of more than 10,000 materials [82]. Engineers should select proper vacuum materials for chambers, flanges, O-rings, and adhesives to attain the desired pressure in a short time.

2.3.3.2 Leakage

A leak is defined as unintended or undesired paths for gases and vapours to escape from one side of the vacuum wall to the other because of pressure differences. As the geometry of the channels is unclear and varies, the leak rate is difficult to predict. Therefore, the assumptions and calculations are performed only for ideal geometries.

In vacuum technology, leaks are considered to be sufficiently small if the leak rate is less than 10% of the total flow rate, and the remaining 90% of the flow rate is contributed by outgassing and process gas [41].   Hence, the tolerable leak rate is

$$Q_{leak,tot} \leq 0.1 \cdot Q_{total} = 0.1 \cdot p_{ult} \cdot S \qquad (2.17)$$

where Q_{total} is the total flow rate, and p_{ult} is the ultimate pressure, which is the lowest pressure that the system can reach. The general leak detection methods are foam-spray checking and bubble immersion tests, which are not sufficiently precise when the system is under high vacuum. In a high vacuum system, a helium leak detector is an ideal solution for leak tests [83]. A helium leak detector uses helium as the testing gas,

as it is a small molecule and suitable for detecting microleaks. The helium leak detector uses a residual gas analyser (RGA) to ionise the helium molecules, enabling ions to hit the ion collector. The detection range of the helium leak detector is frequently from 10^{-1} to 10^{-12} mbar·L/s.

2.3.3.3 Initial gas and process gas

Initial gas and process gas are often present in a vacuum system, which significantly affect the pressure of the system and pumping time. All vacuum chambers are initially at atmospheric pressure, where initial gas is the dominant contribution to the gas load in the early stage of a vacuum system [78]. The amount of initial gas depends on the volume and temperature of the system and will gradually or rapidly decrease when the pump starts. Sometimes, additional gas can be introduced when the required pressure has been attained, particularly in industrial vacuum systems (Table 2.4), which is called process gas. Process gas is frequently the dominant contributor to the gas load when it is present in a vacuum system

Table 2.4 Process gas loads in industrial vacuum systems [41]

Industrial Process	Process Gas Load (mbar·L/s)
Precision casting	0.1 – 10
Semiconductor processing	1 – 10
Large-area sputter coating of architectural glass	5 – 20
Induction melting	10 – 1000

Elementary idealised assumptions of the basic design equations have been provided in the previous sections, and they can provide useful practical solutions for system design. In practice, a pressure-independent pumping speed is very rare and hardly attainable for the entire vacuum process [41]. Therefore, the previous solutions can only yield crude approximations for an actual vacuum system. To predict the vacuum performance more accurately, the analytical calculations of pumping speed and pump-down time

should be solved based on an actual pumping process, sources of gas, and system conductance.

2.4 Flow of gases through tubes and orifices

As explained in Section 1.2, Knudsen number can reflect different types of vacuum: rough vacuum, medium vacuum, and high/ultra-high vacuum, which is also used to categorize the flow regimes in vacuum (Figure 2.5). Gas flow patterns determined by the value of Knudsen number play a crucial role in vacuum systems that usually involve complex piping arrangements, including aperture, circular long and short tubes etc. Therefore, it is essential to understand the gas flow through these piping arrangements. The conductance of the various geometric shapes differs in continuum flow and free molecular flow, as will be shown in the following sections.

(A) (B) (C)
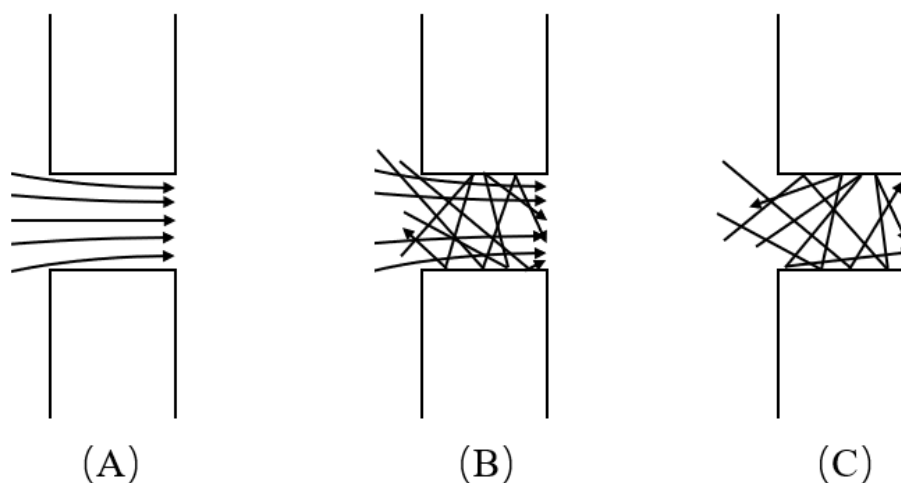
Figure 2.5 Diagram of gas diffusion (A) Continuum flow, $Kn<0.01$, Low vacuum; (B) Transitional flow, $0.01< Kn<10$, Medium vacuum; (C) Free molecular flow, $Kn>10$, High/Ultra-high vacuum [84].

2.4.1 Continuum flow

For continuum flow, gas behaviour is determined by internal friction and collisions between gas molecules [85]. It can be distinguished into viscous laminar flow and turbulent flow based on the Reynolds number. At low gas velocities, the gas flow is

laminar, for which the laminar flow velocity is often assumed zero at the walls of the system (no slip) and increases to the maximum velocity at the system axis. At high velocities, the gas flow swirls and is no longer layered. In most scenarios of vacuum technology, systems are in molecular conditions, for which viscous laminar conditions are rare. However, it aids in the understanding of the conductance for any other flow.

The Hagen–Poiseuille equation is used to derive the conductance of a circular cross-section tube in viscous laminar flow. The throughput is

$$Q = \frac{\pi d^4}{128 \eta L} \bar{p}(p_{entr} - p_{exit}) \tag{2.18}$$

Based on Equation 2.18, the conductance is

$$C_v = \frac{\pi d^4}{128 \eta L} \bar{p} \tag{2.19}$$

where d is the diameter of the tube, p_{entr} is the entrance pressure, p_{exit} is the exit pressure, η is the viscosity of the fluid, and $\bar{p}$ is the average pressure between the entrance and exit. In continuum flow, conductance is proportional to the pressure.

2.4.2 Free Molecular flow

As explained in the beginning of this chapter, the free molecular flow in vacuum technology can indicate Knudsen diffusion in porous media, where the gas movements are dominated by the collisions between the gas molecules and vacuum the walls. When the gas molecules collide with the walls, molecules adsorb for a short time. Subsequently, these molecules leave the surface according to Lambert's cosine law, and the leaving direction is not related to the incidence direction [86]. Similar to light scattering, these scattered molecules have an equivalent probability of emerging from any direction. The conductance of various components is crucial for vacuum system design and will be discussed in the following subsections.

2.4.2.1 Conductance of an aperture

The conductance of an aperture for the free molecular flow can be derived from the definition of conductance.

$$Q = A_{aperture} \sqrt{\frac{RT}{2\pi M}} (P_1 - P_2) \tag{2.20}$$

Hence, the conductance is given in Equation 2.21:

$$C_{aperture} = A_{aperture} \sqrt{\frac{RT}{2\pi M}} \tag{2.21}$$

where $A_{aperture}$ is the circular cross-section area, R is the gas constant, T is the absolute temperature, and M is the molar mass. For air at 20 °C, the conductance of an aperture is

$$C_{aperture} = 115.71 \cdot A_{aperture} \tag{2.22}$$

2.4.2.2 Conductance of a long tube with a uniform cross-section

The conductance of a long tube with diameter d was first derived by Knudsen [6]:

$$C_{long} = \frac{d^3}{3l} \sqrt{\frac{\pi RT}{2M}} \tag{2.23}$$

where l is the length of a cylindrical tube. According to Equation 2.21, the conductance of a long cylindrical tube (Equation 2.23) can be expressed as the conductance of the aperture multiplied by the transmission probability.

$$C_{long} = f_{long} \cdot C_{aperture} \tag{2.24}$$

Therefore, the transmission probability of a long cylindrical tube can be obtained as

$$f_{long} = \frac{4d}{3l} \tag{2.25}$$

In 1965, Berman derived a correction of Equation 2.25 for a long tube [87], as shown in Equation 2.26 (with first five terms):

$$f_{long} = \frac{4d}{3l} - \frac{1}{2}(\frac{d}{l})^2 \ln(\frac{2l}{d}) - \frac{91}{72}(\frac{d}{l})^2 + \frac{4}{3}(\frac{d}{l})^3 \ln(\frac{2l}{d}) + \frac{1}{3}(\frac{d}{l})^3 \qquad (2.26)$$

2.4.2.3 Conductance of a short tube with a uniform cross-section

The expressions for the conductance of a short tube can also be formulated in terms of transmission probability, which is the conductance of the entrance aperture multiplied by the transmission probability.

$$C_{short} = C_{aperture} f_{short} \qquad (2.27)$$

The transmission probability for short tubes calculated by Cole in 1977 is shown in Figure 2.6 [40].
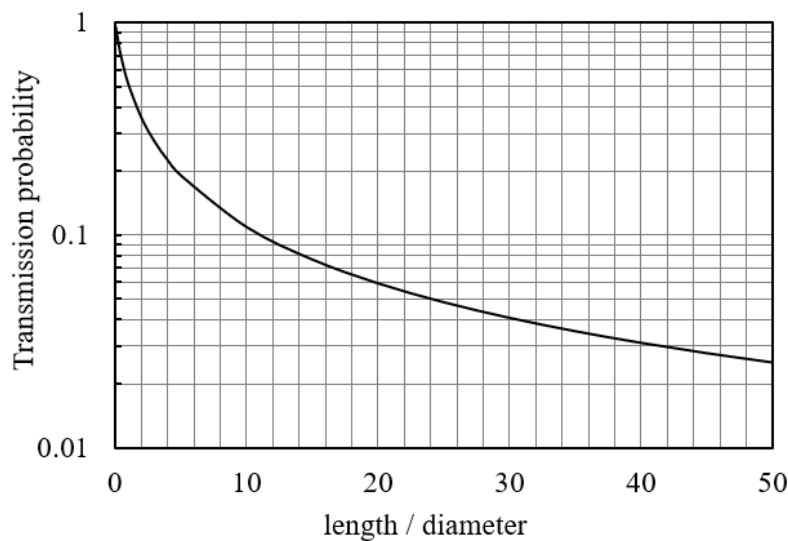
Figure 2.6 Transmission probabilities for short tubes

Berman derived the transmission probability equation of short tube in 1965 [87]. The results calculated using Equation 2.28 have demonstrated remarkable agreement with Cole's calculation with less than 0.2% deviation (Appendix Table A.1). In addition, the transmission probabilities for rectangular ducts are also shown in Appendix Table A.2 [88].

$$f_{short} = 1 - \frac{1}{2}(\frac{d}{l}) + (\frac{d}{l})^2 - \frac{5}{6}(\frac{d}{l})^3 + \frac{1}{2}(\frac{d}{l})^4 - \frac{13}{80}(\frac{d}{l})^5 - \frac{1}{60}(\frac{d}{l})^6 \qquad (2.28)$$

2.5 High-vacuum pump set

To achieve a high vacuum in a relatively short time, vacuum pumps should be studied properly. An integrated high-vacuum pump set is generally used to implement a high vacuum. A high-vacuum pump set frequently consists of a fore-vacuum pump unit that pumps from the atmospheric to the 'transition' pressure of 10^{-2} mbar and high-vacuum pump units that operate normally below 10^{-2} mbar [41].

2.5.1 Fore-vacuum pumps

In a high vacuum system, the high-vacuum pump sets commonly require fore-vacuum pumps, which serve as the backing pump or roughing pump [89]. A backing/roughing pump is required to perform two operations. First, it should evacuate chambers from atmospheric pressure to a certain low pressure, enabling the high-vacuum pump to begin operating. Subsequently, it will revert to the function that provides a low pressure (foreline pressure) at the outlet or exhaust of the high vacuum pump [71]. Using a wrong roughing/backing pump can easily destroy all other careful work. Hence, a proper roughing/backing pump must achieve specific demands in the ultimate vacuum and can provide continuous service over several months without interruption [90]. Three types of pumps are primarily used as the fore-vacuum pumps: rotary vane, diaphragm, and scroll pumps.

2.5.1.1 Diaphragm pump

A diaphragm pump is an oil-free positive-displacement pump, which is also known as a membrane pump. The most commonly used diaphragm pump is a liquid-operated diaphragm pump, which can manage varying liquids with different viscosities as well as many chemicals including acids [91]. An air-operated diaphragm pump is another type of diaphragm pump that uses compressed air as the power supply [66].

A diaphragm pump operates without any oil and no particles are generated. Therefore, these pumps are most frequently used in dry and clean vacuum systems, particularly for the two-stage diaphragm with even longer durability. Another advantage of diaphragm pumps is that they perform reliably with little noise and vibration.
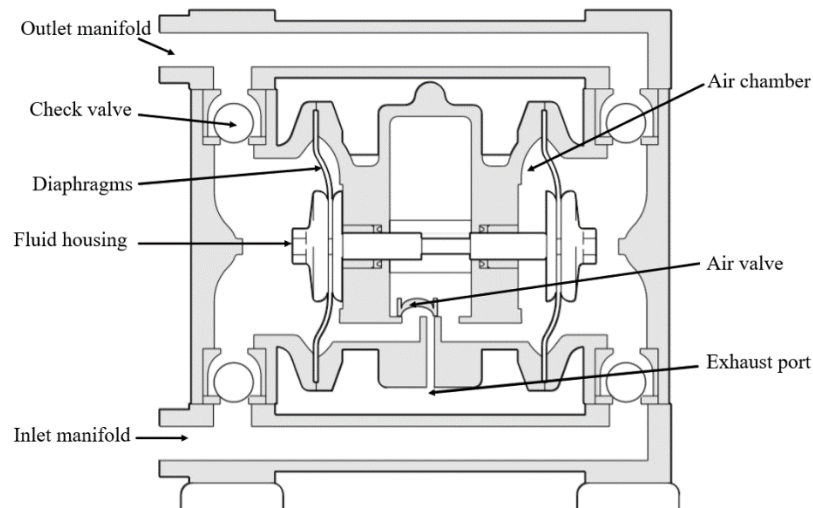
Figure 2.7 Schematic diagram of a diaphragm pump [92]

2.5.1.2 Rotary vane pump

A rotary vane pump is an oil-sealed positive-displacement pump consisting of an eccentrical rotor, housing, vanes, working chamber, and the inlet valve [93]. When the rotor begins spinning, the vanes slide in and out to keep contacting with the housing. As the vanes rotate, a working chamber forms and is sealed by the valve to split the chamber into two variable volume compartments. The gas enters the expanding suction chamber before the second vane seals it off. Subsequently, the enclosed gas is compressed until the outlet valve is opened against ambient pressure. When the oil-sealed outlet valve is open, a small amount of oil enters the suction chamber to seal the vanes against the housing [94].

Rotary vane pumps are frequently used as backing pumps in high vacuum systems. However, the pumped gas and oil are mixed within the pump. A significant concern for these pumps used in high vacuum systems is the contamination of the entire vacuum

system by oil back-streaming.
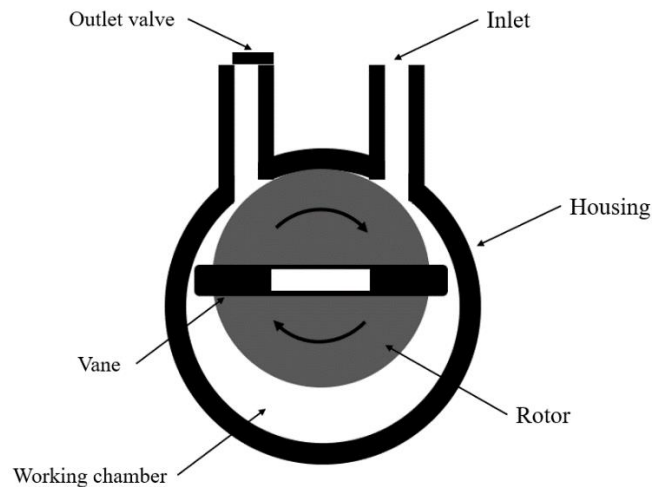
Figure 2.8 Schematic diagram of a rotary vane pump. Adapted from [95].

2.5.1.3 Scroll pump

The scroll pump is an oil-free, high-performance vacuum pump frequently employed in crude and medium vacuum systems. This type of pump is also frequently used as a backing pump in high or ultra-high vacuum systems. Scroll pumps are also considered to be excellent options compared to rotary vane pumps owing to their oil-free features. Moreover, they have longer bearing lives and can provide clean and dry vacuums [41].

A scroll pump consists of two spiral-shaped scrolls in the housing, with an outlet at the centre of the scroll assembly [96]. One scroll is fixed, and the other spiral is an orbiting scroll that moves eccentrically. Gas enters the open end of the scrolls, is trapped between the scrolls, squeezed, and transported towards the centre. As the gas moves towards the centre, the volume decreases, and the gas is compressed.
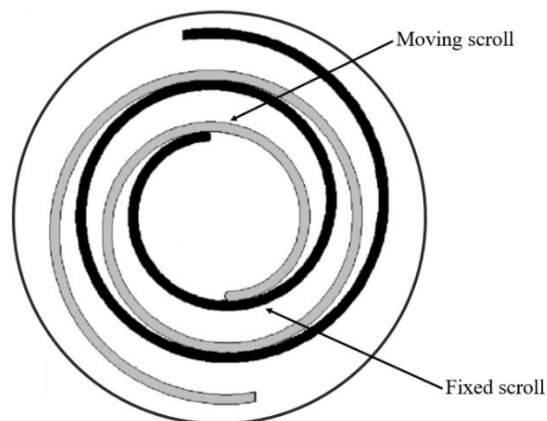
Figure 2.9 Schematic diagram of a scroll pump. Adapted from [97].

Table 2.5 Comparison of different fore-vacuum pumps

Pumps	Size	Oil-free	Approx. Ultimate Pressure
Rotary vane pump	Medium	No	10^{-1} mbar – 10^{-3} mbar
Diaphragm pump	Small	Yes	Atmospheric to 10^{-1} mbar
Scroll pump	Large	Yes	Atmospheric to 10^{-2} mbar

The first crucial step in designing a high-vacuum pump set is selecting the most suitable backing pump (Table 2.5). Engineers should consider the pump dimensions, ultimate pressure, pumping speed, working conditions, and application of the vacuum system simultaneously.

2.5.2 High-vacuum pumps

The process of selecting the most suitable high-vacuum pump set is time-consuming and difficult, and it should consider both fore-vacuum and high-vacuum pumps systematically. The most used high-vacuum pump sets are equipped with diffusion, turbomolecular, and turbomolecular pumps in combination with molecular drag pumps [98]. Regardless of the pumps applied in the high vacuum system, the pumping speed of these pumps can be depicted by three ranges: the ultimate pressure, operating, and overload ranges. To successfully design a high-vacuum pump set, all ranges should be understood. At the ultimate pressure range, pumping is limited by the maximum

compression of the high-vacuum pumps, which is related to the planned ultimate system pressure. In the operating range, the pumping speed is constant. At high pressures, overload occurs and is hardly avoidable. To minimise the overload time, the effective pumping speed of the high-vacuum pump should be no smaller than that of the fore-vacuum pumps, and the fore-vacuum pump should be able to maintain the pressure below the foreline pressure [99].

2.5.2.1 Diffusion pump

The diffusion pump is a high-vacuum pump using a high-speed vapour jet to capture air molecules. The fluid moves the air molecules toward the bottom of the pump and exits the exhaust. It is considered to be the first type of high-vacuum pump operating in the free molecular flow regime [100]. The diffusion pump is also the primary industrial high-vacuum pump, because of its high performance (low ultimate pressure, high pumping speed, etc.) and low initial cost, and it uses polyphenyl ethers or silicone oil as the working fluid [101].
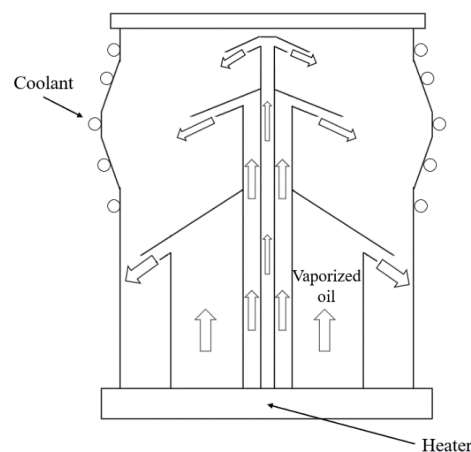
Figure 2.10 Schematic diagram of a diffusion pump. Adapted from [102]. A diffusion pump consists of three cone-shaped pressure nozzles. The oil is heated to the gaseous state by a heater. The vaporized oil travels upwards, then accelerates to sonic speed through nozzles. As the vapour travels toward the walls of the vacuum body, it traps gas molecules along the way through diffusion, then transports them from the inlet to the exhaust.

2.5.2.2 Turbomolecular pump

A turbomolecular pump is classified along with a kinetic vacuum pump as a momentum transfer pump, which transmits kinetic energy to gas molecules [103]. The turbopump has a high-speed rotating circular disk with several angled blades, which frequently consists of a stationary stator blade and quickly rotating rotor blade pair [104]. Gas molecules enter the pump housing through the inlet. As the disk rotates at high speeds, these angled blades hit the gas molecules [105]. Accordingly, the blades transfer the mechanical energy into momentum, causing molecules to move towards the outlet [99].
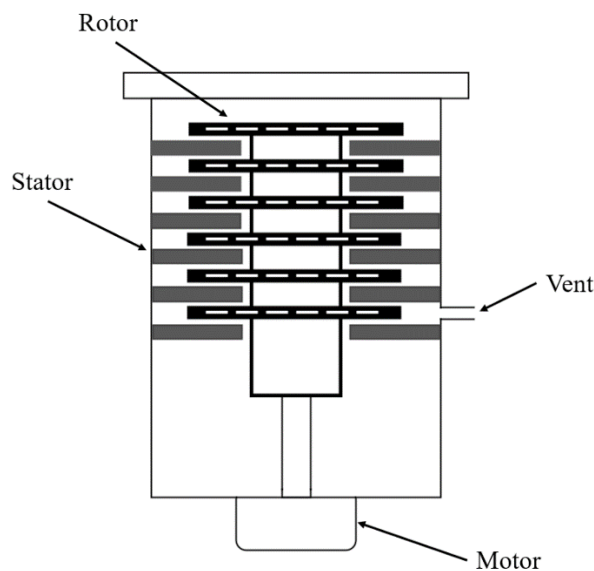
Figure 2.11 Schematic diagram of a turbomolecular pump. Adapted from [106]. The turbomolecular pump consists of few rotors and stators, which rapidly spin and hit gas molecules from the pump inlet towards to the vent to generate a vacuum.

A comparison of the diffusion and turbomolecular pumps is shown in Table 2.6. The diffusion pump offers the advantage of being low-cost, easy to maintain, and having a perfect operating ability for dirty processes. The disadvantages of diffusion pumps are oil contamination problems, slow start and stop, and difficulty in applying to ultra-high vacuum. For turbomolecular pumps, the inherent advantages are that they are considerably clean without any oil contamination, quick to start and stop, and designed for ultra-high vacuum. However, the high cost and maintenance service limit their

application in many fields.

Table 2.6 Comparison of different high-vacuum pumps

Pumps	Advantages	Disadvantages
Diffusion pump	- Cheap (start ~ £500) - Easy to maintain - Work great for dirty processes	- Slow to start & stop - Oil contamination issues - Hard to use for ultrahigh vacuum (UHV)
Turbomolecular pump	- Quick to start & stop - Clean – no oil contamination - Reaches ultra-high vacuum (UHV)	- Expensive (start ~ £3000) - Costly maintenance service

CHAPTER

THREE

3 Conceptual and practical design

While diffusion at atmospheric pressures in disordered porous media interests us, the diffusion in a vacuum through macroscopic tubes directly relates to the Knudsen diffusion in porous media, as long as the mean free path is larger than the tube diameter. Therefore, vacuum technology should be properly studied to successfully construct a vacuum apparatus and perform diffusion experiments in the Knudsen regime. Designing a vacuum system requires knowledge of different disciplines such as vacuum technology, mechanical engineering, physics, and electrical engineering. In this chapter, a conceptual design of the vacuum diffusion system for Knudsen diffusion measurements is presented, including the preliminary design of a vacuum chamber and high-vacuum pump set. Based on the conceptual design, a more detailed practical design of the main vacuum components from the aspects of the material, crucial parts selection, and economic considerations are discussed.

3.1 Conceptual design

The application of this specially designed high vacuum system is to measure Knudsen diffusion and gain more insight into both transport and self-diffusion in a single pore of catalysts. Therefore, the high vacuum system must be capable of maintaining a low pressure, managing the process gas injected into the system continuously, and smoothly

and precisely measuring the system pressure for Knudsen diffusivity calculations. The Knudsen regime requires the pump sets to create pressures of at least 10^{-4} mbar.

As the heart of the high vacuum system, the high-vacuum pump set should consist of a fore-vacuum pump and a high-vacuum pump to promptly evacuate the system and maintain the high-vacuum range for a certain time. Two options for the pump unit design are available:

1) Both chambers are evacuated using a single, high-capacity pump set.

Using a single pump set can cause some of the gas molecules to travel from one chamber to another *via* the pump lines, making the system less accurate, and the total capacity of a single pump set should be extremely large.

2) Each chamber has its own pump set.

This option enables easier manipulation of the pressure in each chamber and provides more accurate measurements.

Because of its advantages, the second option was selected as the pump unit design. According to these requirements, a schematic diagram of the conceptual design for the high vacuum system for Knudsen experiments is presented in Figure 3.1. Two vacuum chambers are connected using a straight cylindrical tube, in which the diffusion process occurs. In the meantime, two individual high-vacuum pump sets are attached to the vacuum chambers to maintain the system pressure in the high-vacuum range and investigate Knudsen diffusion under different conditions in the diffusion channel.
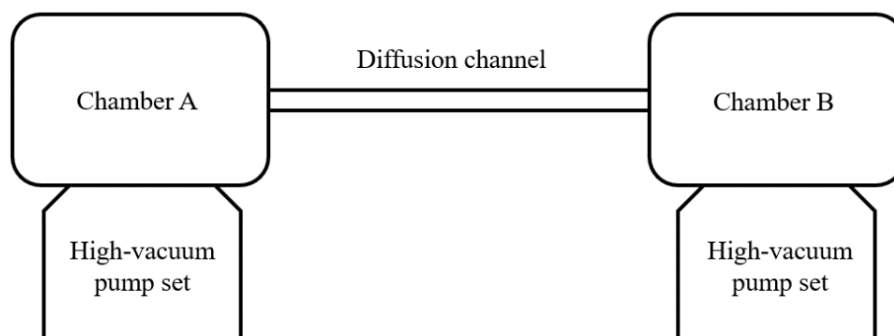
Figure 3.1 Conceptual design of the high-vacuum system.

From the perspective of vacuum technology, the designed system should have small surface areas with low outgassing rates, high conductances, and large pumping speeds. Based on the conceptual design, the practical design of all related vacuum components is further discussed in the following sections from aspects of technical principles, feasibility, lifetime, accuracy, and economic considerations.

3.2 Vacuum chamber design

As the heart of a high vacuum system, a vacuum chamber should be tailored to attain the Knudsen regime within a relatively short time. As the maximum working pressure (10^{-4} mbar) is calculated in the previous section, the chamber to be selected should be an ultra-high vacuum (UHV) chamber. In this section, a preliminary design is discussed first, followed by more technical design requirements, including the selection of materials, flanges, vacuum seals, and grooves.

3.2.1 Preliminary design

The crucial design factor for UHV chambers is the mechanical bearing capacity, which is the pressure difference between the inside and outside of the vacuum chamber. For a UHV chamber, the pressure acting on the outside of the chamber is approximately 1000 mbar (atmospheric pressure). Hence, the chamber should be designed such that it can sustain this pressure difference without being deformed. In addition, the connections between the chambers and other vacuum components should be sufficiently robust and vacuum-tight.

Generally, two types of vacuum chambers are used in a high vacuum system: cylindrical and rectangular chambers [107]. When atmospheric pressure is applied to a wall 3 mm thick (commercial standard) for both cylindrical and rectangular chambers, the latter can be plastically deformed at the sharp edges. As a result, the rectangular chamber requires a thicker wall than a cylindrical chamber. To decrease the cost of the material as well as the chamber weight, a cylindrical chamber that can be modified from a standard tee was selected. As the vacuum chamber will be used in both the HV and

UHV ranges for a certain time, it should be capable of bearing 120 °C (maximum bake-out temperature of the flange of the high-vacuum pump) before being used for measurements and to sustain the atmospheric pressure without deformations [108]. Additionally, the vacuum chamber must be significantly larger than the diameter of the tube, and the chambers should not affect the vacuum or gas transport phenomena occurring in the tube in the subsequent Knudsen diffusion measurements.

Hence, the vacuum chamber for gas diffusion experiments has a standard commercial three-way cross as the main body, in which one port of the cross at the vertical axis is used as the pumping port and the other ports are the gas throughput ports. In addition, the chamber must have an access port to introduce experimental gas into a high vacuum system and a pressure gauge port to accurately measure the chamber pressure (Figure 3.2).
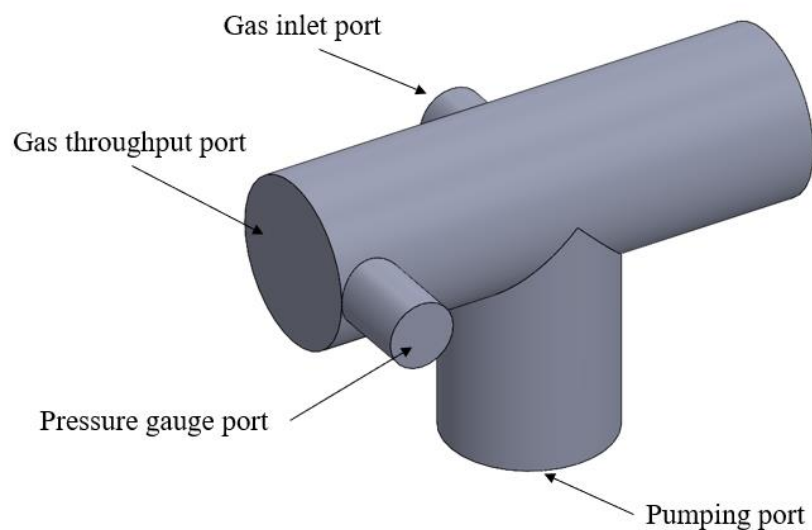
Figure 3.2 Conceptual design of a vacuum chamber

3.2.2 Material selection

For the chamber to rapidly attain the UHV range, a crucial decision about the chamber material should be made to accelerate the pump-down process. As mentioned in Section 2.3.3, the basic gas load of a vacuum system guides the chamber material selection. The first pump-down stage involves evacuating the initial gas from the chamber. The second

stage involves gas from the materials, and the ultimate pressure is highly dependent on the materials. Making an appropriate selection of chamber materials means both selecting the materials with the lowest gas loads and considering their chemical and physical properties.

The most commonly used materials for chamber construction are metals, ceramics, glasses, and plastics [71]. The following considerations directly influence the selection of the vacuum materials: chamber internal surface desorption, chamber wall outgassing, vapour pressure of materials, and mechanical properties [66, 109, 110].

Internal surface desorption: The internal surface is frequently covered with layers of adsorbed water molecules that must be desorbed during the pump-down process. Therefore, the materials should not strongly bond to the water molecules; hence, plastic materials are not suitable for high-vacuum chambers [81]. Additionally, the roughness of the internal surface does not significantly affect the pumping procedure for a pressure higher than 10^{-6} mbar, and only has very limited impact for the pumping time in the lower pressure range [111].

Chamber wall outgassing: The most crucial sources of gases in a UHV are determined by the outgassing of chamber materials, as well as the initial gases pumped out from the chamber [70]. The outgassing rates of commonly used vacuum materials are shown in Appendix Table A.3. Metal materials have lower outgassing rates compared with polymers, particularly for baked stainless steel and aluminium [112].

Vapour pressure of materials: When performing heating for vacuum components, understanding the possibility of evaporation is essential. Gas loads can be increased by the vaporisation of the materials in the chamber and affect the vacuum surroundings. Metals evaporate as a function of temperature and vapour pressure. Low vapour pressure is a critical consideration when selecting chamber materials [110]. High vapour pressure metals such as cadmium and zinc cannot be used as they can cause metallic contamination during the heating process and form oxide coatings that adsorb large quantities of water vapour [113].

Mechanical properties: Mechanical properties are always an important consideration when selecting a material. The first requirement of the mechanical properties is bearing atmospheric pressure without deformation at room temperature, hence, the tensile strength, yield strength, and Young's modulus should be considered. In addition, the chamber should maintain structural integrity at the baking temperature (120 °C). In addition, the surface finishing is crucial for material selection, for which the surface cleaning must ensure that no organic contamination or metallic oxide is on the surface and no porous welding scales remain [110].

Considering all the technical requirements explained above, stainless steel (SS) has been selected as the construction material for the vacuum chamber. Aluminium alloys can also be used for the entire vacuum regime with a low outgassing rate after baking out, and the weight is lighter than that of stainless steel. However, the aluminium chamber should be carefully checked before being used to ensure that the inner surface has not been anodised. Therefore, the SS chamber can be opened more frequently than the aluminium chamber. However, not all SS alloys can be used for high vacuum applications [114]. For example, 303 SS containing sulfur is not suitable for a high vacuum system because of the high vapour pressure of sulfur [115]. 304 SS is frequently used in vacuum systems; it contains 18% Cr and 8% Ni on an Fe basis [110]. In practice, both 304 SS and its low carbon version 304L SS (0.03% carbon) are widely used in industries [116], which the only difference is the latter enhances the corrosion resistance and ductility. Therefore, 304L SS is more suitable for the UHV chamber; it was selected as the material of the vacuum chamber.

3.2.3 Flange selection

Vacuum flanges are the flanges at the end of the vacuum components used to connect different units; they should be selected carefully based on the materials and functionality aspects to avoid unnecessary leaking [117].

For material requirements, vacuum flanges must be compatible with UHV. As discussed in Section 3.2.2, the materials of vacuum flanges must have a low vapour pressure and

low outgassing rate. In addition, the flanges must satisfy the requirement of sustaining the baking temperature without deformation. Based on their the functionality, Klein Flansche (KF) and ConFlat (CF) flanges are primarily used as connections between the different vacuum components (Figure 3.3). The KF flange is a quick-release flange using rubber O-rings; it is easy to disassemble compared with the CF flange. The CF flange is frequently used in the vacuum system, particularly for UHV. The CF flange uses copper gaskets and bolts and nuts. The applicable vacuum range can be down to 10^{-12} mbar [118].

(A)   (B)
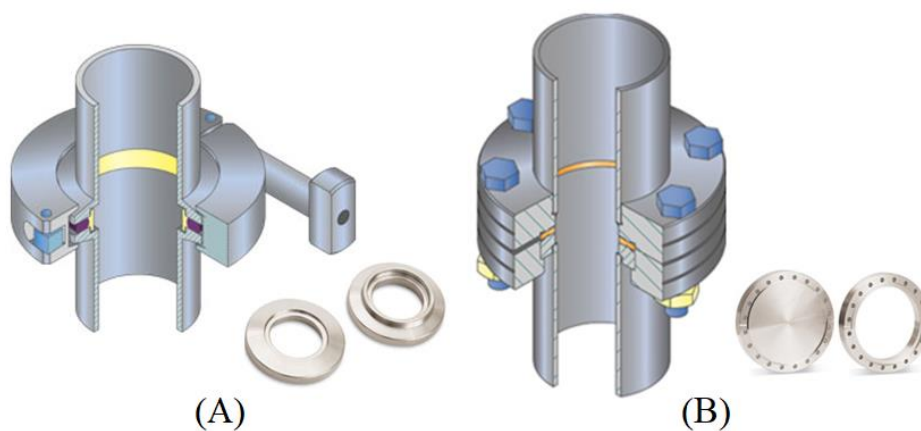
Figure 3.3 A) KF flange B) CF flange. Edited from [118]

Table 3.1 Technical data of KF and CF flanges as vacuum connections

Types	Material	Pressure range (mbar)	Temperature range (°C)
KF flange	304L SS	$10^3 – 10^{-8}$	0 °C – 180 °C
CF flange	304L SS	$10^3 – 10^{-12}$	-196 °C – 450 °C

A 304L SS CF flange was selected, because of its superior mechanical, thermal, and sealing properties in UHV (Table 3.1). For the pressure gauge and high-vacuum pump ports, DN40 and DN100 non-rotatable CF flanges were selected considering the vacuum chamber design, cost, and product availability on the market.

3.2.4 Vacuum seals and groove selection

After selecting the appropriate type of flange, vacuum seals and grooves should be selected; these are used to prevent ambient air leaking or permeating into the vacuum system [119]. The circular gasket seal is the most used. O-rings are frequently fabricated from elastomer, and the metal seals are available in many different materials, such as copper, stainless steel, and aluminium. The vital properties of a vacuum seal are the gas permeation resistance, mechanical properties, and temperature resistance. In Table 3.2, a few widely used vacuum seals are compared.

Table 3.2 Comparison of typical detachable vacuum seals [117]

Material	Maximum working temperature	Notes
Synthetic rubber	90°C	- Multiple usage - Low price - Approx. outgassing rate 10^{-6} mbar
Fluoroelastomer (VITON®)	150°C	- Multiple usage - Expensive - Approx. outgassing rate 10^{-8} mbar
Aluminium	260°C	- One-time usage - Suitable for small flange - Aluminium CF flange specify
Copper	400°C	- One-time usage - Very low permeability - Relative low price - Application for UHV

As elastomer seals would not be sufficient for an ultra-high vacuum diffusion system; therefore, a metal seal was selected. By comparison, the vacuum performance of copper gaskets is high with almost no permeation of gases, low outgassing, long-term radioactive resistance, and sustained high bake-out temperature. Although copper gaskets are not multiple-usage seals, the commercial unit price for the most used gasket, DN100CF, is acceptable at £2 [120].

Copper gaskets are accommodated in grooves, which should be machined in the flanges welded to the vacuum chamber. The vacuum face seal gland was selected for the SS flanges, and the design diagram is shown in Figure 3.4.
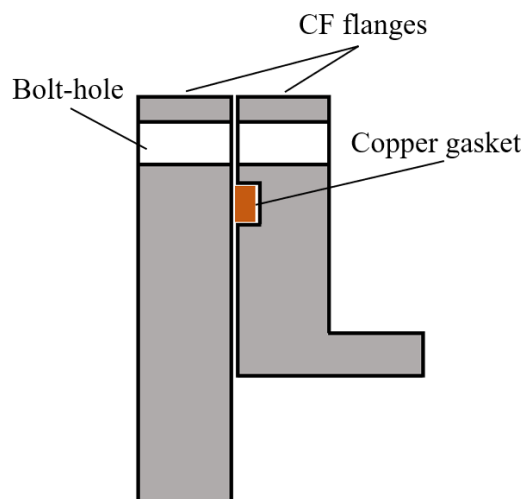
Figure 3.4 Diagram of a copper gasket seal in vacuum flanges

The outgassing rate of the vacuum chamber significantly affects the ultimate pressure of the system [121]. The aim of the high-vacuum chamber is to maintain the pressure as low as possible (maximum 10^{-4} mbar) to ensure the system remains in the Knudsen regime. Therefore, the main body of the vacuum chamber and related components, including the CF flanges, bolts, and nuts, should be fabricated from 304L SS with a 10^{-12} mbar·L·s^{-1}·cm^{-2} outgassing rate after proper surface cleaning, polishing, and baking at 120 °C. To avoid interfering with the diffusion process in the channel, the dimensions of the chamber should be sufficiently large. Considering the economic feasibility, the DN100 commercial standard tee was selected as the main body of the chamber. A more detailed design of the vacuum chamber will be discussed using a numerical approach in Chapter 4.

3.3 High-vacuum pump set design

A high-vacuum pump set should consist of fore-vacuum and high-vacuum pumps to achieve UHV conditions. To remove the initial gas in the vacuum system and attain the

'transition pressure' of 10^{-2} mbar, a fore-vacuum pump is required. To attain the ultra-high vacuum range, a high-vacuum pump must be applied to the system. With a previous understanding and estimation of the pump-down time and sources of gas in high vacuum, a combination of different pump types will be designed in this section. The ultimate pressure of the system equipped with the high-vacuum pump set should be able to attain 10^{-8} mbar or even lower.

3.3.1 Preliminary design

The first step in designing a high-vacuum pump set is to satisfy the basic requirements of the application of the vacuum system, which precisely measures gas diffusion in the Knudsen regime. Consequently, oil-free or oil-sealed is the first and most critical consideration. Oil-sealed mechanical pumps (rotary vane pumps) are commonly used as backing applications for turbomolecular or diffusion pumps. Although they are less expensive than oil-free pumps and fairly reliable, they still have a risk of potential hydrocarbon contamination [72]. The back-streaming of oil from the pump into the vacuum chamber will severely affect the measurements of gas diffusivities. Hence, the design of a high-vacuum pump set should be prudent to exclude any oil-sealed fore-vacuum pumps, as well as the oil-contained high-vacuum pump. Additionally, turbomolecular pumps with no oil contamination should be selected as the high-vacuum pumps of the pump set.

The next step will be the careful study of the pressure versus pumping speed, which is the actual performance of the pumps. The selected fore-vacuum pump must provide sufficient pumping speed and throughput to maintain the required foreline pressure to satisfy the performance requirements of the high-vacuum pump [85]. Otherwise, the high-vacuum pumps will stop pumping. The third step is to select a proper type of oil-free pump; a dozen oil-free pumps with different capacities are available on the market. The different types of oil-free pumps are explained from various considerations (performance, price, maintenance, reliability, etc.) in the next section.

According to these design steps, a high-vacuum pump set was conceptually designed

by combining of a turbomolecular pump and an oil-free fore-vacuum pump. The design of high-vacuum pump sets can be conducted using two approaches: with bypass and without bypass (Figure 3.5).
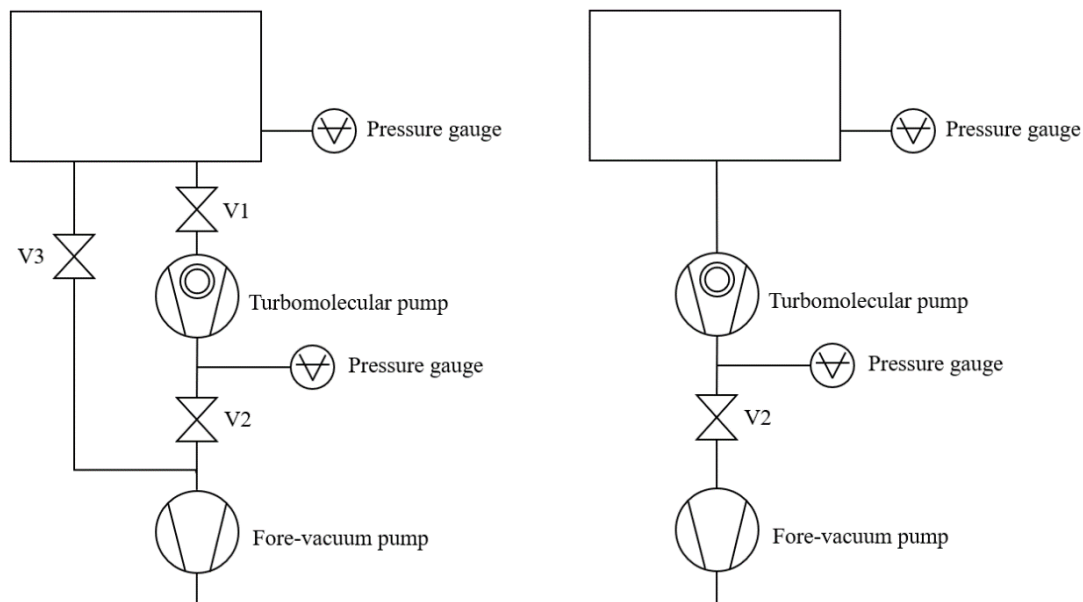
Figure 3.5 Schematic diagram of two set designs of high-vacuum pumps: A) with bypass; B) without bypass

With the first approach, the fore-vacuum pump can be connected to the vacuum system through a bypass pumping line and bypass valve (V3). The system is initially pumped down to the specified pressure before V3 is closed to terminate the roughing pumping down process. Subsequently, the high-vacuum valve (V1) is opened to the inlet of the turbomolecular pump and the fore-vacuum valve (V2) is opened simultaneously, and the inlet of the fore-vacuum pump is valved using V2 into a line on the exhaust of the turbomolecular pump. This design can avoid particle deposition in the turbomolecular pump (TMP) during the roughing process, and optimising the bypass pumping line (roughing process) is easy. However, this design significantly increases the complexity of valving, plumbing, and even the design of the vacuum chamber.

The second method involves directly using a turbomolecular pump as part of the roughing process. The vacuum system is pumped by starting the fore-vacuum pump with only opening the fore-vacuum valve (V2), which is evacuated through the

turbomolecular pump. After the maximum tolerable pressure of the turbomolecular pump is attained, the turbomolecular pump starts. This design is much more flexible and cheaper than the first one. However, it can result in a slightly longer pump-down time for a small system and particle deposition in the turbomolecular pump if polymers are introduced into the vacuum system without pre-treatment. With a systematic consideration of the pump's performance, system conductance, dimension of the applied vacuum system, plumbing and valving complexity, and financial and maintenance aspects, the second conceptual design was selected to create the high-vacuum pump set.

3.3.2 Fore-vacuum pumps

As mentioned earlier, the selected fore-vacuum pump must be an oil-free pump to avoid unpredicted particle contamination in the vacuum system. In addition, several other factors should be considered before purchasing the fore-vacuum pump, such as initial and repair costs, power usage, and high-vacuum backing requirements. Therefore, a dry scroll pump is the first option because of the advantages of being contamination-free, its low power consumption, and long service intervals.

As many types of dry scroll pumps are available on the market, we calculated the required average pumping speed to identify the pump type. In this high vacuum system, the volume of the chamber was approximately 3 L. To evacuate the initial gases of the chamber within a reasonable time (less than 1 min), the minimum pumping speed was calculated using Equation 2.15. The minimum average pumping speed was required to be not less than 0.58 L/s. An Edwards nXDS dry scroll pump providing robust, quiet operation, and clean pumping is desired [122]. Four sizes of nXDS are available: nXDS6i, nXDS10i, nXDS15i, and nXDS20i, along with increasing pumping speed. The pumping speed of the smallest size nXDS6i is 1.7 L/s, which is sufficient for the ultra-high vacuum chamber. Therefore, the Edwards nXDS6i was selected as the fore-vacuum pump (Table 3.3).

Table 3.3 Technical data of Edwards nXDS6i [122]

Description	Unit	Value
Peak pumping speed	L/s	1.7
Ultimate vacuum (total pressure)	mbar	0.020
Power consumption	W	260
Weight	kg	26.2
Inlet flange		NW25
Exhaust flange		NW25
Leak tightness	mbar·L/s	$<1 \times 10^{-6}$
Operating temperature	°C	+5 to +40

Figure 3.6 Edwards nXDS6i dry scroll pump [123]

3.3.3 High-vacuum pumps

To pump down the system from 10^{-2} mbar to UHV, an oil-free turbomolecular pump should be used as a high-vacuum pump, as discussed in Section 3.3.1. The time it requires for the vacuum system to attain the ultimate pressure depends on the amount of gas and water vapour adsorbed on the walls of the system and the pumping speed of the turbopump. Hence, a turbomolecular pump with a high pumping speed is necessary to attain the UHV reasonably quickly. The experientially recommended pumping speed is approximately 100 times the speed of the fore-vacuum pump [124]. As a result, the

pumping speed of the turbomolecular pump should be at least 170 L/s. Edwards provides five types of turbomolecular pumps: nEXT85, nEXT300, nEXT400, nEXT730, and nEXT930. However, selecting an economical and practical turbomolecular pump that satisfies our requirements is a time-consuming process, which needs to balance pump performance and cost. The details of pump selection will be discussed in the next chapter through analytical and numerical analysis.

A turbo and instrument controller (TIC) was selected as the controller of the high-vacuum pump set controller. It can automatically recognise the nXDS dry scroll pump when connected to the fore-vacuum pump connector, which is convenient for the installation process without using a relay box to interface with the nXDS. Additionally, the TIC can directly control the nEXT turbomolecular pump and three pressure gauges simultaneously. Many necessary functions, such as speed control, running hours, and active gauges, can be readily accessed from the display panel [125]. A schematic diagram of the high-vacuum pump set and the image of the designed high-vacuum pump set are shown in Figure 3.7 and Figure 3.8.
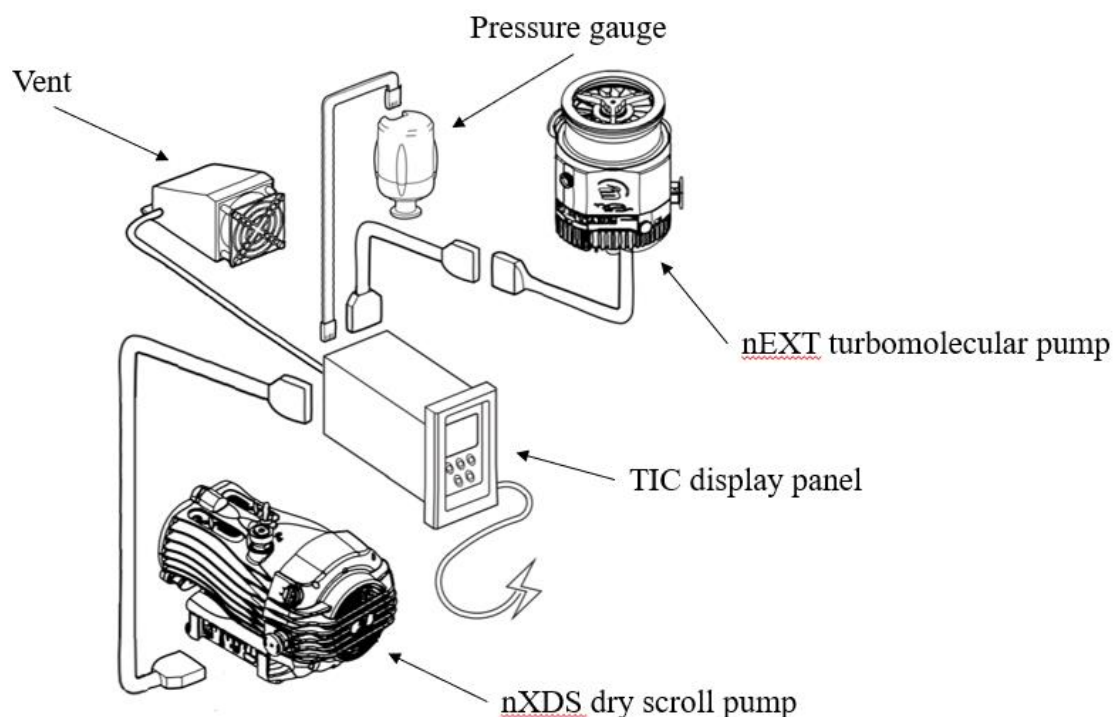
Figure 3.7 Schematic diagram of high vacuum pump set

Figure 3.8 Image of the designed high-vacuum pump set

3.4 Design of other vacuum components

3.4.1 Diffusion channel

The specially designed tube in the centre of the apparatus is considered to be the diffusion channel for gas transport from one side to the other. The interaction of diffusing molecules with the walls motivated us to study the molecular dynamics, in which the channel should remain in the Knudsen regime for the entire measurement. Ideally, the diameter of the SS tube should be as small as possible to ensure that the system remains in the Knudsen regime. In addition, the diameter of the SS tube should be slightly larger than the diameter of the 3D printing tubes for the surface roughness investigation. According to these requirements, the diameter of the SS tube should not be smaller than 2 cm. Otherwise, the 3D parts would be difficult to print and cannot be inserted into the SS tube. If the diameter of the tube is too large, the system may require larger capacity pumps, which can also significantly increase the 3D printing cost. The diffusion channel was designed to connect with vacuum chambers *via* DN100CF flanges to ensure good leak tightness (Figure 3.9).
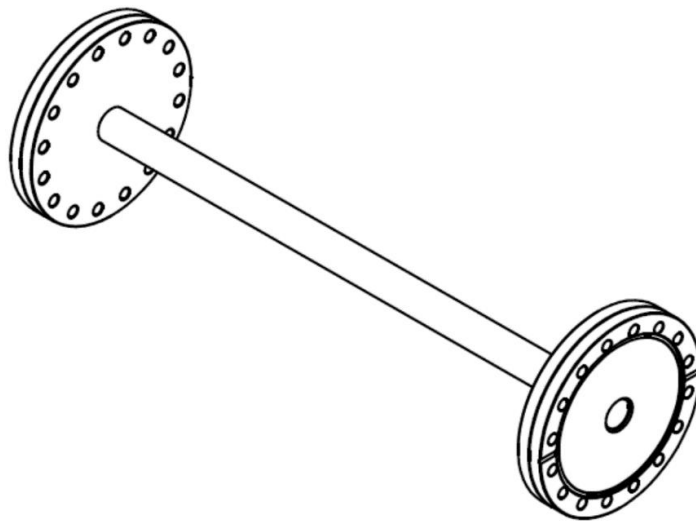
Figure 3.9 304L SS diffusion channel (DN100CF-DN100CF)

Kurt J. Lesker fabricated CF nipples for our high vacuum system using 304L SS tubing and knife-edge CF flanges. The diameter of this custom full nipple was 25.4 mm (1 inch). As Knudsen calculated the diffusion coefficient by examining a long tube with a circular cross-section [6], the diffusion channel of our system should also be sufficiently long. Considering the site-specific constraints, the length of the diffusion channel was limited to 500 mm, and the ratio between length and diameter was approximately 20. The lateral view of the diffusion channel is shown in Figure 3.10.
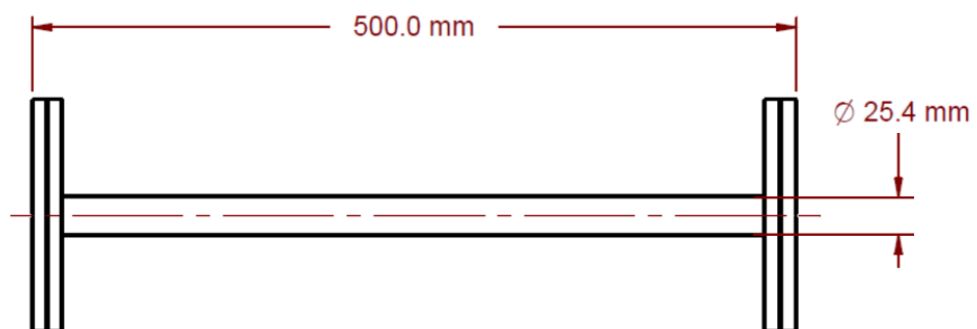
Figure 3.10 Lateral view of the diffusion channel

3.4.2 Pressure gauge

Another crucial component of this vacuum system is the pressure measurement device and pressure gauge. Pressure gauges indicate the system pressure and can be used to maintain a constant pressure for both chambers. The accuracy of the measurements highly depends on the accuracy of the pressure gauges. Therefore, all gauges require careful handling and calibration to provide accurate values [126]. The accuracy of commonly used vacuum gauges can be from 15% up to 50% uncertainty within the different ranges given by manufacturers with a rough calibration [127]. Therefore, a systematic calibration is required over the whole vacuum range.

A vacuum gauge that can encompass the entire pressure range required must consist of two separate gauges for the higher vacuum and lower vacuum ranges. The gauge for the higher vacuum range can be crudely placed in one of two categories: hot and cold ionisation detectors [128]. In principle, a hot cathode ionisation gauge is more sensitive than a cold one. The main problem with hot cathode ionisation detectors is that they are extremely fragile. As our experimental results highly depended on the accuracy of the gauges, a hot cathode ionisation gauge was selected. Edwards Active Ion Gauge (AIGX) can measure pressure from $6 \cdot 10^{-2}$ down to $6 \cdot 10^{-10}$ mbar with an accuracy of $\pm$ 15%. In addition, it is compact. Feature onboard electronics and various components (e.g. the sensor tube) are replaceable. Therefore, the Edwards AIGX gauge was selected as the gauge for the higher vacuum range (Table 3.4).

Table 3.4 Technical data of the AIGX [129]

Description	Unit	Value
Pressure range	mbar	6.6×10^{-2} to 6.6×10^{-10}
Accuracy		+/- 15%
Operating temperature	°C	0 to +40
Weight	kg	0.5

Figure 3.11 Edwards AIGX active ion gauge [130]

The most common and sensitive gauge for the lower vacuum range is the resistance-based gauge, the Pirani gauge, which can measure the pressure from atmospheric pressure to 10^{-2} mbar [71]. Although a simple Pirani technology gauge can indicate the pressure of the lower vacuum range, the more expensive wide range gauge (WRG) was selected as the gauge for the lower vacuum range. The WRG is a combination gauge, and applies to the Pirani technology for the upper-pressure range and can seamlessly switch over to an inverted magnetron for the higher vacuum range (Table 3.5). The WRG can be used to calibrate the AIGX gauge to provide more accuracy in the high-vacuum range. The calibration is discussed in Chapter 4.

Table 3.5 Technical data of the WRG [131]

Description	Unit	Value
Pressure range	mbar	Atmosphere to 1×10^{-6}
Accuracy		+/-15% < 100 mbar +/- 30% $< 10^{-3}$ mbar
Operating temperature	°C	+5 to +60
Weight	kg	0.8

Figure 3.12 Edwards WRG wide range gauge [132]

3.4.3 Gas inlet system

The gas inlet system must be able to leak a constant gas flow into the vacuum system. The simplest method of introducing gases into the vacuum system is the use of an open/close valve. The principal disadvantage of this type of valve is that it generates pressure waves in the vacuum system, which strongly affect the measurements and can even damage equipment. To remove the pressure waves, the pump capacity must be very large, and a single turbomolecular pump is insufficient. Pumps that can manage such inlet flows are extremely expensive, which is not an option. An alternative approach is to use a leak valve. Leak valves are specifically designed to control gases into the ultrahigh vacuum system and can create a small constant gas flow into the system without introducing too many pressure waves. The VAT Series 590 variable leak valve was selected as the gas inlet valve. It can precisely and reproducibly control very small gas flows into a vacuum system using a computer-controlled stepper motor (Table 3.6).

Table 3.6 Technical data of the Series 590 variable leak valve [133]

Description	Unit	Value
Leak rate	mbar·l/s	$<1 \times 10^{-10}$
Pressure range	bar	UHV to 10
Bake-out temperature	°C	<300
Controller position resolution	steps	100,000
Weight	kg	2.5

Figure 3.13 VAT Series 590 variable leak valve [133]

An important aspect is condensation. When the gas passes through the leak valve, the pressure decreases by many orders of magnitude. Because of this extreme pressure drop, gas can condense, which is particularly troublesome in the presence of water. This condensation can cause the total gas flow to become unstable. To limit this problem, the gas introduced into the system should contain as little water as possible. Therefore, we used zero-grade nitrogen as the experimental gas for the Knudsen diffusion measurements [134].
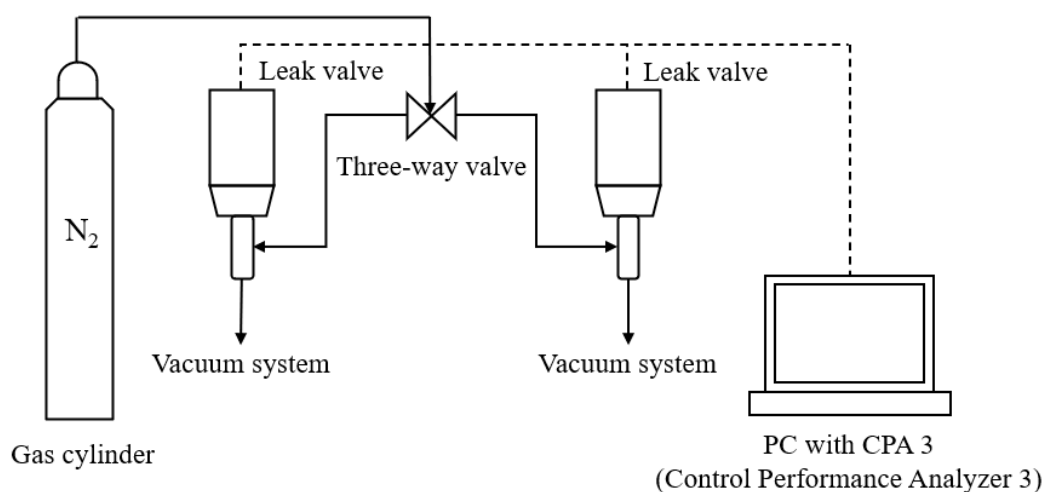
Figure 3.14 Schematic of the gas inlet system. Experimental gas (N_2) is introduced to the system *via* a leak valve. The three-way valve is used to repeat measurements from opposite diffusion directions.

3.4.4 Residual gas analyser (RGA)

To analyse the gas composition inside the vacuum system and perform leaking detection, a mass spectrometer, which is considered to be the most sensitive concentration measurement device, should be connected to the vacuum chamber [135]. As a more economical alternative, we selected an RGA for gas analysis and leaking detection. An RGA is a cheaper and smaller option to a mass spectrometer, but the principle of operation remains the same. The gas molecules are ionized, and the resulting ions are separated by a quadrupole mass filter; thus, the ion detector measures and determines the concentration according to the molecular mass [136]. The Stanford Research Systems RGA 200 was selected to provide details of the gas analysis of a vacuum system and at approximately half the price of a mass spectrometer (Table 3.7).

Table 3.7 Technical data of Stanford Research Systems RGA200 [137]

Description	Unit	Value
Mass range	amu	1 to 200
Mass filter type		Quadrupole
Minimum detectable partial pressure	mbar	5×10^{-11}
Operating range	mbar	1×10^{-4} to UHV
Operating temperature	°C	70
Bakeout temperature	°C	300
Weight	kg	2.7

Figure 3.15 Stanford Research Systems RGA200 [138]

3.5 Summary

Two stainless steel vacuum chambers regulated by two high-vacuum pump sets consisting of scroll pumps and turbomolecular pumps were connected using a 0.5-m 304L stainless steel channel. Two pressure gauges (AIGX and WRG) were located on ports welded on the front side of the chambers, and the leak valves (VAT series 590) were located on similar ports on the backside of the chambers. The RGA (RGA200) was located on the right side of the right chamber when performing leaking detection and advanced self-diffusion measurements. According to the conceptual and practical design, a combined schematic of the high vacuum system for Knudsen diffusion measurements is shown in Figure 3.16.
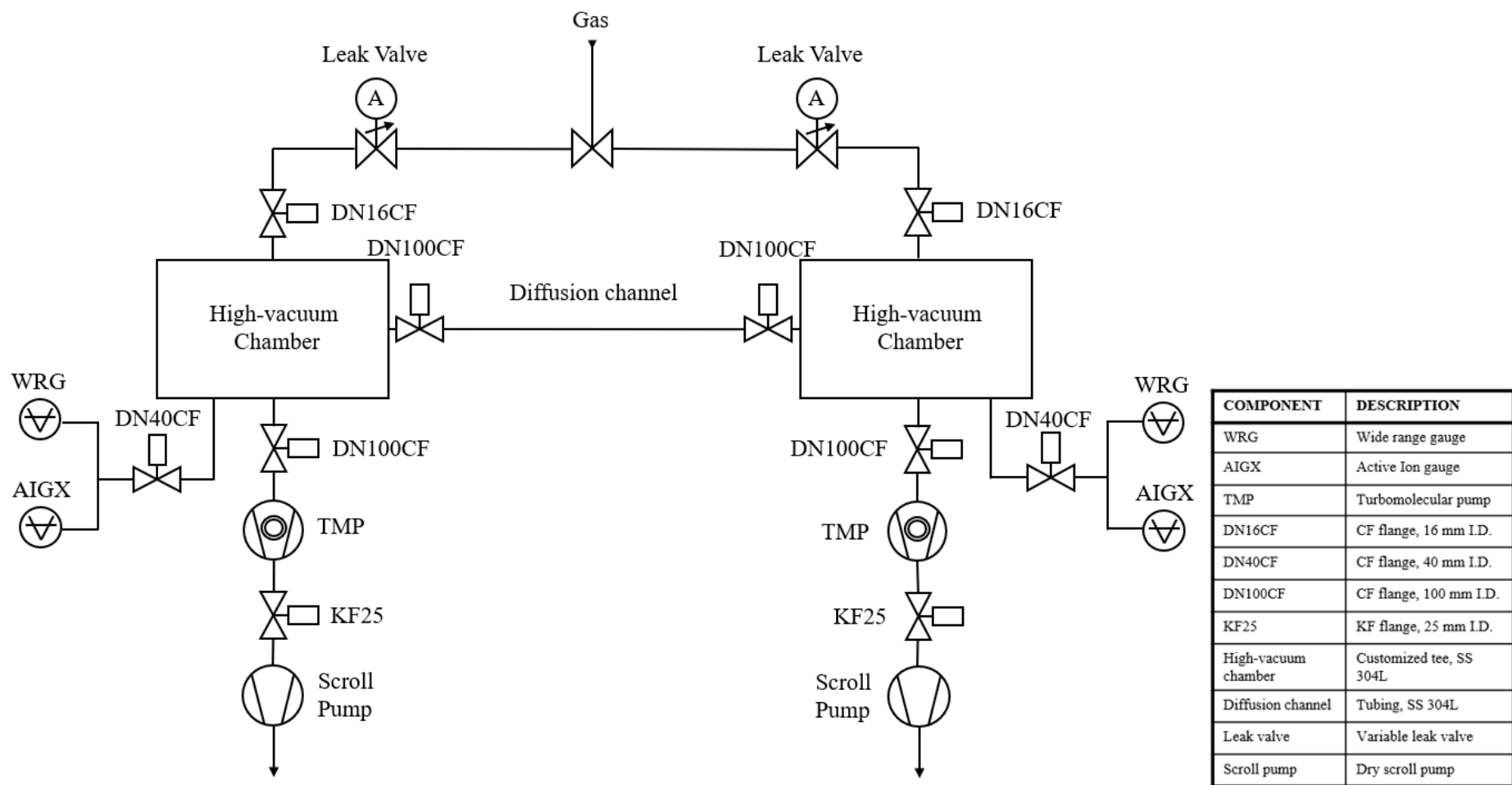
Figure 3.16 Schematic of the high-vacuum diffusion system

CHAPTER

FOUR

---

4 Vacuum calculations

Developing a high vacuum system is not easy because of the difficulties of creating a prototype system. Moreover, precisely measuring system pressures for the quantitative explanation of the Knudsen phenomenon is exceedingly more difficult than other qualitative measurements in a vacuum system. Any inconsiderate design could cause numerous errors. A practical design using theoretical and empirical methods, as discussed in Chapter 3, is limited to qualitative measurement. To investigate Knudsen diffusion in a consistent and reliable system, a more detailed design is critical. In this chapter, the necessary approaches are explained to improve the practical design. Based on this, an actual high vacuum system that could provide reliable data for the diffusion experiments was built.

4.1 Introduction

To create a detailed design of a vacuum system, including pumping speed determination and the location of the pressure gauge port on the vacuum chamber, analytical and numerical calculations should be applied. The analytical approach solves the basic vacuum equations analytically using all relevant data and can provide simple approximations for the vacuum system. In this chapter, the analytical approach is analysed for pump selection in a simplified vacuum system. The numerical approach uses the given data to solve the equations through numerical methods, which is particularly effective for complex system structures. Based on the conceptual and

practical design in Chapter 3, the numerical approach Molflow+ is explained and vacuum calculations are performed on the pumping speed selection and chamber structure design. By using both the analytical method and numerical tools, the pumping speed of the turbomolecular pump and the structure of the chamber are determined, which significantly complements the practical design to avoid empirical errors.

4.2 Analytical calculations

4.2.1 Methodology

In our vacuum system, the behaviour of gas molecules was modelled as resulting from the statistics of a certain number of molecules randomly colliding with the vacuum equipment's walls rather than among themselves, so that no viscosity is present in the system. When the gas molecules collide with the walls, an impulse change occurs, resulting in pressure [139]. For a system with constant calculable conductance and pumping speed, the analytic approach can be applied to calculate the systematic pressure profile. Three fundamental equations of a high-vacuum system are widely used for analytic calculations: the generally equilibrium pressure equation, throughput-conductance equation and effective pumping speed equation.

In the vacuum system, the generally equilibrium pressure is

$$p = \frac{Q_{\text{inlet}}}{S} \tag{4.1}$$

where Q_{inlet} is gas flow entering the vacuum system (systematic outgassing or process gas as discussed in Section 2.3.3). While the throughput-conductance equation is represented as

$$Q = C \cdot (p_u - p_d) \tag{4.2}$$

where p_u is the pressure of higher pressure area, p_d is the pressure of lower pressure area, and C is the conductance depending on the geometry and the gas velocity. The third fundamental equation, the effective pumping speed equation, is Equation 2.9. Many vacuum problems can be solved analytically by using these three equations.

To calculate the pressure profile, the vacuum system can be simplified to a long cylindrical channel (L) with two pumps connected to each side of the channel (Figure

4.1).
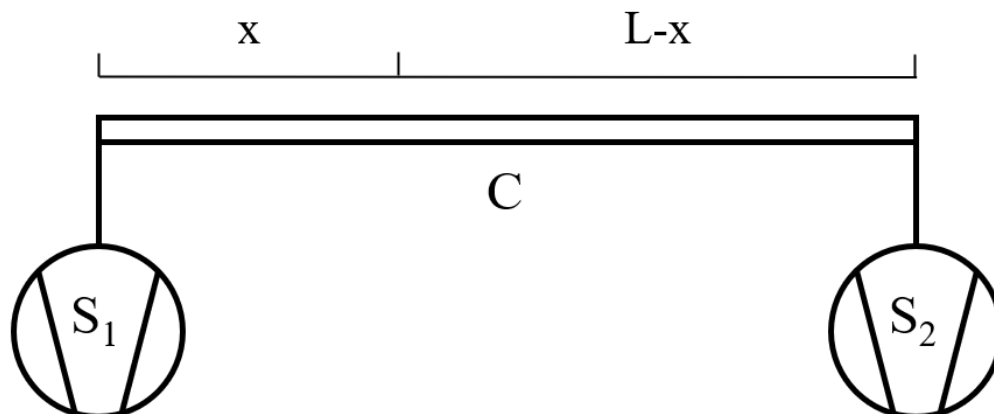
Figure 4.1 Simplified high-vacuum system for analytical calculation

As this calculation is to investigate the pressure profile of the system, no process gases are introduced into the system. Therefore, Q_{inlet} represents the uniform outgassing rate coming from the wall of the tube. The pressure at location x can be expressed by using Equation 4.1.

$$p(x) = \frac{Q_{inlet}}{S(x)} \tag{4.3}$$

The length of the tube is L, the conductance of the tube is C, the pumping speed at location x is $S(x)$. By using Equation 2.6 and Equation 2.9, the local pumping speed in the tube with conductance C is

$$S(x) = \frac{1}{\dfrac{x}{LC} + \dfrac{1}{S_1}} + \frac{1}{\dfrac{L-x}{LC} + \dfrac{1}{S_2}} \tag{4.4}$$

4.2.2 Pump selection

The outgassing rate uniformly emanates from the SS channel, which is 3×10^{-12} mbar·L/s for 304L SS. The key calculation parameters used in the analytical calculation are listed in Table 4.1.

Table 4.1 Parameters used in analytical approach

Parameter	Unit	Value
Outgassing rate, Q_{inlet}	mbar·L/s	3×10^{-12}
System conductance, C	L/s	3.58
Length of the channel, L	cm	50
Pumping speed of left pump S_1	L/s	54
Pumping speed of right pump, S_2	L/s	54

The system conductance (C) is 3.58 L/s, calculated using Equation 2.26. The length between two pump groups (L) is 50 cm, and the pumping speed of both pumps are 54 L/s as an example. Substituting these parameters into Equation 4.3 and 4.4, a parabolic pressure profile is shown in Figure 4.2.
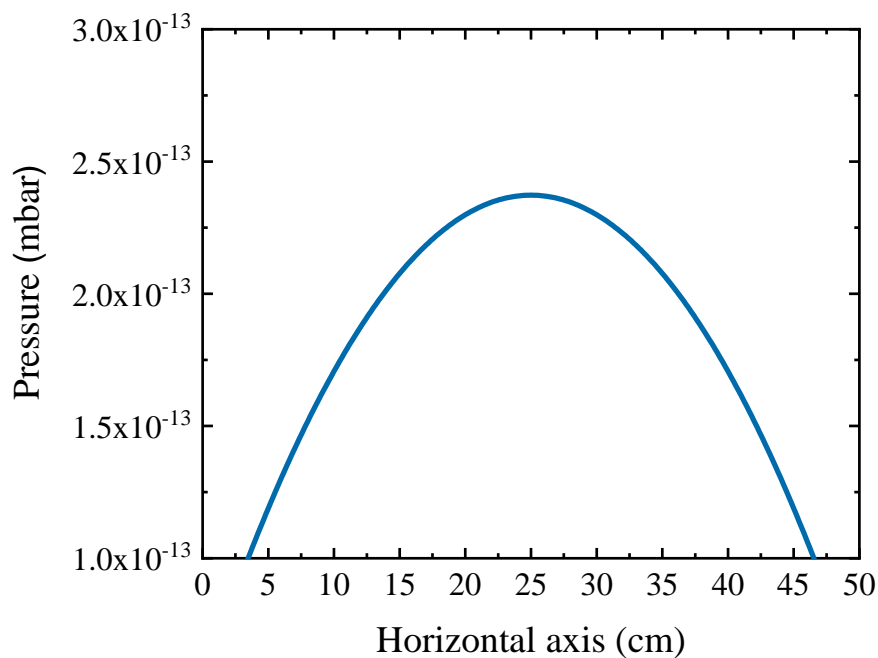
Figure 4.2 Pressure profile of simplified high vacuum system with a pumping speed of 54 L/s

The pressure profile obtained using the analytical approach is approximate as the actual structure of the high vacuum system is more complicated, because it does not consider the resistance in the vacuum chambers. By using these analytical calculation formulas, we can simply change parameters such as the pumping speed, structure, and material of the system to determine the best design performance. Edwards has five types of

commercial turbomolecular pumps on the market, and their pumping speeds are shown in Table 4.2.

Table 4.2 Pumping speeds (Hydrogen) for turbomolecular pumps [140]

Pump types	Unit	Pumping speed
nEXT85	L/s	54
nEXT300	L/s	280
nEXT400	L/s	325
nEXT730	L/s	715
nEXT930	L/s	735

The analytical approach can be used to easily analyse the simplified vacuum system and perform pressure profile calculations. Figure 4.3 shows the pressure profiles of the simplified high vacuum system with different pumping speeds. The results indicate that even the nEXT85 turbomolecular pump with the smallest pumping speed can evacuate the system down to 10^{-13} mbar and provide almost the same performance as higher pumping speed pumps, and the pressure profiles highly depends on the outgassing rate.

As discussed in Chapter 2, the conductance of a simple circular cross-section tube can be calculated using Equation 2.26 and Figure 2.6 as the reference. However, determining the system conductance analytically becomes impossible for complex structures. Therefore, calculating the pressure profile for complicated vacuum systems is extremely difficult and forced simplification can result in large deviations, which is inaccurate to estimate the pressure profile for system design purposes. For arbitrary geometries in which the system conductance is not calculable, numerical approaches should be applied to obtain more reliable pressure profiles, as no analytical solution exists.
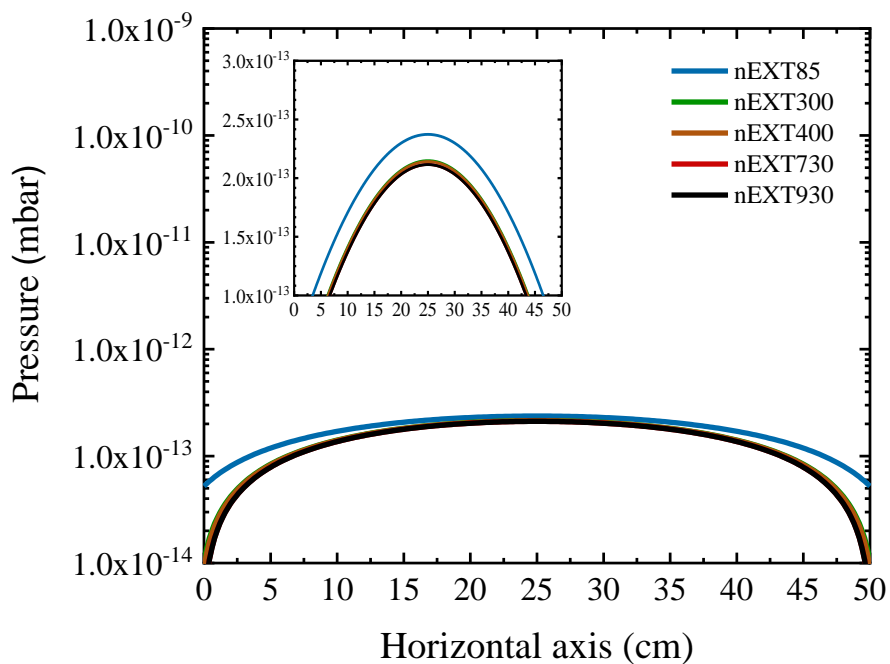
Figure 4.3 Pressure profiles of a simplified high vacuum system with different pumping speeds

4.3 Numerical approach to vacuum calculations

When the mean free path of a gas molecule is larger than the characteristic length of the system, the gas dynamics are dominated by molecular collisions with the walls. Under this condition, a numerical method can be applied to perform vacuum calculations. Molflow+ is a numerical method that employs Monte Carlo simulations to implement the formulae of the kinetic theory of gases [141]. This enables us to obtain approximate solutions for a vacuum system. The introduction of Molflow+ and the simulation of the pressure profile is presented below to determine the chamber design and pump selection.

4.3.1 Molflow+

4.3.1.1 Introduction

Molflow+ is a well-known simulator in vacuum technology developed at the European Organization for Nuclear Research (CERN) that enables the calculation of steady-state pressure profiles and conductance in arbitrary geometries under high and ultra-high vacuum conditions [141]. The name Molflow was derived from 'free molecular flow',

in which the mean free path of the gas molecules is much larger than the characteristic size of the vessel, and the intermolecular collisions can be neglected. In this condition, the test-particle Monte Carlo (TPMC) method is applied to simulate particle flying traces. The Monte Carlo simulator calculates the pressure profile by launching many particles in the vacuum system, where the collisions between a test particle and the wall follow Lambert's law. It enables solving transport problems, particularly when the analytical solutions are difficult to implement.

The initial version of the Molflow+ was developed by Kersevan in 1990 [142]. In 2007, a new version was released with the original algorithm but in a modern environment (C++ based code) [143]. A few years later, large updates were applied to Molflow+ in CERN [144, 145]. These updates significantly shortened the time required to build a 3D model, which enabled users to import a stereolithography (STL) file from other computer-aided design (CAD) programs, such as SOLIDWORKS, AutoCAD, and Rhino.

4.3.1.2 Methodology

Molflow+ is a TPMC simulator for vacuum systems to calculate many trajectories of gas molecules [146]. These trajectories are straight lines between the vacuum walls, and they are determined by ray tracing from the outgassing point to the pumps. Molflow+ records all the collisions between gas molecules and the wall and stores them in memory. Subsequently, the number of collisions on the geometry (called facets in Molflow+) are exported [147]. Based on these collisions, physical quantities such as pressure and density are calculated and updated on the screen every second. To fully understand the methodology of Molflow+ simulation, the steady-state algorithm will be explained next.

For a vacuum system, gas particles generally come from the walls that frequently represent the outgassing rate in vacuum technology or from gas inlet ports. In Molflow+, both gas-particle inlet sources are defined as outgassing with the unit mbar·L/s. Hence, the gas-particle inlet rate can be calculated by using the ideal gas law and Equation 4.5:

$$\frac{dN_{real}}{dt} = \frac{d\frac{pV}{RT}}{dt} = \frac{Q_{outgas}}{RT} \tag{4.5}$$

where N_{real} is the total amount of real particles on the source facets, T is the temperature of the source facets, and Q_{outgas} is the outgassing of all gas-particle inlet sources. Hence, the total number of gas particles entering the vacuum system can be represented as $\sum \frac{dN_{real}}{dt}$. Simulating all real particles is an extremely slow process. To avoid this, the Molflow+ algorithm introduces the concept of test particles, where each test particle can represent many real ones and the progress of a test particle can be followed through a field of target molecules [148, 149]. By applying a test particle Monte Carlo technique, the calculations are simplified and the storage requirements are reduced. As a result, the simulation duration is significantly shortened. Additionally, the concept of $K_{\frac{real}{test}}$ is introduced and is used for pressure calculations:

$$K_{\frac{real}{test}} = \frac{\sum \frac{dN_{real}}{dt}}{N_{test}} \tag{4.6}$$

where N_{test} is a total number of test particles.

After generating new particles, the direction of a particle rebounding from a surface is governed by Knudsen's cosine law, in which the direction is independent of the incident direction. The velocity of the gas particles follows the Maxwell–Boltzmann model. When the direction and velocity of particles are calculated, a ray-tracing algorithm is applied to determine the next collision point. When the particle collides with the pump facet, it can be pumped out from the system, generating a new particle from the outgassing facet, or the particles rebound from the facets. This procedure depends on the sticking factor (probability of absorption for the impinging particle) of the hit facet [141]. The sticking factor is related to the pumping speed according to the equation

$$S = s \cdot \frac{1}{4} \bar{v} \cdot A_{facet} \tag{4.7}$$

where S is the pumping speed defined by the Molflow+ user, s is the sticking factor representing the ratio of the number of adsorbed molecules to the total number of molecules that impinge upon the surface, $\bar{v}$ is the average molecule speed, and A_{facet} is the area of the facet. Molflow+ registers all the hits by the particles and momentum changes, then calculates the impingement rate and pressure based on these numbers.

Impingement rate

The impingement rate (z) is the number of collisions on a facet per second on a unit area:

$$z = \frac{N_{hit} \cdot K_{\frac{real}{test}}}{A} \tag{4.8}$$

where N_{hit} is the number of test particles that hits on the facets, and A is the area of the facet.

Pressure

Pressure p is the ratio between the sum of the momentum changes and the facet area. The sum of momentum changes can be express by the total perpendicular momentum changes:

$$mv_{\perp} = mv \cos \theta \tag{4.9}$$

where $v_{\perp}$ the perpendicular velocity, and θ is the incident angle of test particles. To obtain the real pressure, the sum of perpendicular momentum changes must be scaled up by the $K_{\frac{real}{test}}$ ratio. Hence, the pressure of the facet area can be expressed by using Equation 4.10:

$$p = \frac{\sum dI}{dt \cdot A} = \frac{\sum I_{\perp} \cdot K_{\frac{real}{test}}}{A} \tag{4.10}$$

where $I_{\perp}$ is the perpendicular momentum change.

4.3.1.3 Simulation procedures

The Molflow+ steady-state algorithm is applied to the calculations. To determine the physical quantities on the facets, a continuous inlet flux of specific gas particles to the system should be defined first. Subsequently, the pumping speed, pump location, and temperature must be defined based on reality.

The Molflow+ simulation procedures consist of four steps:

1) Generating or importing the geometry

Two methods to build the simulation geometries are generating them using a Molflow+ built-in 3D geometry editor and importing a standard STL (ASCII) file from a CAD program.

2) Setting up simulation parameters

Defining the physical properties of the vacuum system, such as temperature, gas, and opacity of facets. In addition, the particle inlet (outgassing rate) and pump properties (location, pumping speed, etc.) should be defined.

3) Setting up measurement facets

To derive useful simulation results, creating one or few indication facets is necessary, which enables the user to observe physical quantities more directly in the form of colours on the geometry (facets) or plotting figures.

4) Running the simulation

When everything is ready, Molflow+ traces the trajectories of virtual gas particles from the inlet until they leave the system. The displayed results are updated every second, and the calculated values, profile plots, and textures fluctuate with each screen update. Molflow+ enables users to control the running time and decide when the results are sufficiently accurate.

A STL file (from SOLIDWORKS)

Importing the geometry

Setting up parameters
(temperature, gas, opacity etc.)

Defining the measurement facets

Simulation
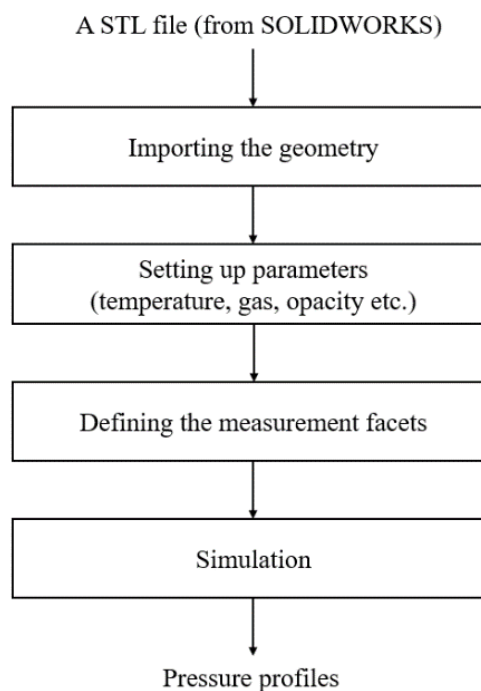
Pressure profiles

Figure 4.4 Block diagram of pressure profiles simulation

Calculating the pressure profiles on different facets can optimise the vacuum design in three aspects: the dimensions of the vacuum chamber, pressure gauge location, and turbomolecular pump selections.

4.3.2 Simulations on vacuum chamber design

4.3.2.1 Post-processing in Molflow+

Before estimating the performance of the vacuum chamber using Molflow+, the model of vacuum chambers with different locations of the gauge ports must be created first. The gauge port can be distributed in the centre of the chamber's horizontal axis or near the junction between the chamber and channel. Hence, a 3D model with both designs is created to compare the pressure difference. As discussed in Section 3.2.3, the main body of the chamber is a DN100 tee and the diameter of the gauge port is 40 mm.

In Molflow+, the geometry under study is described by a set of polygons (facets) representing vacuum walls. All polygons have user-defined physical properties, such as outgassing rate, opacity, and temperature. As the geometry of the conceptually designed vacuum chamber is not trivial and difficult to generate using the Molflow+ geometry editor, 3D models are imported from the outsourced CAD software SOLIDWORKS. Figure 4.5 shows the 3D vacuum chamber model with two gauge ports in SOLIDWORKS.
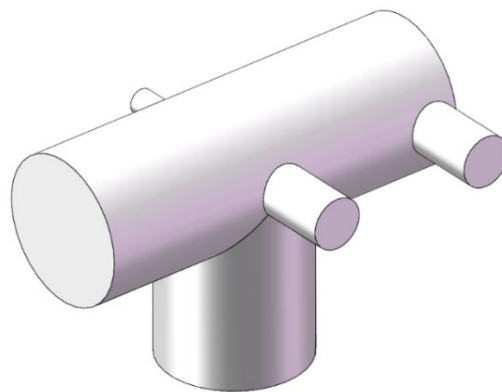
Figure 4.5 Vacuum chamber 3D models in SOLIDWORKS

As Molflow+ accepts the STL file format only, the initial designed 3D model by SOLIDWORKS should be converted to an STL file before importing it into Molflow+. However, simplifying an STL-format 3D model from other CAD software is not a trivial process. The STL file describes the surfaces of the 3D model using many triangles. Figure 4.6 shows the vacuum chamber with two gauge ports in STL format, in which one port is in the centre of the chamber's horizontal axis and another one is

near the junction. Figure 4.6 contains too many unnecessary triangles that can complicate the physical properties defining the process for specific facets. Molflow+ can automatically merge triangles into a simple polygon by detecting adjacent and coplanar triangles. This procedure can significantly reduce the error caused by a manual modification to prevent leaks, which represent a geometrical error due to too coarse 'collapsing' (see below), leading to incorrect joints.
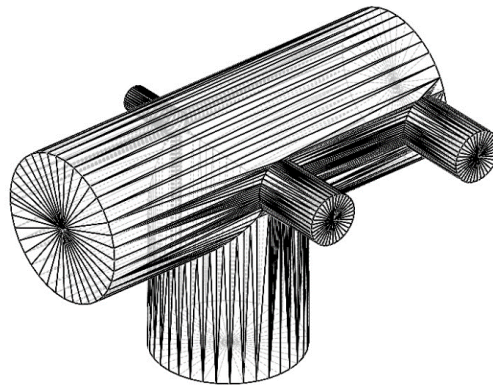
Figure 4.6 Vacuum chamber 3D model in STL format

Figure 4.7 compares the unmodified and Molflow+-modified gas ports facets of the vacuum chamber. By applying the 'collapse' function in Molflow+, a surface originally consisting of several small facets is integrated into a large one. Having a simplified vacuum chamber with fewer facets by merging coplanar triangles will significantly reduce the computation time.
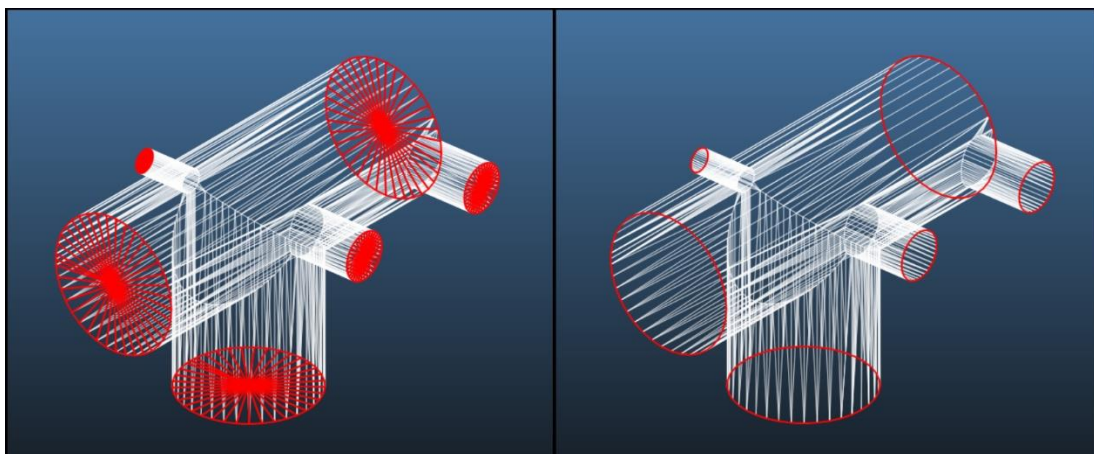
Figure 4.7 a) Unmodified port facets; b) Molflow+-modified port facets

4.3.2.2 Pressure simulations on gauge port

When the 3D models are ready for simulation, some crucial parameters should be defined first, such as pumping speed, outgassing rate, temperature, and molecular mass. The molecular mass as the global parameter must be defined first, then the other parameters should be set for each facet. In reality, hydrogen is always the main gas load in a high-vacuum system [150]. Hence, the simulated gas molecules were of hydrogen with a 2-g/mol molecular mass and the simulated pressure was obtained as an approximation to the total pressure of the chamber. The port at the vertical axis was the pumping port. The pumping speed was set to 54 L/s, which is the smallest available pumping speed for H_2 of the Edwards turbomolecular pump on the market (Table 4.2). The hydrogen specific outgassing rate for stainless steel after a 150 °C bake-out used in this simulation was 3.0×10^{-12} mbar·L/s/cm^2 [109]. The simulation temperature was set to 20 °C. All related parameters are summarized in Table 4.3. The pressures were simulated on the facets where the pressure gauges were connected.

Table 4.3 Parameters of pressure simulations on gauge port

Description	Unit	Value
Pumping speed	L/s	54
Outgassing rate	mbar·L/s/cm^2	3.0×10^{-12}
Temperature	°C	20
Molecular mass	g/mol	2

For the two-gauge ports chamber, the model had 705 facets and 482 vertices. A two-sided transparent facet was created in the centre of the chamber along the horizontal axis, which enabled molecules to pass through to measure the pressure profile of the chamber. All these facets set the parameters before the simulation. The calculation of this two-gauge ports model required approximately 18 h and more than 1.5×10^{10} hits were performed, which was conducted using a Lenovo Air 13 IWL with 1.99 GHz Intel (R) Core (TM) i7-8565U CPU and 8 GB RAM. Figure 4.8 shows the 3D chamber model, in which the green lines depict the test particle trajectories. To visualize the pressure in the centre of the system, a "dummy" two-sided transparent facet in the centre of the model is added (facet with red sides); the pressure profile of the system could also be obtained on this "dummy" facet.
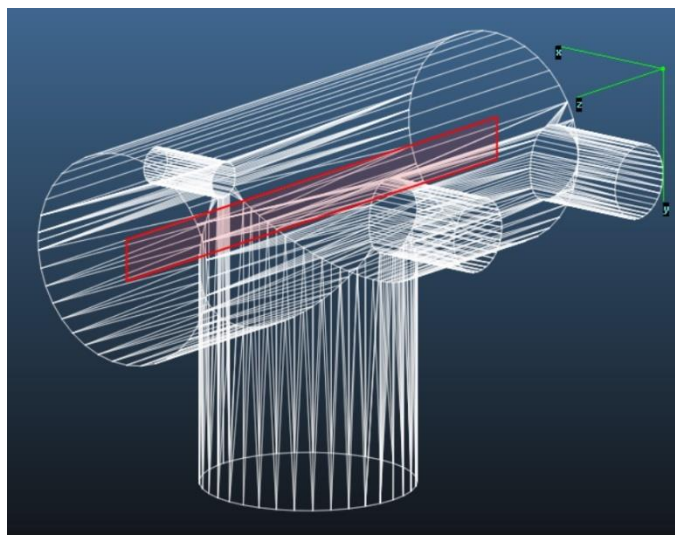
Figure 4.8 3D chamber model in the simulation process

The results of the pressures on the two gauge ports facets were 1.375×10^{-10} mbar (right-side port) and 1.369×10^{-10} mbar (centre port). The simulation results indicated that the two gauge port pressures were almost identical, with approximately 1×10^{8} hits performed on each facet. The pressure texture of the Molflow+ simulated model is presented in Figure 4.9.
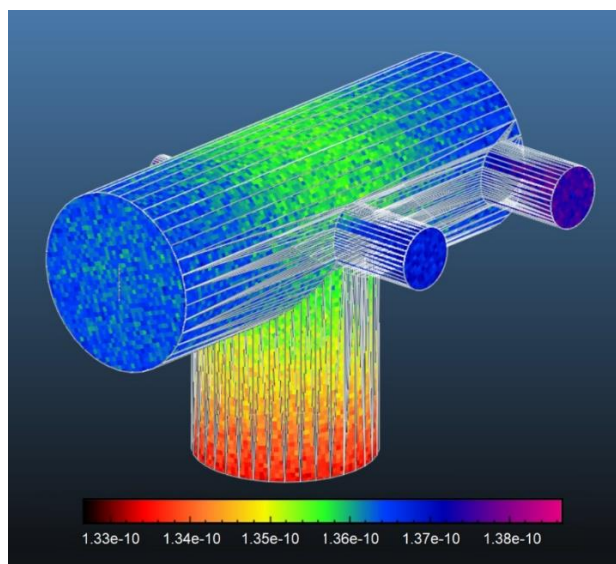
Figure 4.9 Pressure textures within Molflow+

The pressure profile of the vacuum chamber is shown in Figure 4.10, for which more than 1.2×10^{8} hits were calculated on the two-side transparent facet.
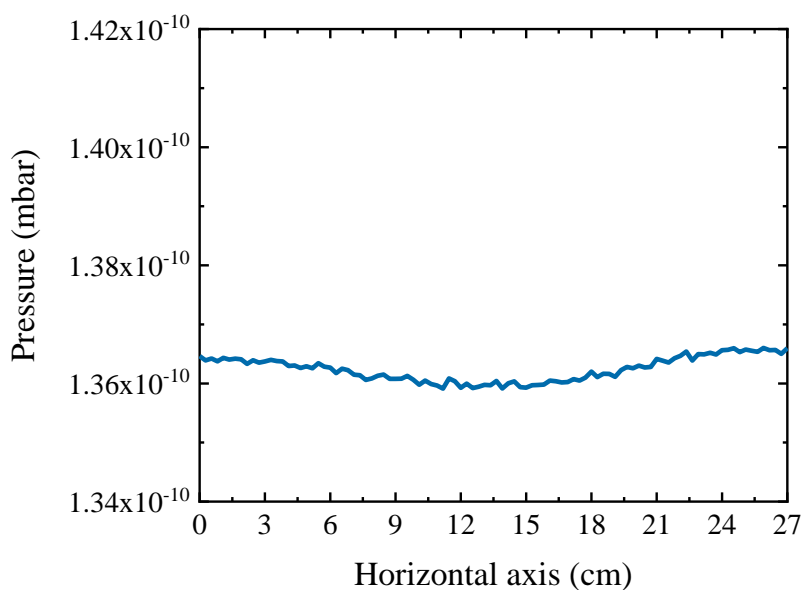
Figure 4.10 The pressure profile along the horizontal axis for a chamber of 27 cm length, as the length of a standard three-way cross is approximately 27 cm.

The pressure profile in Figure 4.10 indicates that the pressure distribution in the vacuum chamber was almost uniform. The pressure difference between the side and centre of the chamber was less than 0.5%, and the average pressure of a chamber with a pumping speed of 54 L/s was 1.362×10^{-10} mbar. Compared with the pressures of the gauge port facets (Table 4.4), the pressures of both designs were close to the average pressure of the chamber, 1.362×10^{-10} mbar. Additionally, the divergence of the 'centre port' pressure from the actual pressure of the chamber was smaller than that of the 'right-side port' pressure.

Table 4.4 Simulation results on two gauges ports with different total hits

Description	Right-side port pressure	Centre port pressure	Chamber average pressure
1.5×10^{10} hits simulation	1.375×10^{-10}	1.369×10^{-10}	1.362×10^{-10}
3.0×10^{10} hits simulation	1.374×10^{-10}	1.368×10^{-10}	1.362×10^{-10}
Relative error	0.07%	0.07%	0.03%

To obtain more reliable results, the simulation was repeated for more hits on the chamber facets (Figure 4.11). The simulated average pressure along the horizontal axis with more hits was approximate 1.362×10^{-10} mbar with less than 0.03% relative error.

Figure 4.11 shows the chamber pressure profile comparison of the 1.5×10^{10} hits and 3×10^{10} hits simulations. The comparison of gauge port pressures between the two simulations with more hits is also shown in Table 4.4. According to the simulation results, the pressure at the centre gauge port was closer to the average pressure of the chamber with an approximate 0.5% difference compared with the right-side gauge port. Therefore, the location of the gauge port should be in the centre of the horizontal axis of the chamber.
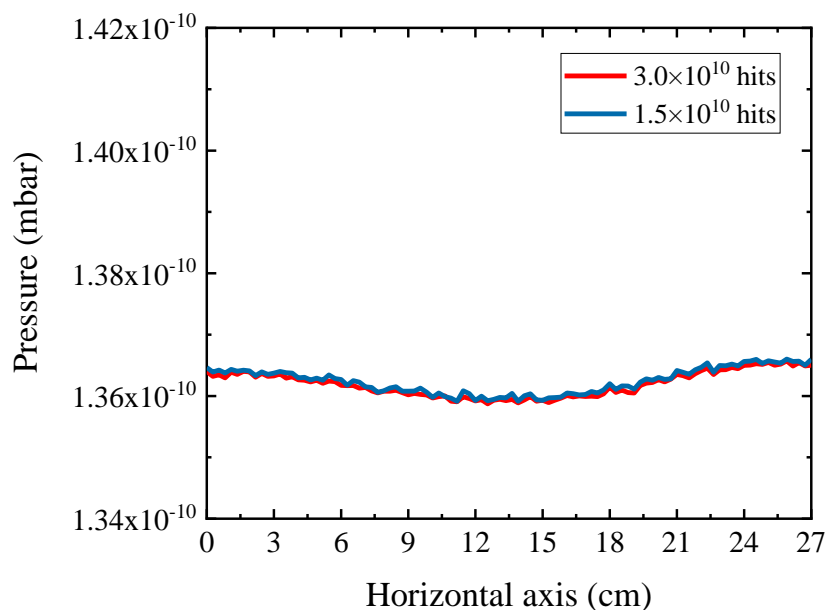
Figure 4.11 Chamber pressure profiles with different hitting numbers

4.3.2.3 Summary

The vacuum chamber consisted of a standard DN100 304L SS three-way cross with CF flanges as the main body, a gas inlet port, and a gauge port. The gas inlet port and gauge port were located opposite each other in the centre of the chamber horizontal axis, and the flange sizes were DN16CF and DN40CF for the gas inlet port and gauge port, respectively. The lateral and top views of the vacuum chamber are shown in Figure 4.12 and Figure 4.13.
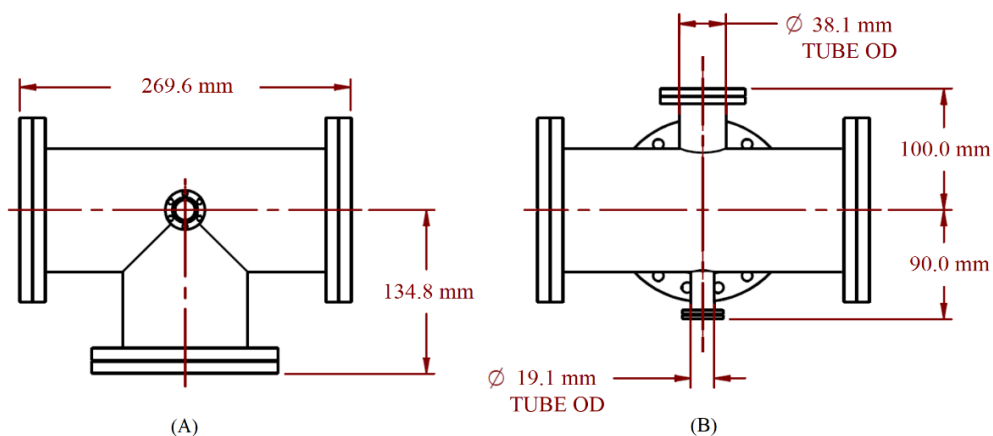
Figure 4.12 Vacuum chamber: (A) Lateral view; (B) Top view
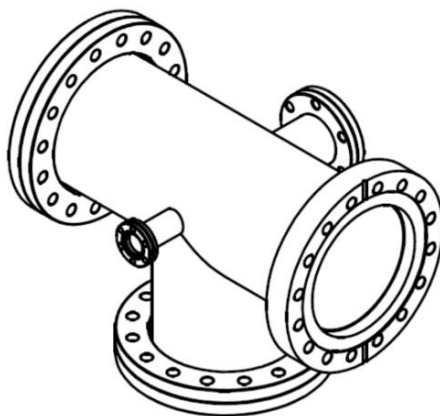
Figure 4.13 304L SS vacuum chamber

4.3.3 Simulation for pump selection

4.3.3.1 Post-processing in Molflow+

As explained in Chapter 3, the main requirement for the pump selection is to maintain the system pressure at 10^{-8} mbar. Hence, we performed simulations for pumps with different pumping speeds to determine the most appropriate turbomolecular pump. The 3D model of the high vacuum system was introduced from SOLIDWORKS (Figure 4.14).
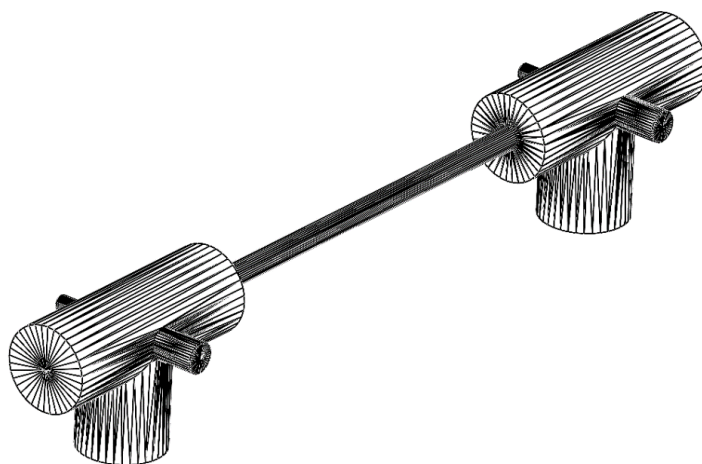
Figure 4.14 Vacuum system 3D model in STL format. The length of a chamber and the tube are 27 cm and 50 cm, respectively, thus the total length of the system is 104 cm.

Molflow+ measures the pressure on the walls of the vacuum system; however, the pressure profile inside the system interested us more. Hence, an extra facet was created first for the measurements. Figure 4.15 depicts the created facet for the pressure measurements (z-axis direction) generated by the create facet from vertices. As the facet was in the middle of the system, it had to be two-sided and transparent to permit particles to pass through.
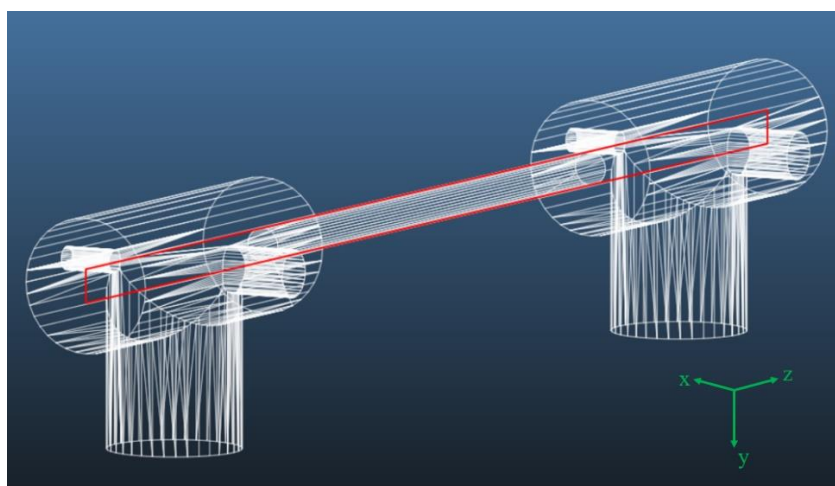
Figure 4.15 Transparent facet for pressure measurements

4.3.3.2 Pressure profile simulation

Now that the 3D model of the high vacuum system has been properly set up (applying the "collapse" function) and is ready for diffusion simulations (Figure 4.15), the system

pressure profile should be predicted to evaluate the turbomolecular pump selection. For an SS vacuum system, as soon as the outgassing of water vapour is significantly reduced by bake-out or long pumping, hydrogen will eventually become the dominant gas source of the system. Therefore, the hydrogen pressure profile was simulated as an approximation of the system pressure. The turbomolecular pumps were assigned to the facets shown in Figure 4.16.
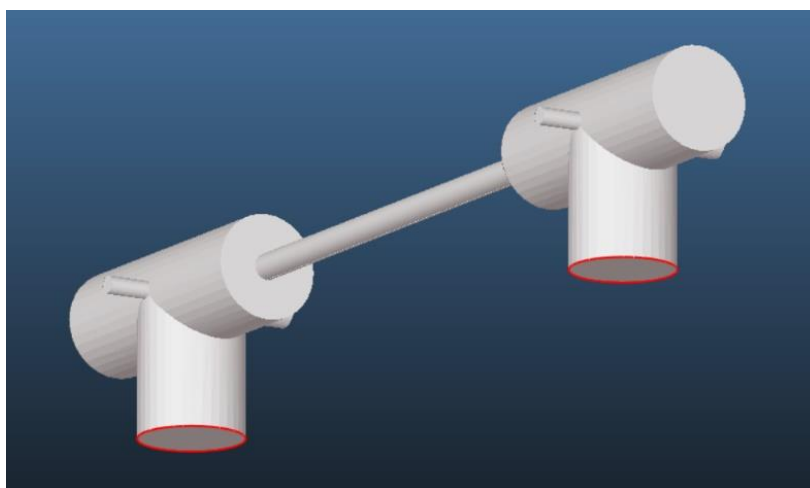
Figure 4.16 Pumping facets

The outgassing rate of stainless steel after a 150 °C, 24 h bake-out is 3.0×10^{-12} mbar·L/s/cm^2 [109], which was defined for all surface facets of the system. Five commercial turbomolecular pumps with different pumping speeds were simulated (Table 4.2). The model temperature was defined as 20 °C based on the actual lab temperature.

The hydrogen pressure profile shown in Figure 4.17 indicates that the H$_2$ partial pressure could attain 10^{-10} mbar by the smallest capacity Edwards turbomolecular pump available (nEXT85), with a pumping speed of 54 L/s. The simulation result indicated that the pressure was not identical in the entire system; the pressure in the centre of the channel was slightly higher than that in the chambers, and the highest pressure was 2.13×10^{-10} mbar. However, the orders of magnitude remained the same for the entire system. The textures of the pressure are shown in Figure 4.18 for the 1.5×10^{10} hits simulation. As hydrogen was the largest contributor to the ultra-high vacuum regime, the system pressure was approximately equivalent to the hydrogen partial pressure for our estimation. Hence, the system pressure ranged from 1.75×10^{-10} to 2.13×10^{-10} mbar.
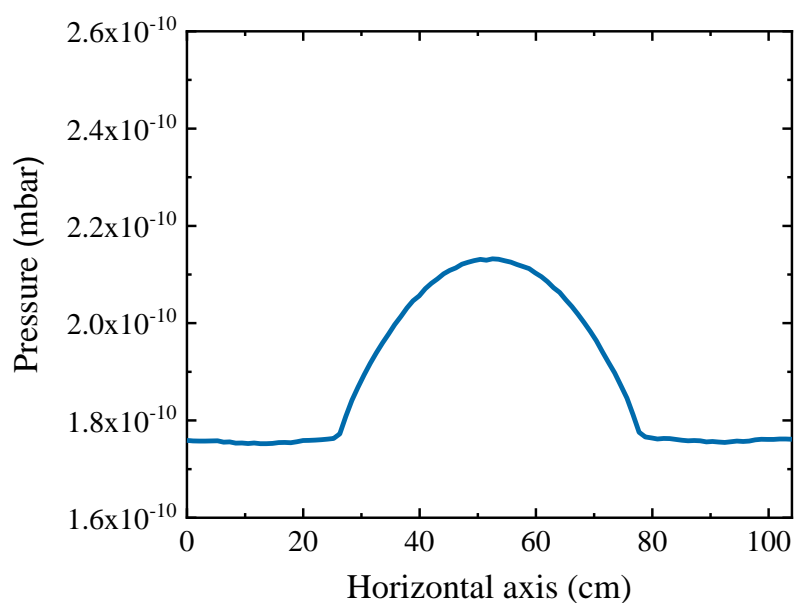
Figure 4.17 Hydrogen pressure profile of the high vacuum system with a 54 L/s pumping speed (Edwards nEXT85 turbomolecular pump)
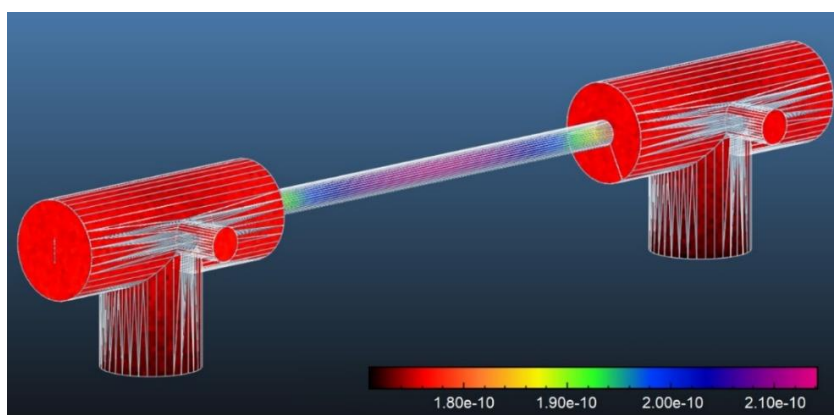
Figure 4.18 Pressure texture of the vacuum system with a 54 L/s pumping speed

Additionally, the simulation results of other types of turbomolecular pumps applied in the system are shown in Figure 4.19. As the simulation results show, all turbomolecular pumps could maintain system pressure below 1×10^{-9} mbar. Table 4.5 shows the relative errors of the results with higher simulation hit numbers (3.0×10^{10} hits), and the relative errors were observed to be extremely small.
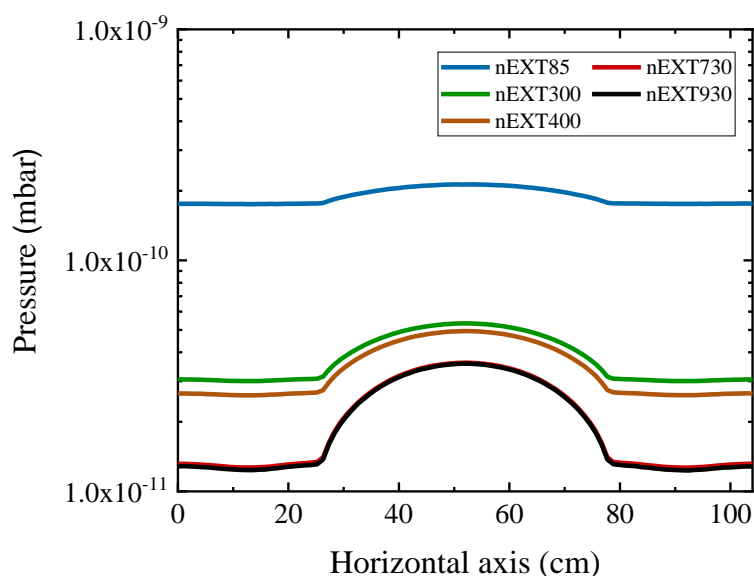
Figure 4.19 System pressure profiles for different turbomolecular pumps

Table 4.5 Relative errors for turbomolecular pumps simulations (1.5×10^{10} hits & 3.0×10^{10} hits)

	nEXT85	nEXT300	nEXT400	nEXT730	nEXT930
Relative error	0.4%	0.5%	0.4%	0.4%	0.5%

The previous simulation results indicated that the nEXT85 turbomolecular pump is sufficient to achieve an ultra-high vacuum with no other interferences. As introduced in Chapter 2, the setup would eventually be applied with complex 3D-printed structures. For the commonly used 3D-printed polymers, the outgassing rate is frequently much higher than that of 304L stainless steel. Therefore, we cannot neglect the effect of 3D-printed channels on the system pressures when we select the pump components. Thus, the pumping capacity of the nEXT85 turbomolecular pump may not be sufficient to pump out the residual gases inside the 3D-printed channels. To estimate the effects, more simulations must be performed.

Polytetrafluoroethylene (PTFE) is commonly used in vacuum systems [151], and its outgassing rate is lower than that of other 3D-printing polymers [152]. We used PTFE as an example for the simulations. Therefore, the outgassing rate of the PTFE diffusion channel between two chambers was 3.3×10^{-7} mbar·L/s/cm^2 [109], so that the facets on the diffusion channel were set to this value. In addition, all the facets on the vacuum

chambers remained the same with an SS outgassing rate of 3.0×10^{-12} mbar·L/s/cm^2. To obtain the pressure profiles with different turbomolecular pumps, the simulation lasted 15 h and more than 1.5×10^{10} hits were performed. The simulation results with PTFE 3D-printed parts in the channel are shown in Figure 4.20.
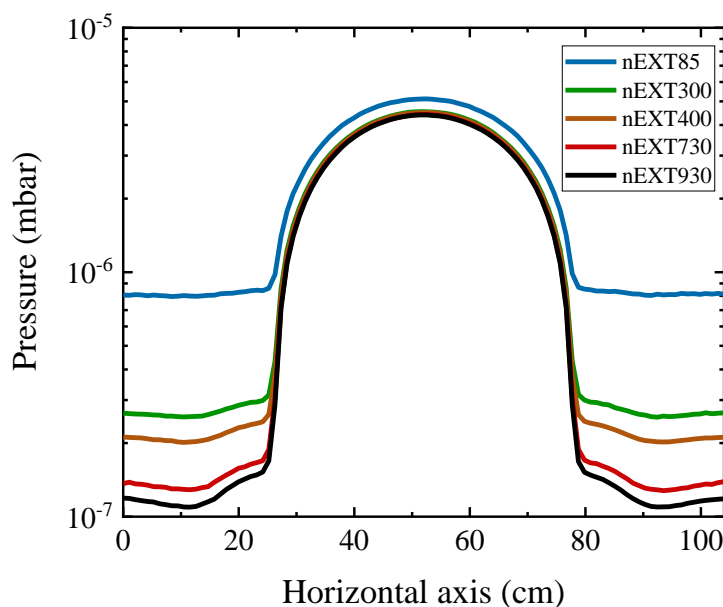
Figure 4.20 System pressure profiles with PTFE 3D-printed parts inside the vacuum channel

Figure 4.20 shows that the pressures of the vacuum channel with PTFE were nearly identical for all types of turbomolecular pumps. The ultimate pressures of the vacuum chambers differed but were still in the same order of magnitude. As Knudsen diffusion occurs in the vacuum channel, the pressure profiles of the channel part interest us. The simulation results demonstrated that the performances of the turbomolecular pumps only have a slight effect on the pressures inside the channel when high outgassing 3D-printed polymers are used. As a result, no significant performance differences between turbomolecular pumps were observed.

Figure 4.21 compares the performances of the nEXT85 turbomolecular pump in a pure SS system and SS system with a PTFE channel. Significant pressure differences were observed between the two systems equipped with the same pump. The results indicated that the pressure profiles highly depend on the outgassing rate of the inserted 3D-printed channel. Therefore, prudently selecting the material of the 3D-printed structure is

crucial for the pressure profile of the vacuum system rather than the pump selection.
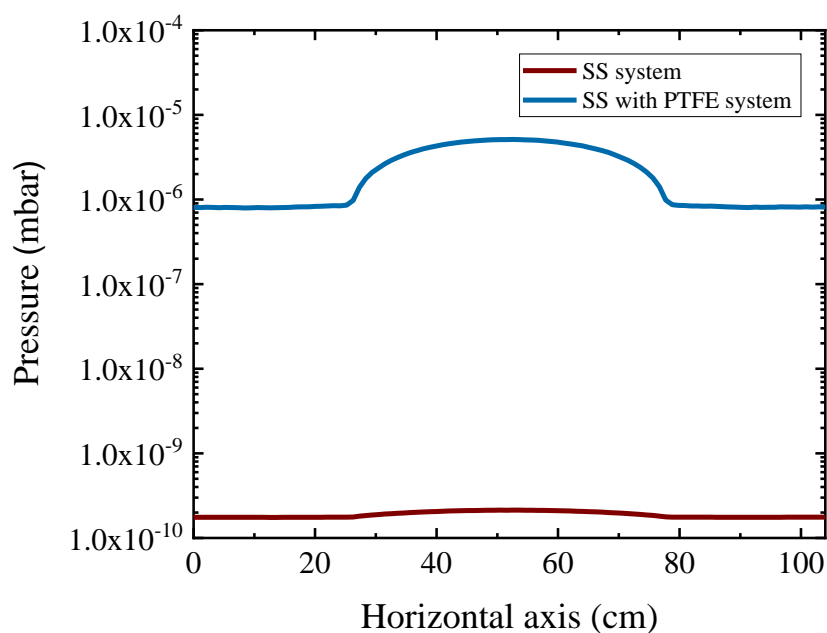
Figure 4.21 Comparison of the pressure profiles between the SS system and SS system with PTFE

According to the simulation results in Figures 4.20 and 4.21, no significant performance differences between turbomolecular pumps were observed, and the ultimate pressures depended on the outgassing rate of the system. Therefore, the lowest speed nEXT85 turbomolecular pump was selected as a candidate for our system. However, the available inlet flange sizes are NW40, DN63 ISO-K, DN63CF, and DN100 ISO-K, which would require reducing the flanges to connect to our DN100CF chamber. Consequently, it would result in extra conductance loss, resulting in a lower effective pumping speed.

The nEXT300 pump is slightly more expensive than the nEXT85 pump but is equipped with a standard DN100CF flange. No additional flange converters are required. Other turbomolecular pumps such as nEXT400, 730, and 930 pumps have larger pumping speeds, which is theoretically more desirable for a vacuum system. However, the simulation results indicated that the nEXT300 pump can achieve a virtually equivalent performance to the higher pumping speed turbomolecular pumps in our vacuum system with a 3D-printed structure. Additionally, the price would increase significantly from £7k to more than £15k for a large turbomolecular pump. Therefore, the nEXT300 pump

was selected as the high-vacuum pump for our vacuum system.

4.3.3.3 Summary

According to the simulation results and practical requirements, we selected the nEXT300 pump as the main high-vacuum pump in our vacuum system (Figure 4.22). The nEXT300 turbomolecular pump connected with the Edwards nXDS6i dry scroll pump constituted the high-vacuum pump set, which has proven to sufficiently pump the system down to 10^{-11} mbar without other interferences. The technical data of the nEXT 300 turbomolecular pump are shown in Table 4.6.

Table 4.6 Technical data of Edwards nEXT 300 [153]

Description		Unit	Value
Inlet flange			DN160CF
Backing ports			NW25
Inlet Pumping Speed	N_2		300
	He	L/s	340
	H_2		280
Critical fore-vacuum pressure		mbar	9.5
Normal rotational speed		rpm	60,000
Start time to 90% speed		sec	145
Mass		kg	8.5

Figure 4.22 Edwards nEXT 300D turbomolecular pump

CHAPTER

FIVE

5 Validation of the high vacuum system

5.1 Introduction

For the initial design of a novel high vacuum system, conceptual and practical designs are necessary. Additionally, analytical and numerical calculations should be applied as complements to provide more precise predictions for the vacuum performance based on actual data. Integrating all the mentioned design principles, a high vacuum system can be constructed without too many empirical errors and unnecessary costs. In this chapter, system integration is discussed first. Subsequently, the leaking tests that were performed are described. Finally, the calibration of leak valves and pressure gauges are explained.

5.2 High vacuum system integration

5.2.1 Ultra-high vacuum diffusion apparatus (UHV-DA)

The well-designed ultra-high vacuum system for Knudsen diffusion experiments consisted of four main units: a gas inlet unit with a VAT Series 590 leak valve, a vacuum system unit with a uniquely designed vacuum chamber, a detection unit consisting of two types of pressure gauges on each chamber, and the pumping unit, which comprised an Edwards nEXT300 turbomolecular pump as the high-vacuum pump and nXDS6i as the fore-vacuum dray scroll pump.
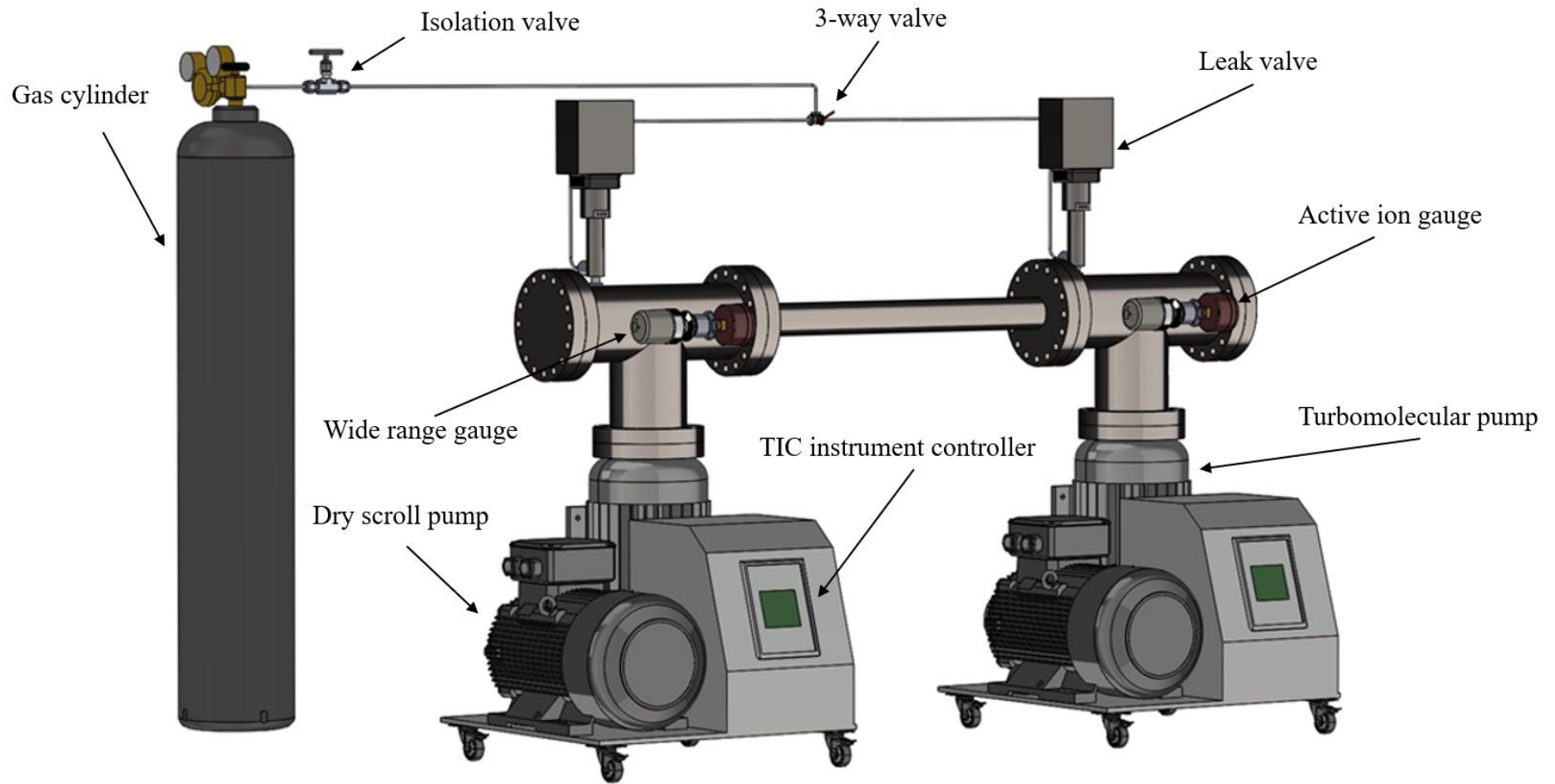
Figure 5.1 Overview of the UHV-DA including gas inlet unit, ultra-high vacuum unit, detection unit and pumping unit

Figure 5.1 shows the main components of the vacuum system, named the ultra-high vacuum diffusion apparatus (UHV-DA). All vacuum components arrived calibrated, surface cleaned, and tested within the specifications. The assembly process was followed by the design principles mentioned in the previous chapters. Beginning with the main body of the apparatus, the specially designed vacuum chambers were connected with turbomolecular pumps through DN100CF flanges with through holes. Sixteen bolts of the flange pair were tightened symmetrically. Subsequently, a spirit level was applied to indicate two chambers in a horizontal line. Next, the diffusion channel was assembled into the chambers on both sides. When the main body of the system was ready, the leak valve and pressure gauges were installed in the chambers corresponding to DN16CF and DN40CF. Finally, the gas inlet pipeline was connected to the vacuum system.

Additionally, the soapy water leak test was applied to avoid large gas leaks or cracks by introducing dry air into the system before starting the pumps [154]. All assembling procedures were conducted with clean powder-free laboratory gloves. The constructed UHV-DA is shown in Figure 5.2, with dimensions of 2 m × 0.75 m × 1.2 m. It was constructed in the Centre for Nature Inspired Engineering, University College London. All vacuum components of the UHV-DA are summarized in Table. 5.1.

Figure 5.2 Ultra-high vacuum diffusion apparatus

Table 5.1 Summary of vacuum components of UHV-DA

Description	Unit	Model	Weight (kg)
Vacuum chamber	2	Custom 304L SS	6.4
Vacuum tube	1	304L SS (DN100CF)	5.3
Turbomolecular pump	2	nEXT300	8.5
Dry scroll pump	2	nXDS6i	26.2
Pumping platform	2	nEXPT	17.8
Leak valve	2	Series 590	2.5
Wide range gauge	2	WRG-S	0.8
Active Ion Gauge	2	AIGX-S	0.5
Residual gas analyzer	1	SRS RGA200	2.7
Tee	1	304L SS (DN40CF)	0.5
Blank flange	1	304L SS (DN100CF)	1.0
Total weight		134.9 kg	
Dimensions		$2 \times 0.75 \times 1.2$ m	

5.2.2 System conductance calculations

The general gas flows, including throughput and effective pumping speed in a vacuum system, are highly affected by the system restriction owing to connecting pipework. Hence, the conductance of the entire system must be estimated before performing any experiments. For the UHV-DA, the main body of the system consisted of two specially designed vacuum chambers connected by a cylindrical tube. To simplify analytical calculation, the system can be simplified to the geometry shown in Figure 5.3.
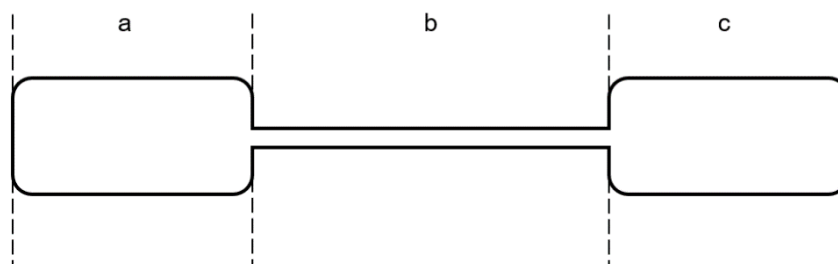
Figure 5.3 Simplified UHV-DA system. Part a and c represent two vacuum chambers with 10 cm diameter; part b represents a cylindrical tube with 2.54 cm diameter

As the simplified system changes in diameter along its length, calculating the conductance of the small diameter parts and large diameter parts as separate sections is

the first procedure. Subsequently, these sections are combined in series by following Equation 5.1.

$$\frac{1}{C_{total}} = \frac{1}{C_a} + \frac{1}{C_b} + \frac{1}{C_c}$$ (5.1)

The conductance calculations for uniform cross-section cylindrical tubes uses Lafferty's table of transmission probabilities for cylindrical tubes [41]. The calculated conductance values for different vacuum sections are shown in Table 5.2.

Table 5.2 Conductance of different vacuum units in UHV-DA, calculated by Equation 2.27.

Unit	Transmission probability	Conductance [L/s]
Part a	0.30	277
Part b	0.06	3.58
Part c	0.30	277

Therefore, the system's total conductance calculated in this manner is

$$C_{total} = \frac{1}{\frac{1}{C_a} + \frac{1}{C_b} + \frac{1}{C_c}} = 3.49 \, L/s$$

5.3 Leak test

5.3.1 Leaking in the high vacuum system

The most crucial requirement for a high vacuum system is the leak-tightness of the system. In vacuum technology, a leak can be represented as a type of hole, which can be in the wall of the vacuum system, at the joints of vacuum components, or even on vacuum instruments [155]. Depending on the leak size, the amount of gas that can leak through could increase the pressure from less than 10^{-12} mbar·L/s up to more than 1 mbar·L/s. As a result, these leaks could completely change the pressure range of the system. Therefore, a leak test is essential for a vacuum system and should be performed before any experiments. Many different leak testing levels can be applied, from experienced observation to a complicated leak detector (mass spectrometer) based on the intended experiments [156, 157].

The UHV-DA was designed to precisely measure Knudsen diffusivity by introducing gases into the system. With a rigorous design, as explained in Chapter 4, our system should not have large leaks, such as gaps between the flange, cracks on the chambers, or welding defects. However, some minor leaks, such as leaks between fittings, are difficult to avoid during the manual assembling process. Consequently, these minor leaks can cause significant deviations in the measurements in the desired pressure range.

5.3.2 Helium leak detection of the UHV-DA

In vacuum technology, soapy water is an easily applied method to locate leaks. However, it is not sufficiently sensitive to check small leaking points and is difficult to use in a high vacuum system. Thus, a helium leak detection instrument is the most convenient method for detecting leaks [158, 159]. The helium leak detector is a stand-alone system that consists of a mass spectrometer, pumping system, and display/control unit, which is simply coupled to the vacuum system with the inlet port (Figure 5.4).
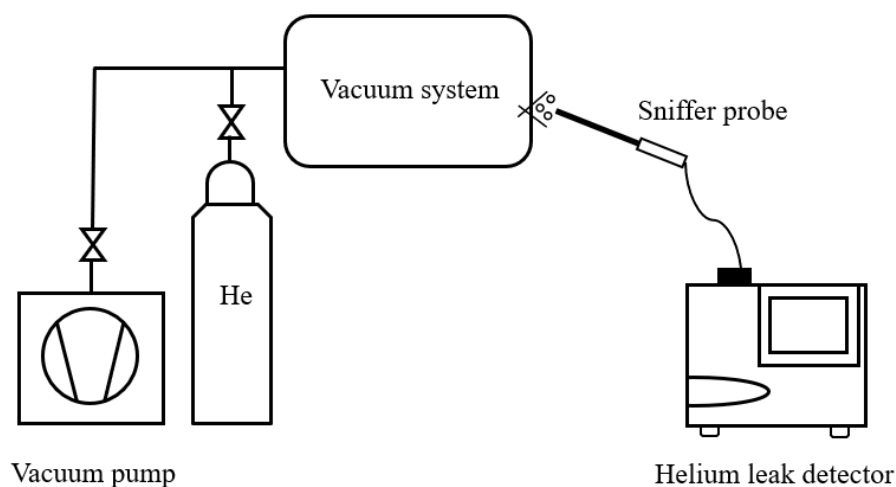
Figure 5.4 Diagram of stand-alone helium leak detector

However, the price of a commercial helium leak detector ranges from £5k to more than £15k, which was far beyond our budget. Thus, we decided to apply helium leak testing based on our current design. The calibrated residual gas analyser, SRS RGA200, a cheap version of mass spectrometer, was used as the helium detector, and it was connected to a vacuum chamber using a straight reducer (DN100CF to DN40CF). Specialty Gases (BUSE Group) 99.999% helium calibration gas was used as the detection gas (Figure 5.5).
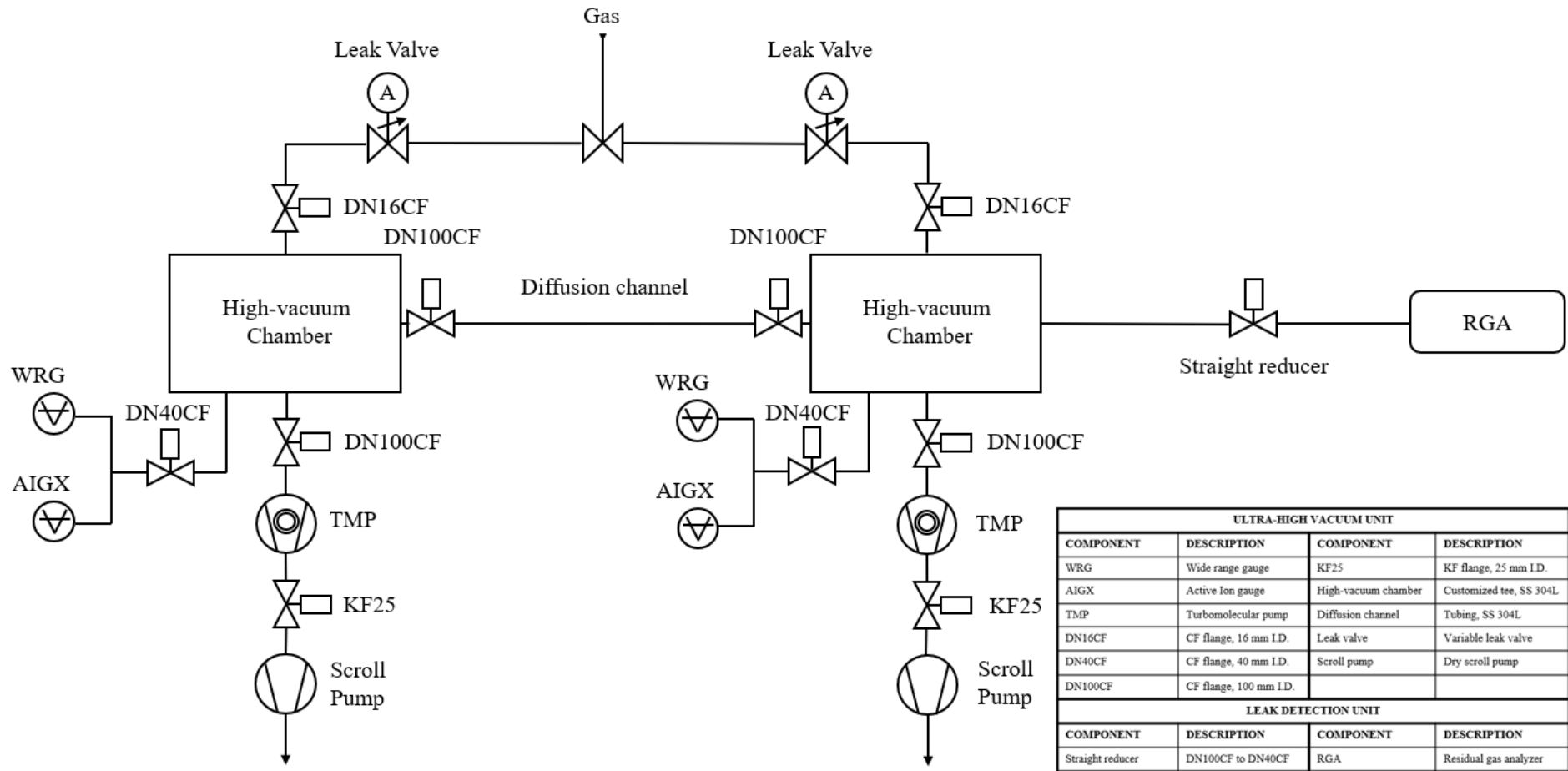
Figure 5.5 Schematic of the UHV-DA with leak detection unit

As the required pressure range was for an ultra-high vacuum, we required spray calibration grade helium to every joint of the apparatus to detect the small leaks. The leaking test procedure is as follows:

1) Assembling the RGA to the vacuum chamber using a straight reducer (DN100CF to DN40CF).

2) Starting the vacuum system first, then switching on the RGA when the system pressure is lower than the maximum operating pressure of the RGA, 10^{-4} mbar.

3) Switching the RGA standard scan model to leak test mode in the RGA Software.

4) Checking the gas flow of the spray helium to avoid flooding the system and destroying the RGA.

5) Spraying 99.999% helium gas to the UHV-DA from the top of the system to the pumping station, particularly focusing on the flanges with copper gaskets, bolt and nut holes, pipe fittings, and valves.

6) Checking the indicator changes in the RGA software and creating the leak detection report.

5.3.3 Results and discussion

To minimise the avoidable minor leaks, leak detection using an RGA was applied to the UHV-DA. The RGA leak test mode indicated the instantaneous partial pressure of helium with an audible beep, which its pitch is proportional to the partial pressure, indicating an abnormal partial pressure [137]. Figure 5.6 shows the result of the leak detection mode with helium on the UHV-DA after 24 h of pumping, where the system pressure was approximately 1×10^{-8} mbar according to the values displayed on the pressure gauges.
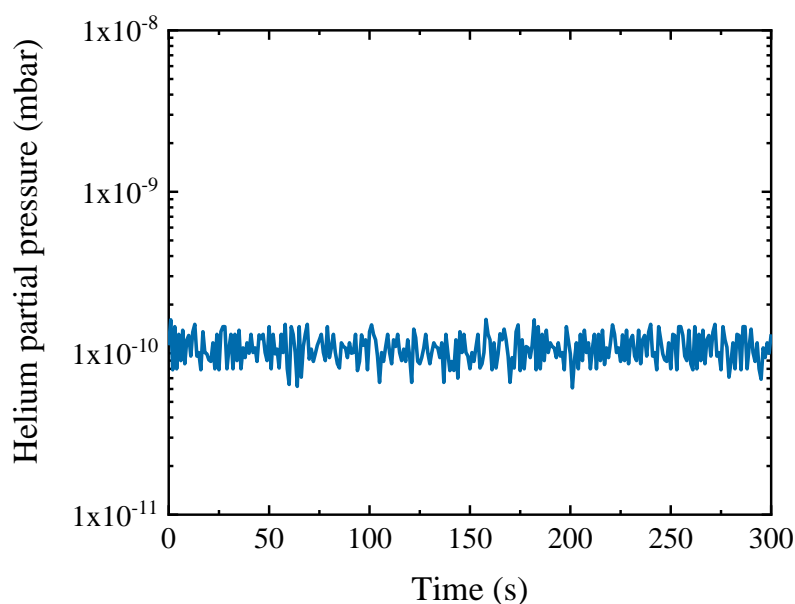
Figure 5.6 Spectrum of the leak detection mode, indicating the partial pressure of helium in the detected system. Detections were conducted under 1.0×10^{-8} mbar total system pressure.

If there is a leak in the vacuum system, a sharp peak should appear in the spectrum [160]. Here, the partial pressure of helium is directly related to the leak rate into the UHV-DA, and the effect of the leak should be studied by calculating the leak throughput. The throughput of the helium is given by Equation 2.2, which is equal to the effective pumping speed at the RGA ioniser multiplied by the partial pressure. If the total throughput of leaks is less than 10% of the total flow rate, the leaks can be ignored [41]. Figure 5.6 shows the partial pressure of helium in the vacuum system. No abnormal partial pressure was observed. The average helium partial pressure was 1.0×10^{-10} mbar, which is relatively small for the Knudsen diffusion measurements.

Although the partial pressure of helium is reasonable for a new vacuum system without baking out, a standard Analog scan mode should also be applied as a complement to the leak test. Analog scan mode is the spectrum analysis mode common to all kinds of RGA, where the X-axis represents the mass range defaulting from 1 to 50 amu and the Y-axis represents the ion current amplitudes. By applying Analog scan mode, all residual gases in UHV-DA can be detected directly. Figure 5.7 shows the scan by performing an Analog scan mode. The spectrum indicated that the peak at 28 was CO, which was associated with CO_2 (44) produced on the filaments of the RGA [160]. Water vapour

was at peak 18. The system pressure was dominated by water vapour, as expected. H_2 was present because of back diffusion through the turbomolecular pump [161]. No oxygen was present in the scan, as expected. Consequently, the UHV-DA was in the proper working order without leaks.
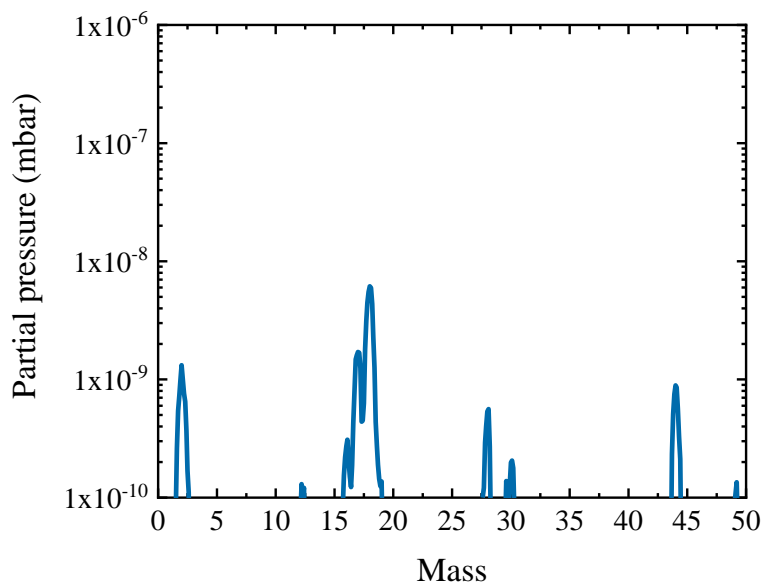
Figure 5.7 Spectrum of the UHV-DA (Analog scan mode)

5.4 Calibration of the vacuum components

Calibration is crucial for an ultra-high vacuum system, which needs to be performed to verify that the vacuum components can provide accurate measurements [70]. For the UHV-DA, two critical vacuum components determined the measurement accuracy: the leak valve and the pressure gauge. The leak valve could precisely control the gas flow into the system, thereby controlling the system pressure. The pressures of the vacuum chambers were measured using pressure gauges, which were directly related to the Knudsen diffusivity. Hence, calibration of these important components before measurements could significantly increase the accuracy of the UHV-DA.

5.4.1 Leak valve

The leak valve applies a PI controller mode to provide precise control in a short time. In the PI mode, two important parameters should be carefully calibrated and set to achieve satisfactory performance. The empirical calibration method is used to set the

parameters P (proportional) and I (integral), and the procedures are shown below.

1) Define the set points (SP1 & SP2)

For a specific working range, pressure setpoints 1 and 2 should be determined first. Setpoint 1 represents the optimised pressure, which is the medium pressure of the working range. Setpoint 2 is approximately 15% lower than setpoint 1. Both pressure setpoints can be optimised later.

2) Optimising parameter P

To optimise parameter P, the gas flow should be constant during the calibration process. P is set to 1 as the starting point, and I is 0. First, the chamber pressure is set to SP2 and it is left until it is stable. Subsequently, the chamber pressure is set to SP1. If a significant pressure overshoot occurs or SP1 cannot be stable after this transition, the parameter P is too large. If no overshoot occurs and the pressure attains SP1 very gradually and asymptotically, the value of P is too small.

3) Optimising parameter I

The gas flow should remain the same in parameter I to optimise the process. P is set to half of the optimised value in step 2 and I is set to 1. First, the chamber pressure SP2 is set. Subsequently, the pressure is set to SP1 when SP2 is stable. If the transition process has a pressure overshoot or the pressure is difficult to stabilise, then parameter I is too large. If the transition indicates a slow asymptotic increase in pressure, parameter I is too small.

To perform the leak valve calibration, we isolated one chamber of the UHV-DA (Figure 5.8). The VAT leak valve uses a $0 - 10$ V output from an Edwards wide range gauge. There is nitrogen at 1-bar gauge pressure connected to the valve inlet and an Edwards turbomolecular pump nEXT300 connected to the vacuum chamber. As the operating range of the UHV-DA was from 1×10^{-8} to 1×10^{-5} mbar, the pressure set points were 5×10^{-6} mbar for SP1 and 4×10^{-6} mbar for SP2. Following the mentioned procedures, the optimised value of parameters I and P were determined, 0.03 and 0.005, respectively.
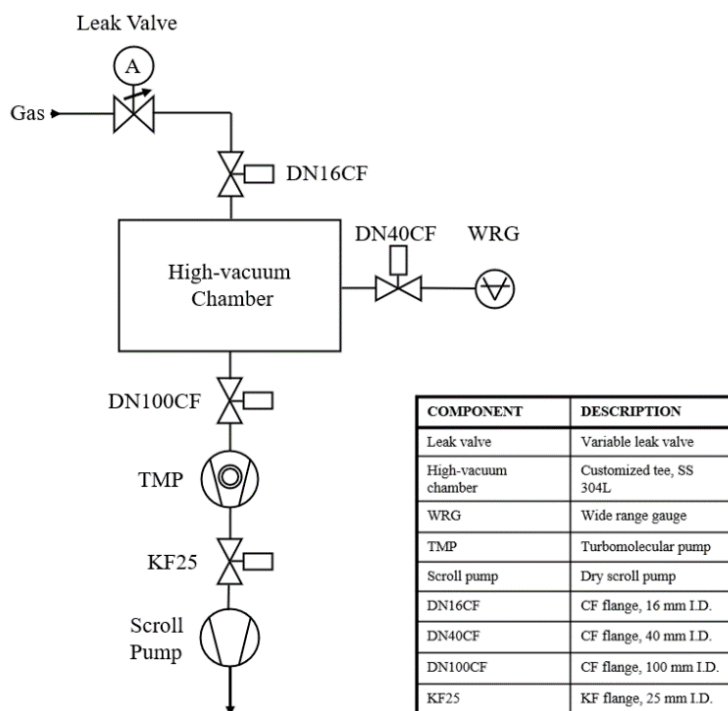
Figure 5.8 Schematic of leak valve calibration system

5.4.2 Pressure gauge

After successfully calibrating the leak valves, the pressure gauges were calibrated next to indicate more accurate readings for the UHV-DA. Precisely calibrating a pressure gauge is difficult and expensive, as it requires a pressure gauge calibrator or a professional calibration service [128, 162]. Our system had two types of pressure gauges, which could be applied to verify the accuracy of the readings. One type of gauge was verified by comparison with another type of gauge, which was called the reference gauge [163]. This calibration process should fulfil the following requirements.

1）The calibration pressures must be established using a stationary continuous flow, which a well-calibrated leak valve can provide.

2）The temperature of the vacuum system should not change during the entire calibration process.

3）The location of the calibrated gauge and reference gauge should be arranged symmetrically to the gas inlet and pump outlet. Additionally, the tubing for both gauges should be the same.

As the accuracy of the AIGX gauge was higher than that of the WRG gauge, the AIGX

gauge was applied as the reference gauge to calibrate the WRG. In the UHV-DA, a WRG gauge and an AIGX gauge were fitted on the vacuum using a three-way DN40 tee. The entire system was wrapped in heating tape, and the temperature was kept constant at 30 °C. The UHV-DA system was operated over a weekend for the system to attain the ultimate pressure. The ultimate pressures of both chambers measured using the AIGX and WRG gauges are shown in Table 5.3. The gauge reading of WRG-1 was close to that of AIGX-1 with only an 18% difference. However, the differences between the WRG-2 and AIGX-2 readings were more than 50%, indicating that WRG-2 could be inaccurate at this pressure range.

Table 5.3 Ultimate pressures of vacuum chambers

	Left chamber		Right chamber
AIGX-1	1.46×10^{-8}	AIGX-2	1.88×10^{-8}
WRG-1	1.2×10^{-8}	WRG-2	9.2×10^{-9}
Difference	18%	Difference	51%

To calibrate the WRGs in all UHV-DA working ranges, we introduced a constant continuous nitrogen flow into the system by controlling the well-calibrated leak valve. To ensure stationary equilibrium, the readings of both gauges were obtained after 5 min. Subsequently, the open rate of the leak valve was increased and a few new readings were obtained per decade. The pressure of the left chamber and the leak valve open rate increased (Figure 5.9). Both gauges indicated almost similar pressure readings from 10^{-6} to 10^{-4} mbar, with differences smaller than 15%.
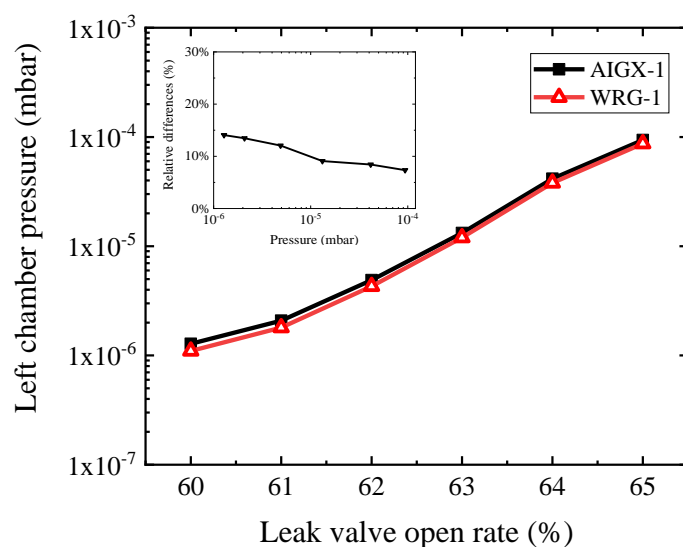
Figure 5.9 Pressure readings of left chamber measured using AIGX-1 and WRG-1

The pressure profiles measured using AIGX-2 and WRG-2 of the right chamber are presented in Figure 5.10, indicating large differences for AIGX-2 and WRG-2 in the range of 10^{-8} to 10^{-6} mbar. Altogether, the relative differences in the left and right gauges decreased with the open rate of the leak valve, shown in the inset of Figure 5.10, which indicated that the pressure range may affect the accuracy of the WRG-2. Therefore, we switched the WRGs to repeat the calibration.
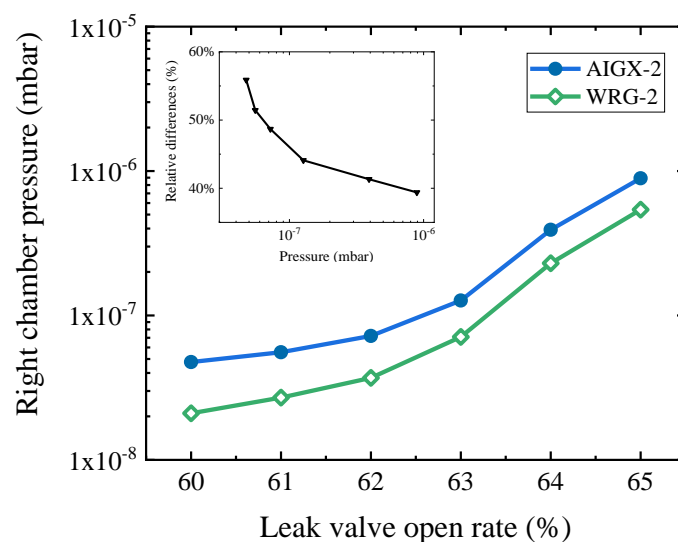
Figure 5.10 Pressure readings of right chamber measured by AIGX-2 and WRG-2

To switch the WRGs, we opened, re-assembled, and evacuated the vacuum system to

10^{-8} mbar before performing calibration. Table 5.4 shows the ultimate pressures of both chambers. The pressure reading of AIGX-1 gauge differed from the reading of WRG-2 with more than 40% deviation. In contrast to the left chamber, the readings of the right chamber were close to each other for AIGX-2 and WRG-1. Therefore, WRG-2 may have not been in good order, which could be caused by a fault to the sensor tube. To further verify this assumption, the same process was repeated by increasing the open rate of the leak valve.

Table 5.4 Ultimate pressures of vacuum chambers (WRGs switched)

	Left chamber		Right chamber
AIGX-1	1.51×10^{-8}	AIGX-2	1.93×10^{-8}
WRG-2	8.5×10^{-9}	WRG-1	1.6×10^{-9}
Difference	44%	Difference	17%

Figure 5.11 shows the readings of the left chamber measured using AIGX-1 and WRG-2. The WRG-2 readings significantly differed from those of the AIGX-1, as expected. The WRG was composed of a Pirani gauge in the low vacuum range ($>10^{-4}$ mbar) and an inverted magnetron gauge for a high vacuum range ($<10^{-4}$ mbar). As WRG-2 could not provide accurate readings for the entire UHV-DA working range, the inverted magnetron part could have been out of order, and the age of the gauge and the dirt in the sensor tubes could be the reason.
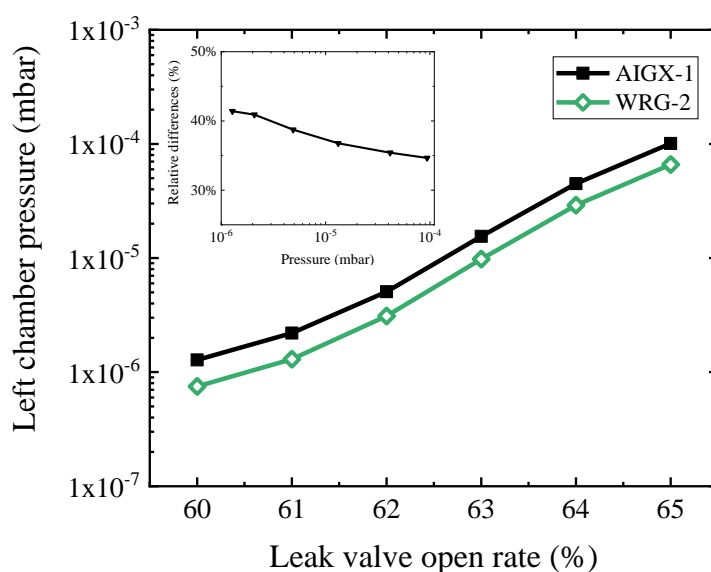
Figure 5.11 Pressure readings of left chamber measured by AIGX-1 and WRG-2

The pressure readings of AIGX-2 and WRG-1 are shown in Figure 5.12. In contrast to the results of Figure 5.11, the two profiles were close to each other with less than 15% differences. The two calibrations verified that the performance of WRG-1 was more accurate than that of WRG-2. Considering the accuracy of the WRG, which was indicated as 30% by the technical data, WRG-1 was in good working order. For the entire calibration process, both AIGX gauges were steady and trustable. Consequently, the readings of the AIGX gauges were applied as the parameters for further Knudsen diffusion calculations.
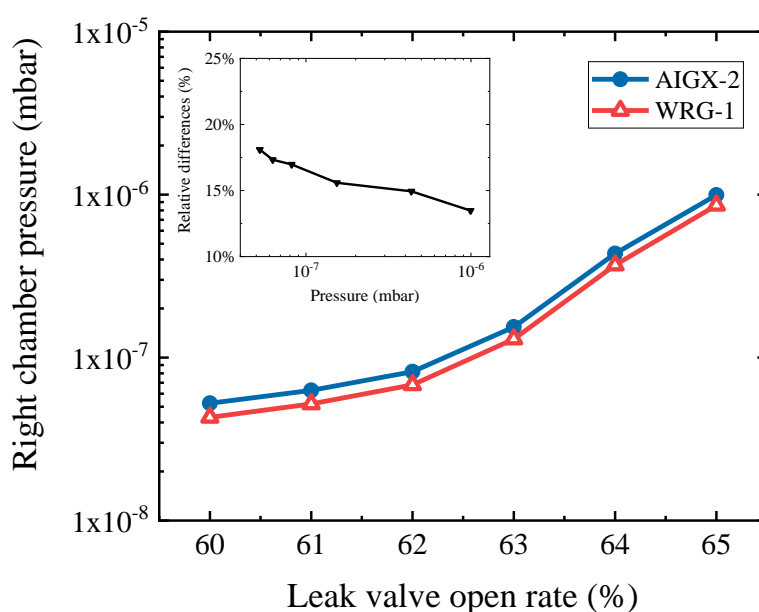
Figure 5.12 Pressure readings of right chamber measured using AIGX-2 and WRG-1

CHAPTER

SIX

6 Knudsen diffusion in tubes of variable geometry

6.1 Introduction

After physically assembling the UHV-DA, experimental validation was necessary to prove that the apparatus could operate in good order and precisely perform Knudsen diffusivity measurements without too many deviations. In this chapter, Knudsen diffusion experiments in a cylindrical tube and theoretical calculations to validate the UHV-DA are described. In addition, the UHV-DA is used to carry out Knudsen diffusion measurements in tubes of arbitrary length, and the results are compared with a COMSOL simulation and Clausing's calculations [164]. Furthermore, an investigation of the pore shape effect on Knudsen diffusion is performed through both UHV-DA experimental measurements and COMSOL simulations. The results are compared to Smoluchowski's conclusion [7], in which he used geometrical arguments to derive a general formula for long tubes with a cross-section of arbitrary shape. The details of the Knudsen diffusion experiments under different conditions are described in this chapter.

6.2 Methodology of the Knudsen diffusion measurements

The UHV-DA provides an ultra-high vacuum environment (lower than 10^{-7} mbar), where the mean free path of a gas molecule is about 10^3 times larger than the tube diameter (2.54 cm). Therefore, the system is fully in the Knudsen regime. The

application of the UHV-DA was to precisely measure the Knudsen diffusivity in a single tube, corresponding geometrically to Knudsen diffusion in a nanoscale pore. Knudsen diffusion involves the net transport of gas molecules in a non-equilibrium situation from one side (e.g. the left chamber) to another (e.g. the right chamber) of the vacuum system through a test tube, resulting from a concentration gradient.

The principle of Knudsen diffusion measurements is based on Fick's first law (Equation 1.6), in which the gas flux that flows to the tube is proportional to the concentration gradient and the Knudsen diffusivity [165]. The ideal gas law can be applied in vacuum technology. Therefore, Fick's first law (Equation 1.6) can be expressed in terms of the pressure gradient and the Knudsen diffusivity:

$$J = -\frac{D}{RT} \cdot \frac{\Delta p}{\Delta x} \tag{6.1}$$

According to the definition of the diffusion flux, J can be expressed in the form:

$$J = \frac{n}{At} \tag{6.2}$$

where A is the cross-sectional area of the tube (in m^2) and t is time (in s). Then, substituting J by Equation 6.2, Equation 6.1 becomes:

$$\frac{1}{RT} \cdot \frac{pV}{t} = -A \cdot \frac{D}{RT} \cdot \frac{\Delta p}{\Delta x} \tag{6.3}$$

In a vacuum system, Q represents the quantity of gas flow rate at a constant temperature, calculated using Equation 2.1 and has the SI units $[Q] = $ Pa m^3/s

According to Equation 2.1 and 6.3, the expression for gas load through the vacuum tube (Q) in the UHV-DA is

$$Q = -A \cdot D \cdot \frac{\Delta p}{\Delta x} \tag{6.4}$$

Consequently, the Knudsen diffusivity D can be calculated using Equation 6.4.

$$D = -\frac{Q}{A} \cdot \frac{\Delta x}{\Delta p} \tag{6.5}$$

Thus, the Knudsen diffusivity can be obtained using the value of the throughput and pressures. According to the mass balance, the gas throughput diffusing in the vacuum tube is equal to the gas load through the turbomolecular pump inlet port, which can be

easily calculated using the effective pumping speed and pressure at the turbomolecular pump inlet port. The effective pumping speed is correlated to the selection of the flange and turbomolecular pump. Additionally, the pressure at the turbomolecular pump inlet port depends on the location and accuracy of the pressure gauges.

As discussed in the previous sections, the UHV-DA was well-designed, as proven by both analytical calculation and numerical simulation. In addition, the crucial vacuum components were meticulously calibrated. Therefore, the UHV-DA could measure the Knudsen diffusivity accurately.

6.3 Experimental

6.3.1 Preceding calculations

To precisely calculate the Knudsen diffusivity according to Equation 6.5, two critical parameters should be determined before the experiments: the effective pumping speed and gas load through the tube. Both parameters were derived from a mass balance over the system. A schematic of the gas loads in the vacuum system is shown in Figure 6.1.
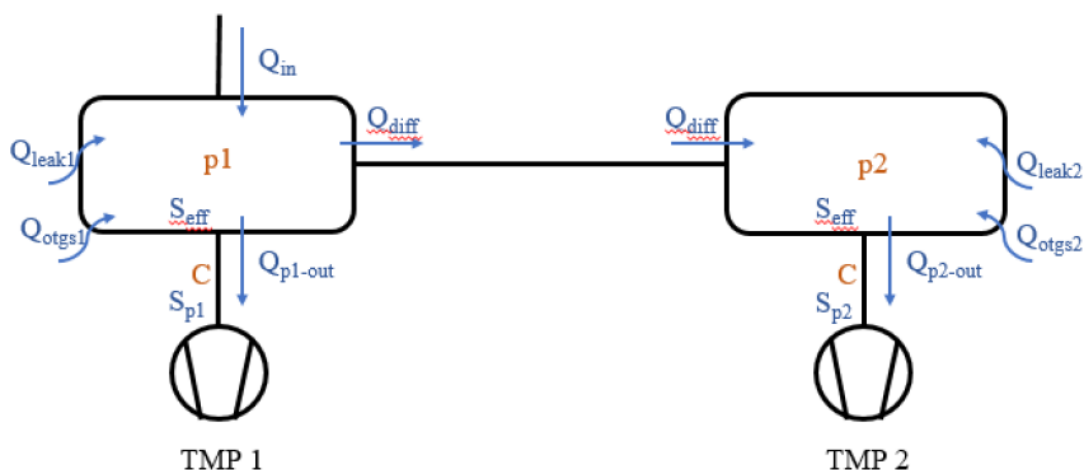
Figure 6.1 Schematic of the gas loads in the vacuum system

Assuming that the pressures and temperatures are constant for both chambers, the mass balance over vacuum chamber 1 can be expressed as

$$Q_{in} + Q_{leak1} + Q_{otgs1} - (Q_{p1-out} + Q_{diff}) = Q_{ac} \tag{6.6}$$

The mass balance over vacuum chamber 2 is

$$Q_{diff} + Q_{leak2} + Q_{otgs2} - Q_{p2-out} = Q_{ac} \tag{6.7}$$

where Q_{in} is the process gas load, Q_{leak} is the leakage of the system, Q_{otgs} is the outgassing of the system, Q_{diff} is the gas load through the tube, and Q_{ac} is the accumulated gas load.

As the UHV-DA passed the leaking test, the value of Q_{leak} was very small. In addition, the material of the UHV-DA was stainless steel with an extremely low outgassing rate; thus, Q_{otgs} was a small number. Compared with the process gas load (Q_{in}), both Q_{leak} and Q_{otgs} can be neglected. Thus, the equilibrium mass balance for the two chambers can be simplified to

Chamber 1:

$$Q_{in} - (Q_{p1-out} + Q_{diff}) = 0 \tag{6.8}$$

Chamber 2:

$$Q_{diff} - Q_{p2-out} = 0 \tag{6.9}$$

The gas output of chamber 2 (Q_{p2-out}) can be defined by

$$Q_{p2-out} = p_2 \cdot S_{eff} \tag{6.10}$$

The pressure gauge in chamber 2 can measure p_2, and S_{eff} which is the result of the conductance of the connection between the turbomolecular pump and the centre of chamber 2, can be calculated using Equation 2.9:

$$\frac{1}{S_{eff}} = \frac{1}{S_{manu}} + \frac{1}{C} \tag{2.9}$$

To calculate the effective pumping speed, the pumping speed provided by manufacturer and the conductance of the connection to chamber 2 should be obtained first. For nEXT300 turbomolecular pump, the pumping speed provided by the manufacturer was 300 L/s. The connection to chamber 2 was designed as a short tube with a DN100CF flange (10cm diameter), where the ratio of diameter to length is approximately 1. The transmission probability (f) can be attained using Figure 2.6 derived by Cole in 1977 (Table A.1, Appendix A), which is 0.5142. And $C_{aperture}$ is 924 L/s calculated by Equation 2.21. Therefore, the conductance of the connection, 475 L/s, can be easily

calculated by using Equation 2.26. Moreover, the effective pumping speed can be obtained as 184 L/s by applying Equation 2.9.

6.3.2 Experimental procedures

As explained in the methodology section, the Knudsen diffusivity measurement was performed in such a way that a known concentration gradient was created and the gas flow through the pore could be calculated using Equation 6.4 as the governing equation. Zero grade nitrogen was selected as the experimental gas to avoid interference from impurities. Figure 6.2 shows a schematic of the Knudsen diffusion measurement system.
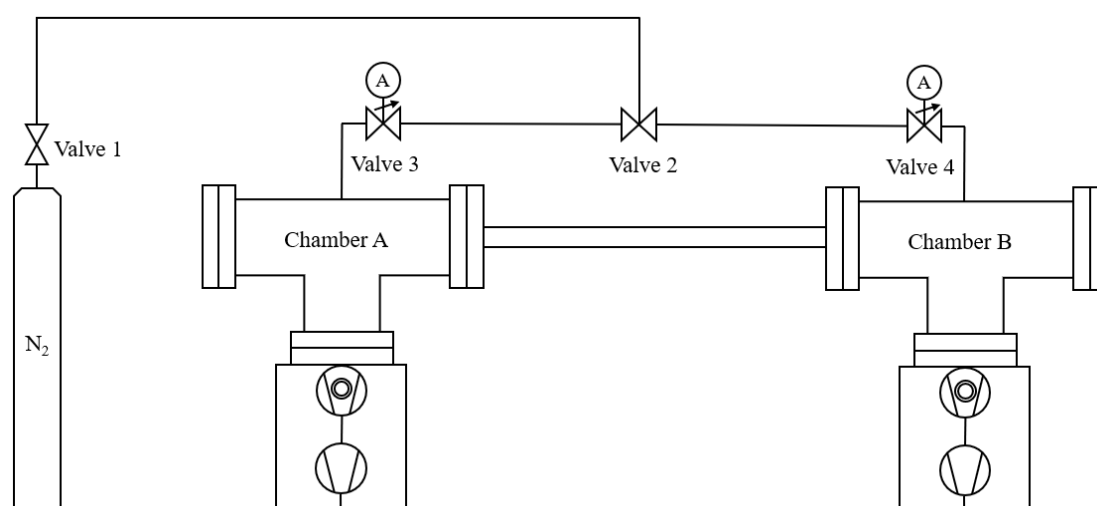
Figure 6.2 Schematic of the apparatus for Knudsen diffusion measurements. Isolating valve (valve 1), three-way valve (valve 2), and leak valves (valve 3 and 4)

The experimental procedure was as follows:

1) Chambers A and B were evacuated to 10^{-8} mbar using the high-vacuum pump sets.
2) Valve 2 was opened to chamber A, and valve 1 was opened.
3) The program-controlled valve 3 was opened, then the pressure of chamber A was set to introduce continuous gas leaking into chamber A.
4) As the pressure of both chambers increased, a concentration gradient was created and measured by pressure gauges.
5) When the pressures in chambers A and B were stable, the vacuum system attained equilibrium. The pressures of both chambers were recorded using a TIC panel.

6.4 Knudsen diffusion coefficient measurement in the UHV-DA

To measure the Knudsen diffusion coefficient in the UHV-DA, measurements were performed in a 0.5-m, uniform cross-section cylindrical tube. As explained in Section 6.2, Equation 6.5 can be used to obtain Knudsen diffusion coefficients by directly measuring the pressures of both chambers (the gradient in pressure), along with the calculated flux. The diffusion 'channel' was a circular cross-section cylindrical tube with a length-to-diameter ratio of 20. The well-known Knudsen diffusivity formula (Equation 1.8) indicates that the Knudsen diffusivity is only proportional to the gas mean velocity and pore diameter. Therefore, we expect the diffusion coefficients to be identical in the Knudsen regime pressure range (up to 10^{-4} mbar).

The UHV-DA obtains the diffusion coefficient from a pressure gradient. The obtained Knudsen diffusion coefficients as a function of the pressure gradient is shown in Figure 6.3, and each experimental point was repeated four times to minimise experimental error. The error bars are smaller than the size of the symbol for most pressure gradients.
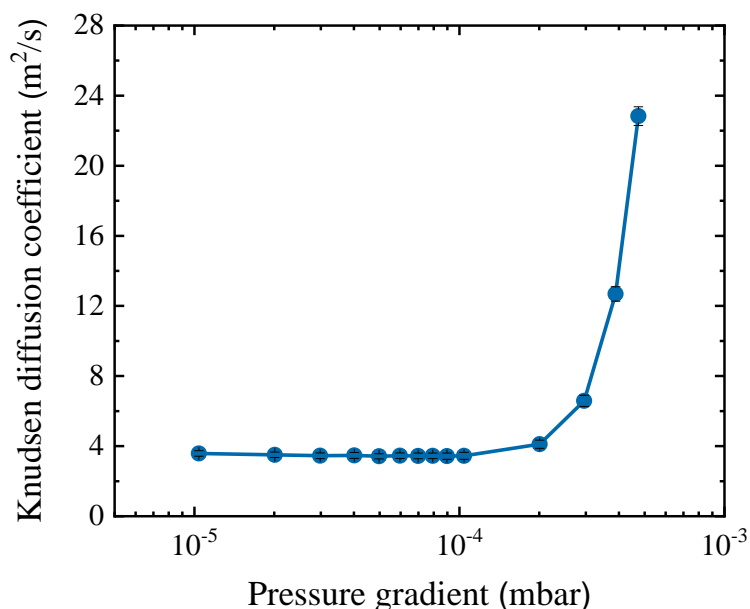
Figure 6.3 Correlation between Knudsen diffusion coefficient and pressure gradient

The experimental results indicated that the Knudsen diffusion coefficients increased as the pressure gradient increased, which was unexpected. As the pressure gradient was

predominantly determined by the pressure of the gas inlet chamber, the Knudsen diffusion coefficients depended on the chamber with a higher pressure. The profile of the diffusion coefficient consisted of two domains: a pressure gradient higher than 1×10^{-4} mbar and lower than 1×10^{-4} mbar. According to Equation 1.2, the mean free path of nitrogen should be larger than the dimensions of the tube when the pressure is lower than 4×10^{-3} mbar, where Knudsen diffusion occurs. However, considering complexity of the vacuum system, the actual maximum pressure must be lower than 4×10^{-3} mbar. As shown in Figure 6.3, the experimental results indicate that the limited upper pressure is around 1×10^{-4} mbar. The Knudsen diffusion coefficients measured at the lower pressure limit were identical with an experimental error of less than 10%. In contrast, the diffusion coefficients increased exponentially as the pressure increased above 10^{-4} mbar, where the flow regime could change.

To reproduce the results for Knudsen diffusion coefficients, we performed Knudsen diffusion measurements in the opposite diffusion direction. The results presented in Figure 6.4 are representative of two series of measurements with opposite diffusion directions. A similar trend in the Knudsen diffusion coefficient profile was observed. However, the deviation in the diffusion coefficients between the two profiles amounted to more than 40% in the higher-pressure range. The reason could be that the Knudsen diffusion coefficient cannot be calculated using the derived formula Equation 6.5 because of the changes in the flow regime in this pressure range. The results at the lower pressure range were highly consistent and repeatable over two series of experiments with a small deviation owing to operational errors during the measurements.
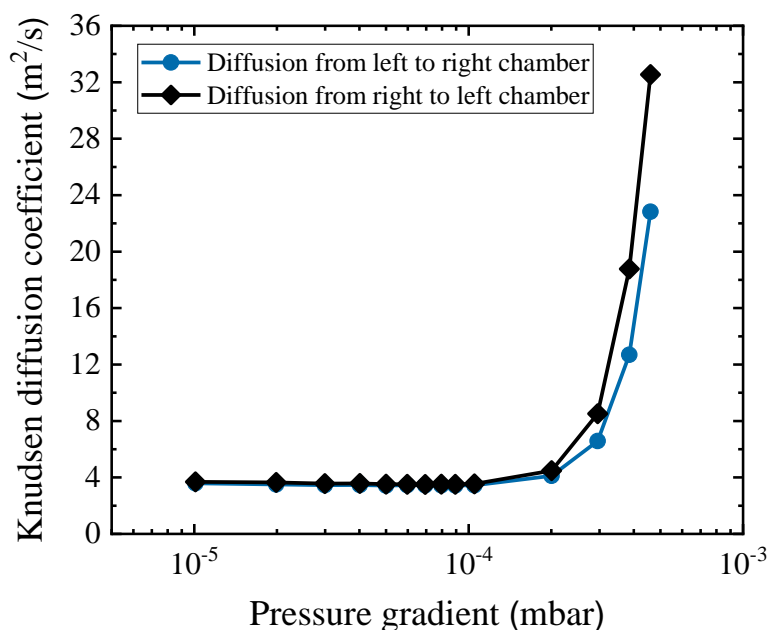
Figure 6.4 Knudsen diffusion measurements with different diffusion direction

We made a general estimation of the UHV-DA measurement accuracy by comparing it to Knudsen's theoretical calculations [6]. The Knudsen diffusion coefficient for our UHV-DA cylindrical tube could be easily estimated using Equation 1.8 with a result of 3.64 m^2/s. Figure 6.5 compares the Knudsen diffusivities measured *via* the UHV-DA measurements with theoretical calculations.

As explained in Section 1.2.2 of this work, Knudsen diffusion does not incorporate a pressure dependence, where the dashed line indicates the constant theoretical calculated diffusion coefficient. The deviation between the experimental and theoretically calculated Knudsen diffusivity is less than 10%, indicating that the UHV-DA is in good working order. However, it is also apparent that the experimental results of the Knudsen diffusion coefficients are slightly smaller than theoretical calculations. Knudsen's formula only predicts the Knudsen diffusivities for very long, smooth cylindrical pores. The 0.5-meter stainless steel tube for the UHV-DA is not long enough for Knudsen's theory to hold exactly, and the surface cannot be perfectly smooth. Therefore, the experimental results could be smaller than Knudsen's theoretical limit.
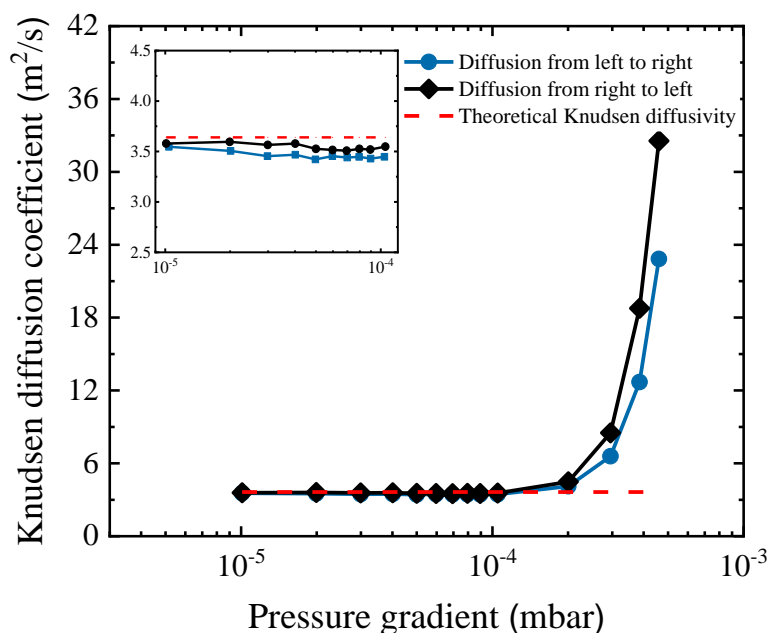
Figure 6.5 Comparison between the UHV-DA measurements and theoretical calculation (inset shows a magnification for low pressure gradients)

6.5 Investigation of tube length on Knudsen diffusion

Over the past decades, gas flow through tubes of finite length has been extensively studied through both computer simulation using the Monte Carlo method and experimentally in capillaries [166-168]. However, measuring the Knudsen diffusion coefficient on a macroscopic scale to emulate processes that occur in nanoporous media is still virgin teritory. Moreover, the investigation of tube length on Knudsen diffusion can validate the accuracy of the UHV-DA by comparing it with the analytical calculation. Therefore, investigating the tube length during Knudsen diffusion in the UHV-DA is essential. This section describes the measurement of the Knudsen diffusion coefficient in tubes of varying lengths using the UHV-DA. Subsequently, numerical simulation to investigate the effect of tube length on Knudsen diffusion are carried out using COMSOL Multiphysics. Finally, the experimental and numerical results are compared with the analytical calculations.

6.5.1 Experimental measurements using the UHV-DA

The UHV-DA was validated using a Knudsen diffusion experiment of a 500-mm long,

circular cross-section tube. The experimental results indicated that the UHV-DA was in a good working order as expected. To investigate the effect of tube length on Knudsen diffusion, another cylindrical SS tube was applied as a comparison to the 500-mm tube. A 250-mm long cylindrical tube was selected as an experimental pore with a ratio of the length to the diameter of approximately 10. Both tubes were manufactured by Edwards. All vacuum welds passed the leakage check with a helium mass spectrometer before being assembled into the UHV-DA.

According to the results of section 6.4, the pressure range of $1 \times 10^{-5} - 1 \times 10^{-4}$ mbar provides the most reliable results, for which the Knudsen diffusion coefficients are consistent and there are no diffusion regime changes. Therefore, we focused on the experimental range between 1×10^{-5} and 1×10^{-4} mbar. The obtained Knudsen diffusion coefficients for the 250-mm tube were compared with those of the 500-mm tube (Figure 6.6).
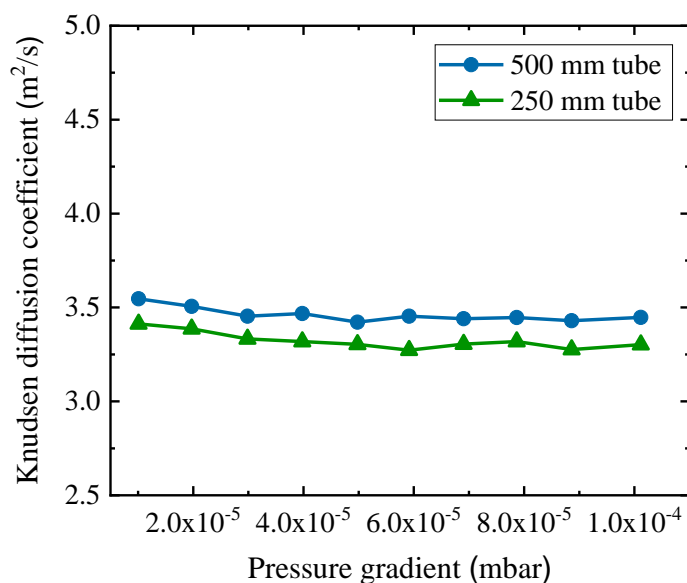
Figure 6.6 Knudsen diffusion coefficients in 500-mm and 250-mm tubes

Figure 6.6 shows that the Knudsen diffusion coefficient is roughly independent of the pressure, as expected. The value of the Knudsen diffusion coefficients in the 250-mm tube was smaller than the diffusion coefficients in the 500 mm tube with 4% deviations between the two. As listed in the Table 3.4, however, $\pm 15\%$ accuracy of pressure gauges and operational errors could result in discrepancies in experimental measurements, shown in Figure 6.7 as a coloured band. Generally, the diffusion

coefficient for a shorter tube is expected to be higher; the experimental results suggest the opposite, but the deviations are smaller than the accuracy of the gauges. Therefore, more numerical predictions and analytical calculations were applied to compare to the experimental results.
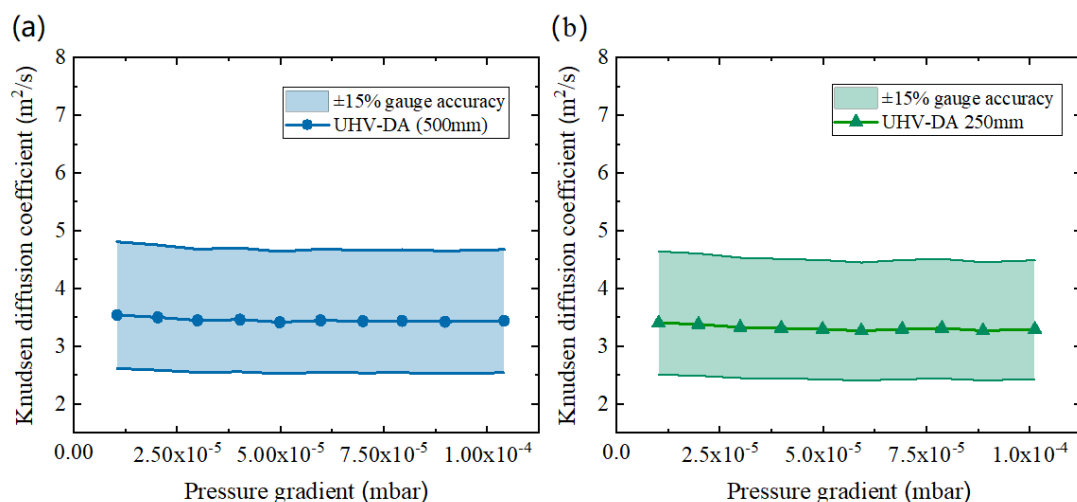
Figure 6.7 Knudsen diffusion coefficients zone in 500-mm and 250-mm tubes; the bands indicate 15% uncertainty, due to the accuracy of the gauges

6.5.2 COMSOL simulation

To further investigate the Knudsen diffusion in pores of varying lengths, COMSOL was applied to simulate diffusion of gas molecules [169]. The Molecular Flow Module is a unique module of the COMSOL Multiphysics software, which is designed to accurately simulate flows in the Knudsen regime [170, 171]. The Molecular Flow Module uses the angular coefficient method to simulate steady-state flows in Knudsen regime, and it is only applied for Knudsen numbers greater than 10 [172]. The module enables the molecular flux, number density, and pressure to be computed on the surfaces of the system. The calculation principle is to integrate all the arriving fluxes at a surface from all other surfaces in its line-of-sight.

Using the Molecular Flow Module, the pressure distribution and flux profile can be simulated in the UHV-DA system, in which the Knudsen diffusion coefficient can be calculated according to the simulation data. Moreover, the COMSOL Molecular Flow Module can be used to numerically predict systems with a complex geometry.
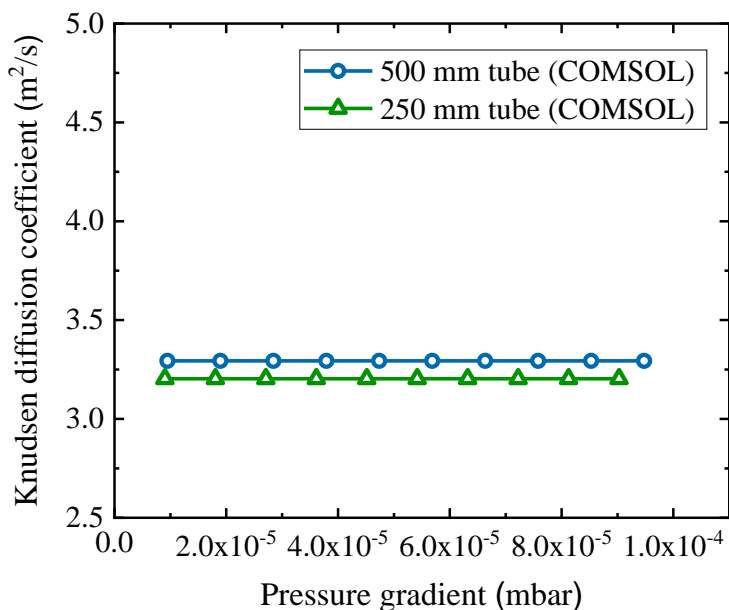
Figure 6.8 COMSOL predictions of Knudsen diffusion coefficients for 250-mm and 500-mm long tubes

Figure 6.8 shows the simulated Knudsen diffusion coefficients for tubes of varying lengths. Both series of simulated results were independent of the pressure gradient, as expected. Moreover, a similar trend of diffusion coefficients in tubes of varying lengths as the experimental measurements indicated that longer tubes have larger Knudsen diffusion coefficients.

6.5.3 Discussion

According to the pioneering results of Clausing and Cole [8, 40], the Knudsen diffusion coefficient can be expressed as a function of the transmission probability. Therefore, we can analytically compute the Knudsen diffusion coefficient for a tube of arbitrary length. The correlation between the Knudsen diffusion coefficient and transmission probability is shown as follows:

$$D_k = f \cdot \frac{L}{4} \cdot \sqrt{\frac{8RT}{\pi M}} \tag{6.11}$$

where f is the transmission probability for the cylindrical tube, which can be obtained by Cole's calculations (Table A.1). The calculated results from the Knudsen diffusion coefficients are shown in Table 6.1. The analytical calculations indicate that the shorter

tube did not result in a larger Knudsen diffusion coefficient compared with the longer tube, and it is determined by the transmission probability and tube length.

Table 6.1 Analytical calculation of transmission probabilities and Knudsen diffusion coefficients

	Transmission probability	Analytical D_K using Equation 6.11 (m^2/s)
250 mm tube	0.098	2.89
500 mm tube	0.053	3.12

To compare the Knudsen diffusion coefficients using different approaches, a comparison between UHV-DA experimental results, COMSOL simulation results, and analytical calculations of Knudsen diffusion coefficients in varying tubes is shown in Figure 6.9.
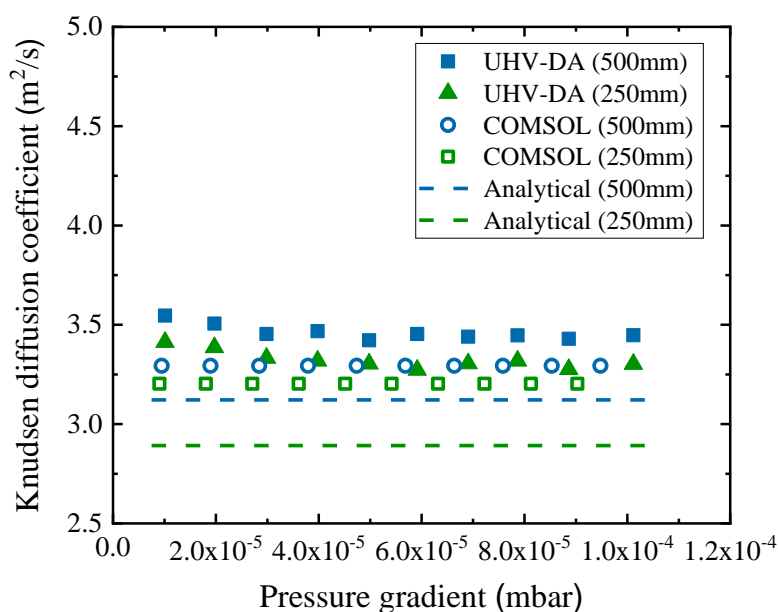
Figure 6.9 Comparison between the experimental and simulated routes to obtain Knudsen diffusion coefficients

Figure 6.9 shows that the experimental values of the diffusion coefficient in both tubes were larger than the analytical calculations. According to Equation 6.5, the experimental results were determined by the system output and chamber pressure measured using gauges. The system output is correlated to the pumping speed and

pressure at the system output port. Generally, the pressure at the system output port is slightly smaller than in the chamber, where it is measured by gauges. Consequently, the calculated gas output is greater than the actual output, and the Knudsen diffusion coefficient is higher than the analytical value. Avoiding this error is difficult, unless additional gauges are included at the system output port. Although there is an approximately 10% systematic error in the UHV-DA measurements, the experimental results are quite consistent and reproducible. Moreover, similar trends of varying tube lengths were observed, as expected. Therefore, the measurement of the Knudsen diffusion coefficient using the UHV-DA was reliable and could be improved with a few modifications.

The COMSOL simulation results seemed more consistent than the experimental results (Figure 6.9). Comparing the simulation results and analytical values, the COMSOL Molecular Flow Module was relatively reliable with only a 5.5% deviation for the 500 mm tube and a 10.8% deviation for the 250 mm tube. The Molecular Flow Module applied the boundary condition of a large 'reservoir' for the incoming molecular flux, for which nitrogen was present at a specified pressure in the reservoir. As the mean free path of nitrogen is much larger than the size of the opening to the reservoir (diameter of the tube), the nitrogen molecules travelling to the tube followed the principle of molecular effusion. Consequently, the pressure at the tube opening differed from the value of the pressure for the reservoir, resulting in higher apparent Knudsen diffusion coefficients. This can be explained by "entrance effect" [4], which affects the diffusion coefficient, depending on which pressure difference is used to calculate the diffusivity. Both measurements using the UHV-DA and simulations using COMSOL indicated that the shorter lengths provide a slightly lower Knudsen diffusion coefficient for cylindrical tubes with a uniform cross-section.

6.6   Investigation of the pore shape effect on Knudsen diffusion

Knudsen diffusion in complex pores is crucial in the fields of rarefied gas dynamics and heterogeneous catalysis, which are commonly studied through molecular simulation and analytical calculations [173, 174]. The problem of the geometrical effect on Knudsen diffusion has been investigated for more than a century [175]. Knudsen first

proposed a relationship for diffusion of a rarefied gas through a long cylindrical tube with arbitrary cross section in 1909 [176]. However, the results derived by Knudsen were proven erroneous by Smoluchowski, who proposed a corrected analytical expression [7]. However, no direct experiments have proven these results in a single pore on a macroscopic scale. The UHV-DA was used to measure Knudsen diffusion in different geometrical tubes. Knudsen diffusion in both a tube with a square cross-section and a circular cross-section tube was investigated, and the results were compared with COMSOL simulations and Smoluchowski's formula to further validate the accuracy of the UHV-DA.

6.6.1 Experimental measurements using the UHV-DA

To investigate the effect of tube shape on Knudsen diffusion, a 500-mm long stainless steel tube with a 23-mm square cross-section was manufactured and installed on the UHV-DA. As with other SS tubes provided by Edwards, all vacuum welds were vacuum tight with leakage checking. Images of a tube with a circular cross-section and a square cross-section are shown in Figure 6.10.

Figure 6.10 Images of stainless steel tubes with varying cross-sectional shapes

To make the results more consistent, the experimental pressure range was still from 1×10^{-5} to 1×10^{-4} mbar. The effect of tube geometry on Knudsen diffusion was measured in the UHV-DA for circular and square tubes with a length of 500-mm. Figure 6.11 shows the Knudsen diffusion coefficients in the two tubes. The diffusion coefficients for a tube with circular cross-section are very close to those for a tube with a square

cross-section. Both series should be essentially parallel, however, the variations were not stochastic, which going up and down in the same way. The main reason could be the pressure gradients measured by pressure gauges leading to systematic errors.
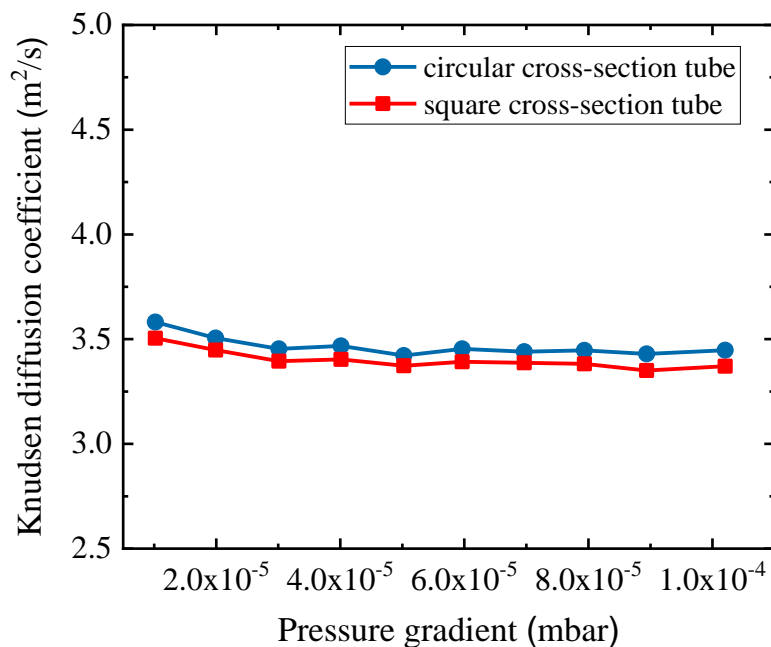
Figure 6.11 Measured Knudsen diffusion coefficients in tubes with a circular and square cross-section

6.6.2 COMSOL simulation

The COMSOL Molecular Flow Module was used to investigate the effect of pore shape on Knudsen diffusion (Figure 6.12). Nitrogen gas flows through two tubes with different pore shapes from a reservoir with higher pressure to a reservoir with lower pressure. According to the simulation results, the predicted Knudsen diffusion coefficients for circular and square cross-section tubes were close to each other with less than 1% deviation.
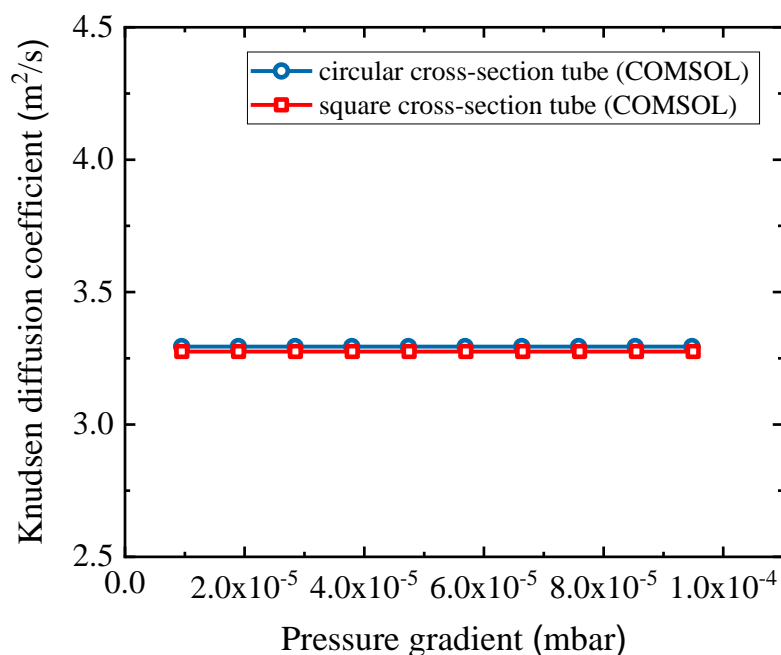
Figure 6.12 COMSOL predictions of Knudsen diffusion coefficients in square and circular cross-section tubes

6.6.3 Comparison

In the last pages of Knudsen's first paper on rarefied gases flow through a long cylindrical tube, he mentioned that the derived formula can be applied to arbitrary cross-section tubes [6]. A year later, Smoluchowski proved that Knudsen's formula for arbitrary cross-sections could not be correct when the cross-section was very rough with a significantly high perimeter-to-area ratio [7]. He also illustrated that the pore (tube) shape has a limited effect on Knudsen diffusion. To prove the accuracy of the UHV-DA and COMSOL simulation, the ratios of the diffusion coefficient between the square and circular cross-section tubes from both experimental measurements and COMSOL simulation were compared to Smoluchowski's calculation shown in Figure 6.13.
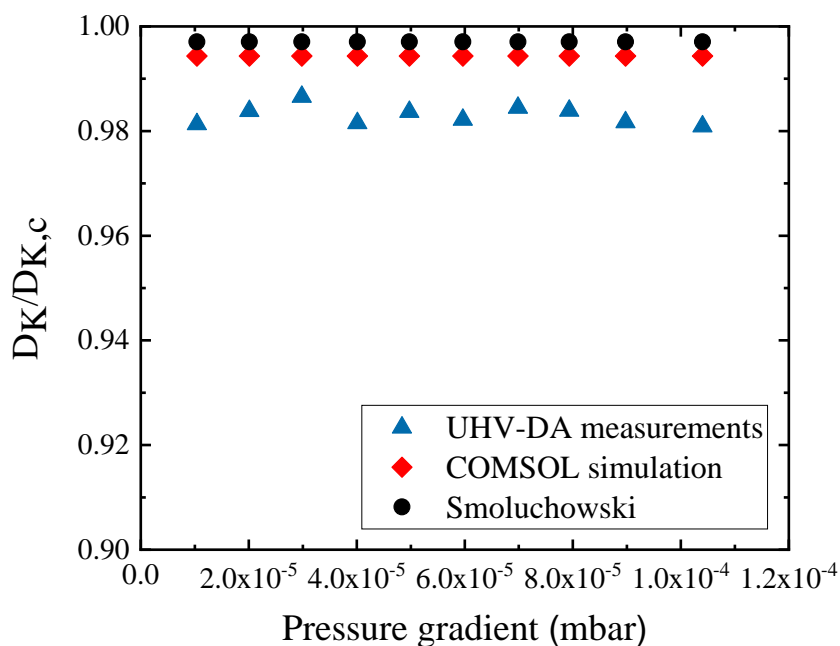
Figure 6.13 Ratio of the Knudsen diffusion coefficients for a square tube (D_K) to that for a circular tube of equal cross-sectional area ($D_{K,c}$) at different pressures using different approaches.

Both the UHV-DA experimental approach and COMSOL method indicated that the square cross-section has a limited effect on the Knudsen diffusion coefficient. The experimental diffusion coefficient ratios for the square tube ($D_K/D_{k,c}$) were close to Smoluchowski's calculations with less than 2% deviation. Furthermore, the COMSOL predicted ratios indicated a good agreement between the computer-simulated and Smoluchowski-calculated Knudsen diffusion coefficients. According to the previously discussed results, the UHV-DA was in good working order and could be used to qualitatively measure the Knudsen diffusion coefficient in tubes with varying surface roughness. The COMSOL Molecular Flow Module can be applied simultaneously as a complementary method to investigate the effect of surface roughness on Knudsen diffusion.

CHAPTER

SEVEN

7 Knudsen diffusion in tubes with a fractal surface

7.1 Introduction

As explained in Chapter 1, the ultimate aim of this project was to investigate the effect of surface roughness on Knudsen diffusion using the UHV-DA. The heart of this part is the physical, fractal pore model. In this chapter, 3D printing technology will be described, including technique selection, model design, manufacturing, and vacuum compatibility tests. Although further experimental investigations of Knudsen diffusion in rough fractal pores using UHV-DA were difficult to complete because of the effect of the Covid-19 pandemic, computer predictions using COMSOL's Molecular Flow Module are presented in this chapter.

7.2 Additive manufacturing

7.2.1 Overview

The heart for investigating the effect of surface roughness on Knudsen diffusion is the physical 'pore' model. Producing the fractal pore model with conventional milling is impossible. A possible method is the use of the 3D printing technique [177-179]. 3D printing, also called additive manufacturing, is the construction of a 3D object from a computer-aided design model [180]. This technique can produce almost any desired shape, and it enables the development of pore models with different surface features or 'roughness' [181]. As the most crucial part of the surface roughness investigation,

creating a desired physical fractal model is difficult. All these aspects, manufacturing techniques, materials, economic aspects, vacuum compatibility, and model robustness should be considered first before fabricating an actual fractal model.

7.2.2 3D printing techniques

In current 3D printing markets, the most commonly used printing techniques are direct metal laser sintering (DMLS), stereolithography (SLA), and selective laser sintering (SLS) [177, 182, 183].

DMLS, as the first 3D technique to directly create a metal part without tooling, was developed by EOS GmbH and Rapid Product Innovations in 1994 [184]. Today, this technique has been widely used to fabricate aerospace parts, dental components, and surgical implants. DMLS utilizes a variety of metal and alloy materials such as titanium, cobalt, and stainless steel, to create strong metal parts [185]. During the production procedure, support structures are added to provide supplemental strength to fine features. However, owing to the geometrical complexity of the pores, some parts may collapse when removing the supports. In addition, DMLS materials are frequently expensive. Creating a 0.5-m long cylindrical tube with 2.5 cm diameter using the DMLS technique can cost £10k.

SLA, known as the first 3D printing technology, is another commonly used technique to create small concept models and complex parts [186]. This technique, as an industrial 3D printing process, can be applied using various materials with high resolution. Compared with DMLS, stereolithographic 3D printing has many advantages, such as high accuracy, faster, cheaper, and no risk for the pore structure to collapse [187]. However, supports leave behind small spikes; thus, this technology is difficult to apply to our fractal model, and the commonly used acrylic-based resin can result in structural brittleness [188].

As the first technology of laser sintering 3D printing methods, SLS is a rapid prototyping technology that converts 3D CAD data into physical parts in a few hours. It was first developed and patented by Deckard in 1989 [189]. Unlike DMLS, SLS frequently utilizes powdered nylon and polyether ketone materials. The parts fabricated using SLS frequently have fine details, good surface finish, and chemical resistance [190-192]. When a 3D part is built using SLS, it is always encompassed by a large

amount of unsintered powder that can provide supplemental strength and eliminate the necessity for support structures [193]. A complex design such as our fractal pore tube, even for a high-roughness tube, can be produced using SLS within a few hours. Moreover, the price is much cheaper than the DMLS technique. Based on these advantages, the SLS technique was selected as the production technique to create tubes with a fractal surface.

7.2.3 CAD software

Any 3D printing part begins from a 3D model generated using CAD software. There are many 3D modelling software packages on the market, such as SketchUp, AutoCAD, Rhinoceros 3D, and SOLIDWORKS [194]. All these CAD software packages can create 3D models using .stl files for 3D printing. In this project, SOLIDWORKS was used to create 3D models for the Knudsen diffusion study. As a professional CAD program, SOLIDWORKS is widely used for industrial objects as it enables the creation of very detailed features. Unlike other CAD software, it is easy to learn and use for non-CAD background users. Moreover, SOLIDWORKS can be used together with COMSOL Multiphysics simulation to understand how 3D parts perform in a 'real' environment. Therefore, SOLIDWORKS cannot only create CAD models for 3D printing, but also be easily synchronized to COMSOL for further vacuum system simulation with a LiveLink add-on [195].

7.3 Experimental

7.3.1 Fractal model design

To investigate the effect of surface roughness on Knudsen diffusion, a fractal surface was first generated. A self-similar Koch surface was applied as fractal surface. The fractal structure began from one square tile. Subsequently, it expanded by generating a smaller square tile on each surface of the original tile. The direction of the new generated tile was random to create a random fractal pore. Figure 7.1 shows the 2D and 3D schematics of the Koch fractal surface.

2D Koch fractal surface
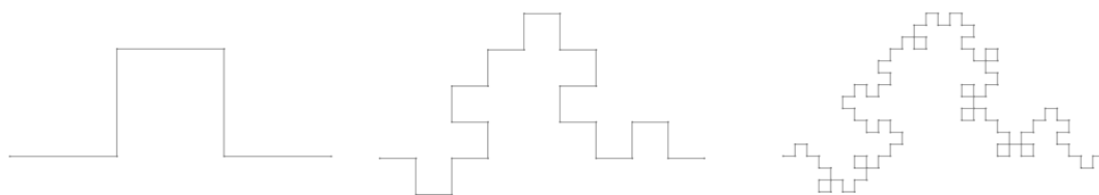
3D Koch fractal surface
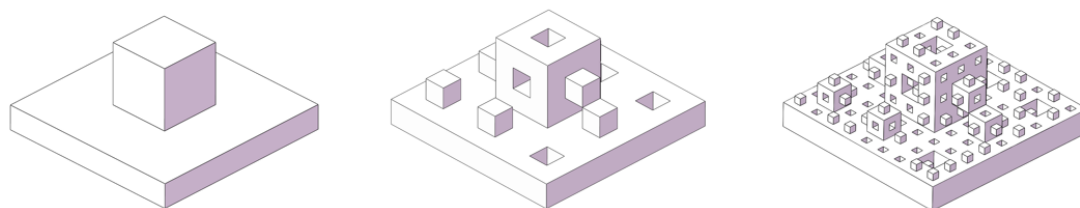
Figure 7.1 Schematic of the 2D and 3D Koch fractal surface

The surface roughness (ξ) of the Koch surface pore at any generation is calculated using the ratio of the surface area (side length for 2D) of the fractal pore to the surface area (side length) of a non-fractal pore with the same cross-sectional area. Therefore, the roughness for the 3D fractal pore is $\left(\frac{13}{9}\right)^N$, where N is the order of the generation. A conceptual 3D Koch surface tube for $N = 2$ is shown in Figure 7.2.
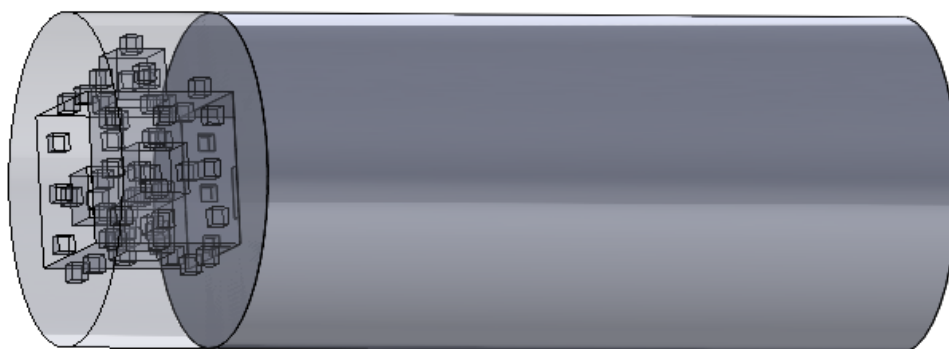
Figure 7.2 Schematic of a 3D Koch surface tube generated using SOLIDWORKS

7.3.2 Manufacturing of 3D-printed fractal tubes

The fractal roughness prototypes up to 3 generations were designed using SOLIDWORKS (Dassault Systèmes, France). The fractal designs were rendered to

an .stl file before performing the 3D print-out. The 3D printer was an EOS Formiga P100, which is a type of SLS printer using PA2200 nylon as the material [196]. The suggested build size is 240 mm × 190 mm × 320 mm at £0.07/cm^3, and the build rate can be up to 20 mm height/h [197].

7.3.2.1 3D-printed segments

Directly printing complex fractal surface tubes with a length of 500 mm are impractical because removing residual powdered nylon for a long tube is extremely difficult. Alternatively, the fractal surface tubes were segmented, and the length of one segment was no more than 50 mm. Subsequently, the segments were glued together with a low-viscosity glue to create a fractal surface tube. Figure 7.3 shows the 3D-printed prototypes with different values of N.
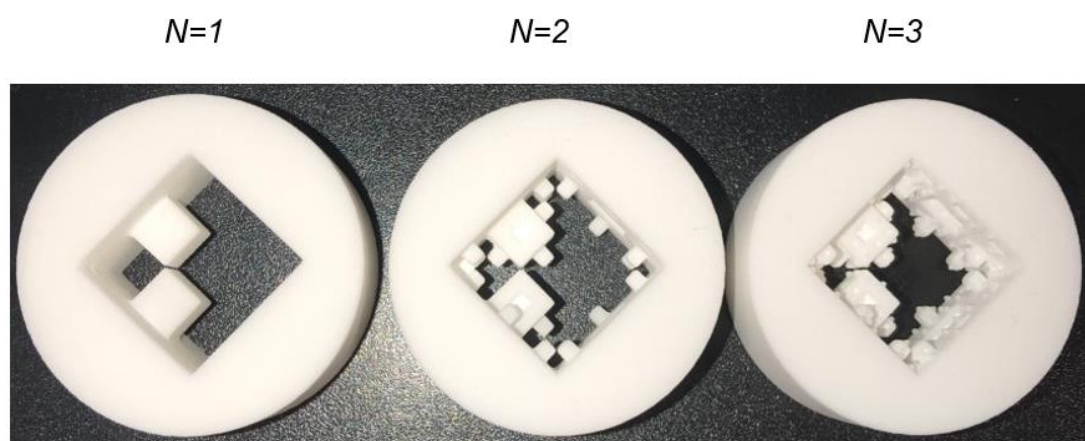
Figure 7.3 Image of 3D-printed prototypes with $N = 1$, 2, and 3

Resolution is the key factor for a fractal pore model and is determined by the 3D printer [198]. The suggested minimum build size of the EOS Formiga P100 is 0.4 mm and the listed layer thickness is 0.1 mm (Appendix Table B.1). Thus, the smallest size of the square tile for the third generation fractal segment should be no smaller than 0.4 mm. Thus, the characteristic length of the square cross-section was chosen to be 10.8 mm (calculated by $3^N \times 0.4$ mm, where $N = 3$). As the square tiles are generated in random directions, the outer diameter of the fractal surface pore must be at least twice the size of the cross-sectional square, i.e. at least 21.6 mm. Table 7.1 shows the dimensions of four fractal surface prototypes ($N = 3$) with different resolutions from 0.4 to 0.7 mm.

Table 7.1 Dimensions of fractal surface prototypes with different sizes of the smallest scale structure

Prototype	Smallest square tile (mm)	Largest square tile (mm)	Cross-sectional square (mm)	Segment outer diameter (mm)
1	0.4×0.4	3.6×3.6	10.8×10.8	21.6
2	0.5×0.5	4.5×4.5	13.5×13.5	27.0
3	0.6×0.6	5.4×5.4	16.2×16.2	32.4
4	0.7×0.7	6.3×6.3	18.9×18.9	37.8

Table 7.1 shows that only Prototype 1 can fit in the current SS tube with a diameter of 22.1 mm. All other resolution fractal surface prototypes require a larger diameter tube to fit in. However, considering the tolerance of the 3D-printed parts, a lower resolution should be used. Prototypes 2, 3, and 4 were produced *via* the EOS Formiga P100. Only the smallest scale structures of prototype 4 were consistent and tough without any damage during the cleaning process. Therefore, the dimensions of prototype 4 were applied for the segment design, and the length of the segment was 18.9 mm. A new SS tube with larger diameter is essential for the experiments.

7.3.2.2 Vacuum glue

To achieve successful bonding between 3D-printed segments, adhesives should be selected properly. Epoxy adhesives are the most widely used adhesives for coating, sealing, and structural bonding owing to their high strength and resistance at room temperature [199]. Epoxy adhesives can adhere to a wide variety of ceramics, stainless steel, plastics, rubbers, and most other commonly used materials [200, 201]. As the 3D-printed segments would be placed in vacuum, an ultra-high vacuum compatible epoxy adhesive is required.

Araldite® 2020 (XW 396/XW 397) was selected as the ultra-high-vacuum-compatible adhesive. Araldite is a two-component, low-viscosity, water-white epoxy resin system with a high performance in sealing, bonding, coating, and encapsulating [202]. Araldite® 2020 is prepared by mixing two proprietary solutions in a 20:7 ratio by volume; this process should be done slowly to avoid trapping air [203]. The pot life of a mixed 100-gram batch is approximately 40-50 minutes. It performs well in a vacuum system and can cure readily at room temperature for 24 h, and more rapidly at elevated temperatures (only 2.5 h at 60–100 °C). It also has excellent chemical resistance to

water, oils, and hydraulic fluids.

The durability of a bonded joint is highly dependent on the proper treatment of the bonding surfaces [204]. All the surfaces should be carefully cleaned with a good degreasing agent such as isopropanol to remove all traces of oil, dirt, and grease. Additionally, a radial glue cavity should be designed at the join intersection, where Araldite 2020 is sucked into the cavity through an access port to fill the join region. This special design can guarantee a seal in a vacuum environment (Figure 7.4).
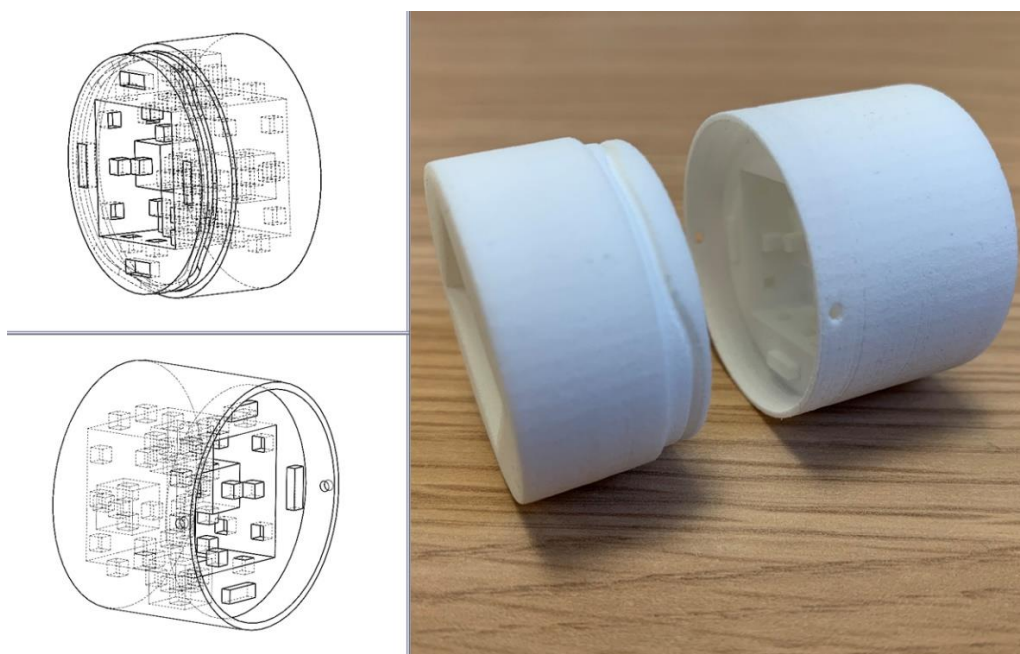
Figure 7.4 Image of the segments with glue cavity

7.3.2.3 Fractal surface tube in SS tube

A 3D printing technique was used to print the fractal surface segments, which would eventually be inserted into the SS tube for diffusion measurement. However, directly placing a 3D-printed fractal surface tube inside the SS tube without any connecting part can result in large leaks between the flange of the SS tube and fractal surface tube. A 3D-printed cover with thread features was designed to connect the main body of the fractal surface tube and seal both ends of the tube (Figure 7.5). This design could effectively avoid gas molecules diffusing into the small voids between the 3D-printed tube and SS tube, and also maintain the vacuum-tightness of the fractal tube.
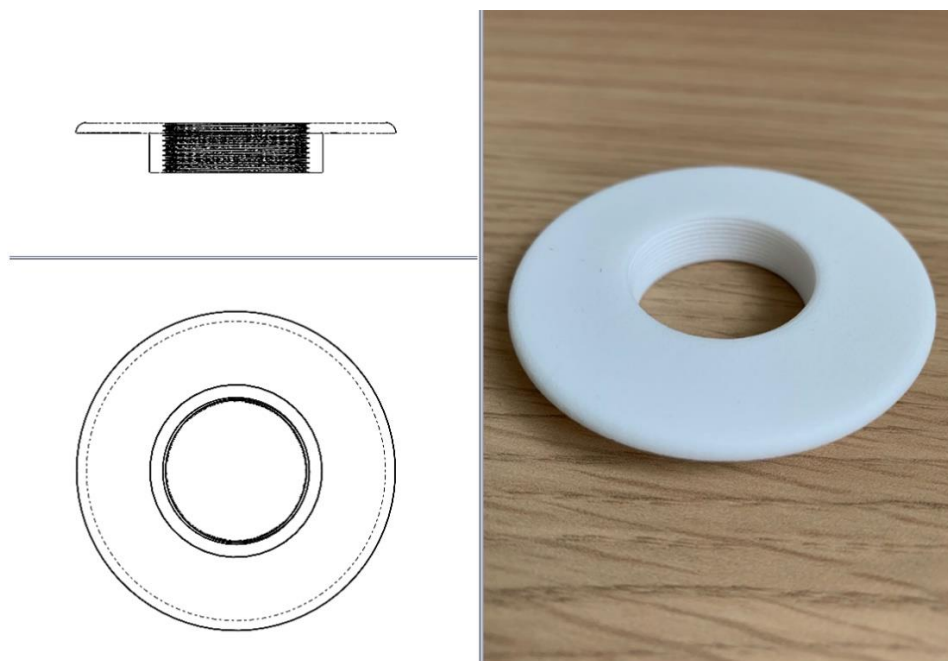
Figure 7.5 Image of the 3D-printed cover

The integrated 3D-printed tube consisted of a certain number of fractal surface segments and two specially designed covers. Araldite 2020 was applied to glue the segments together as the main body of the fractal surface tube. Two covers were designed and connected to the fractal surface tube's main body using thread features.
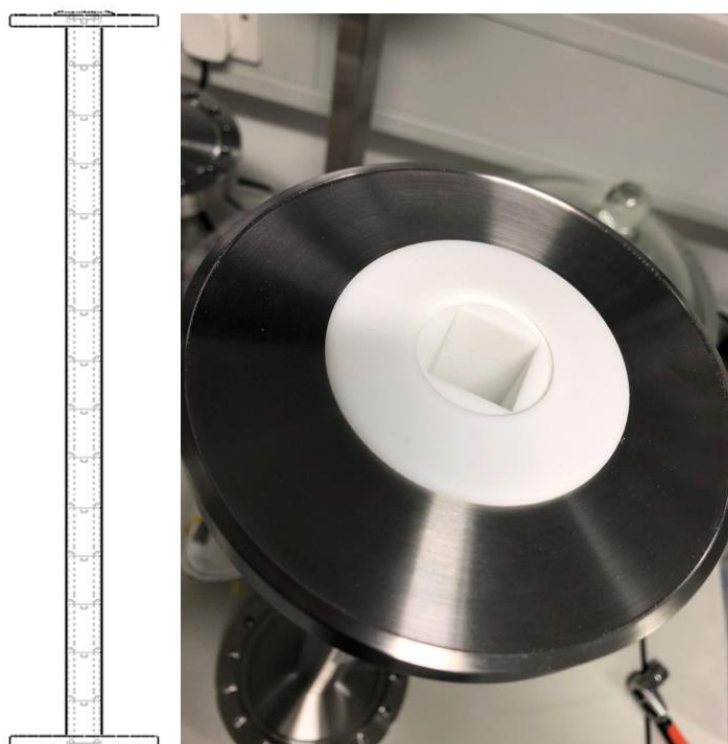
Figure 7.6 Image of a 3D-printed tube inside the SS tube

7.3.3 Vacuum compatibility of the 3D-printed tube

As 3D printing is additive, some small voids may be present in the 3D-printed part [205]. These small voids can trap gases, resulting in a high outgassing rate. Plastic materials frequently contain a large amount of water [206]. When the plastic is inside a vacuum system, diffusion will cause water molecules to gradually leave the plastic, which is expected to play a dominant role in the system below 10^{-4} mbar. In addition, a thick layer of water molecules can build up on the surface of the 3D-printed part under atmospheric conditions. As a consequence, a very long time would be required for the vacuum system to attain the ultimate pressure. Therefore, some printed materials may not be suitable for ultra-high vacuum environments, and verifying the vacuum properties of a 3D-printed fractal surface segment is crucial before Knudsen diffusion measurements.
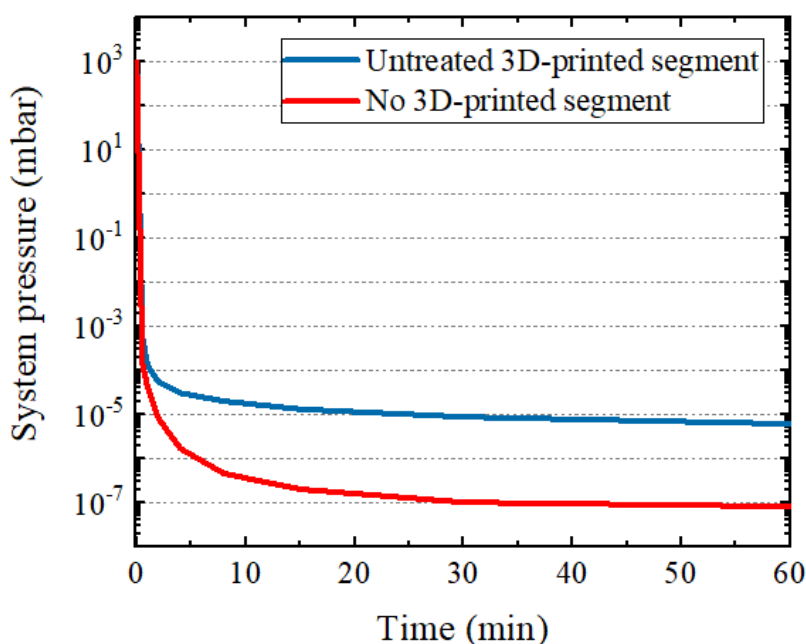
Figure 7.7 Time-dependent pressure of the UHV-DA with and without a 3D-printed segment

The fractal surface segment with $N = 1$ shown in Figure 7.3 was placed inside the UHV-DA without any pre-treatment (for instance, 60 °C for a day can improve the vacuum properties). Figure 7.7 shows the pressure drop over a 60-min period in the UHV-DA with and without a fractal surface segment. UHV-DA required less than 30 min to attain 10^{-5} mbar from atmospheric pressure for both scenarios, which indicated

that the system was considered sufficiently leak-tight. However, attaining pressures lower than 10^{-5} mbar was very difficult and required a significantly longer time. This indicated that residual gases and water molecules are expected to be present in large quantities, and the water adsorbed on the outside of the segment is a significant problem. Thus, proper pre-treatment is necessary to eliminate undesired gases. The pre-treatment procedure was modified from the CERN cleaning guideline shown below [207]:

a) Use an air blow gun to remove the excess PA2020 nylon powder.

b) Ultrasonically clean the parts in deionised water, followed by rinsing with deionised water.

c) Ultrasonically clean using ethanol heated at 40 °C to dissolve excess organics.

d) Evaporate excess ethanol by spraying with dry nitrogen.

e) Insert into a vacuum chamber and pump down to 10^{-8} mbar.

f) Bake chamber for 24 h at 65 °C.
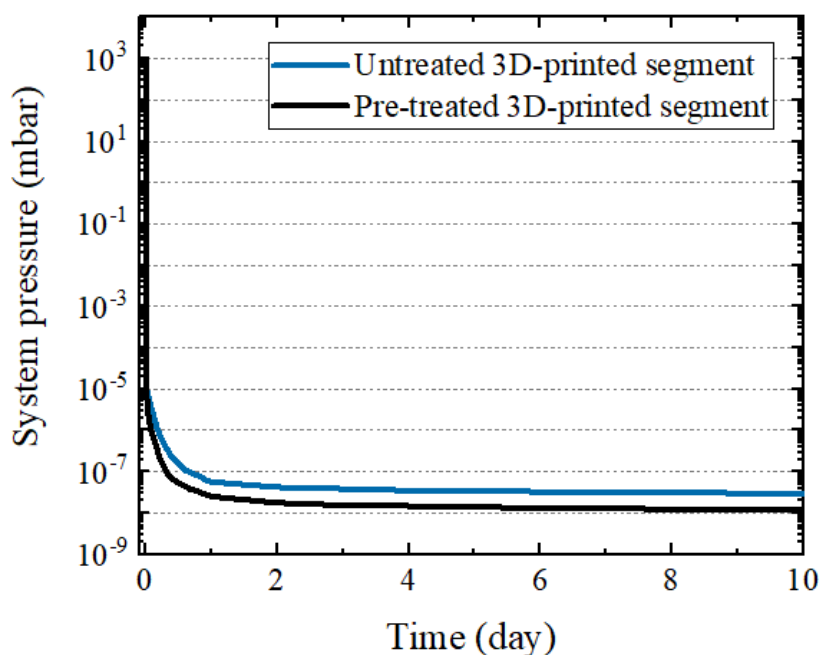
Figure 7.8 Time-dependent pressure of UHV-DA with a pre-treated 3D-printed segment

Figure 7.8 shows the pump-down curves for both a pre-treated segment and an untreated 3D-printed segment. The pump-down time performances of the pre-treated and untreated segments differed significantly. The time for a fractal surface segment without pre-treatment to attain the ultimate pressure, 1×10^{-8} mbar, is excessively long.

Next, the vacuum compatibility of 3D-printed segments with different materials was investigated. An SRS RGA200 mass spectrometer was used to measure the outgassing behaviour of a PA2020 nylon segment using SLS, as mentioned in section 7.3.2. An acrylic-based resin segment using SLA (Form labs – Form 3) was also tested for comparison. The residual gas analysis is shown in Figure 7.9.
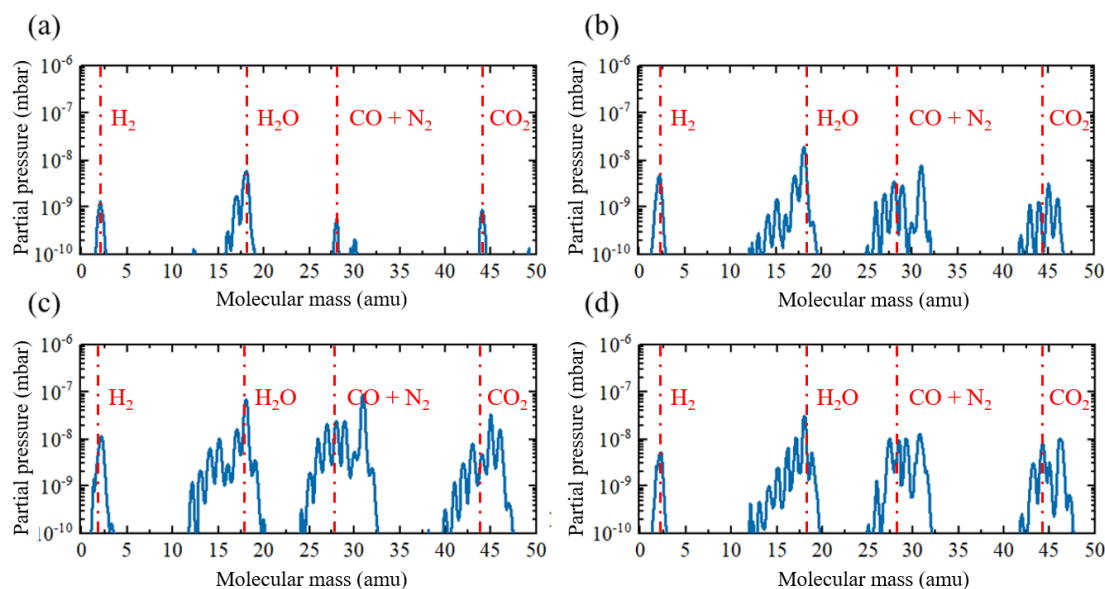
Figure 7.9 Residual gas analysis of materials in UHV-DA 24 h: (a) Empty system; (b) a pre-treated PA2200 nylon segment; (c) a pre-treated acrylic-based resin segment; (d) an untreated PA2200 nylon segment

The residual gas measurements indicated that more N_2, H_2, and CO_2 were trapped in the acrylic-based resin 3D-printed segment (Figure 7.9c). In contrast to acrylic-based resin, the PA2200 nylon segment seemed to have adsorbed less water from the cleaning process, and fewer gases vented into the vacuum system. In addition, the PA2200 nylon segment without bake-out is shown in Figure 7.9d, where the bake-out was essential for a 3D-printed nylon segment even at a low baking temperature (60 °C). Of these tested materials, PA2200 nylon with pre-treated process was found to be high-vacuum compatible.
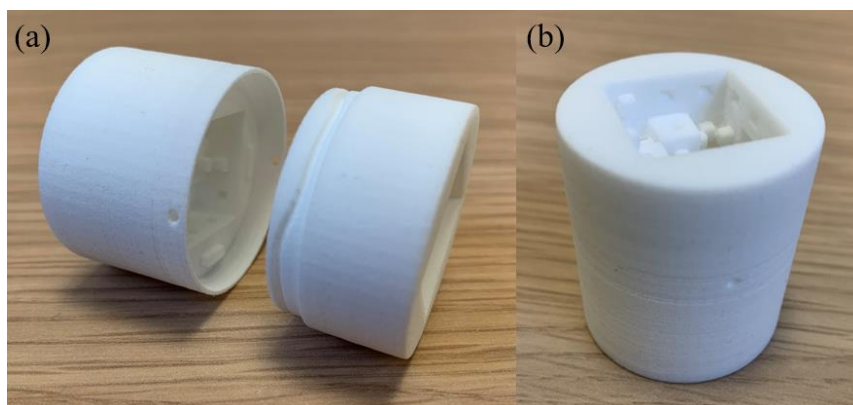
Figure 7.10 Image of fractal surface segments: (a) two individual segments; (b) two segments glued by Araldite 2020.

As an entire 3D-printed fractal tube consists of several fractal surface segments, the epoxy glue Araldite 2020 needed to be applied to glue the segments together. Therefore, the vacuum compatibility of two 3D-printed segments with epoxy glue (Araldite 2020) should be tested as well. Figure 7.10 shows the images of two fractal surface segments ($N = 2$) glued by Araldite 2020, as well as the individual fractal surface segments. The spectra are compared in Figure 7.11. The spectra showed no significant differences between two segments with Araldite 2020 and without Araldite 2020 after 24 hours, indicating the great vacuum performance of Araldite 2020. Therefore, fractal surface segments of PA2200 with Araldite 2020 as the glue could be used to investigate the effects of fractal surface roughness on Knudsen diffusion in the UHV-DA.
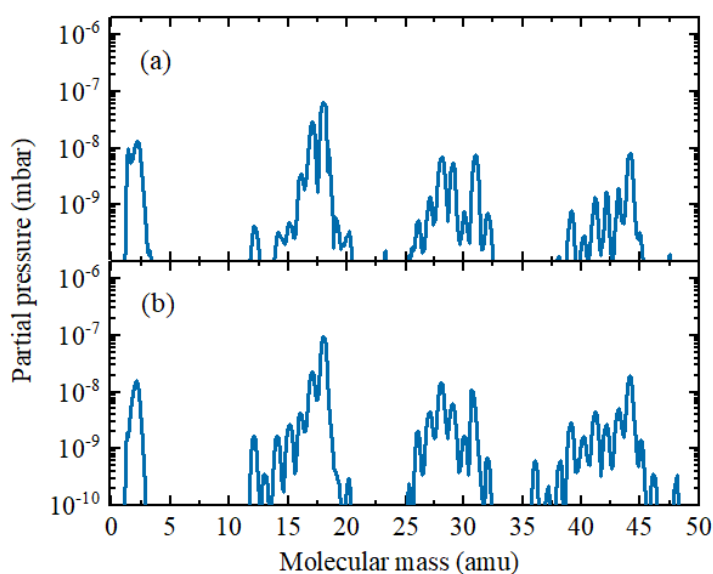
Figure 7.11 Residual gas analysis: (a) two individual pre-treated segments; (b) two pre-treated segments glued by Araldite 2020.

7.4 Investigation of the surface roughness effect on Knudsen diffusion

The investigation of Knudsen diffusion in smooth tubes with different pore shapes and length has been presented in Chapter 6. In reality, pores are often not smooth [208]. Therefore, it is essential to analytically study the surface irregularity in porous media. By using fractal geometry, irregular surface features or 'roughness' could be altered systematically and is expected to affect Knudsen diffusion in the UHV-DA. In this chapter, tubes with a fractal surface were designed to investigate the effect of surface roughness on Knudsen diffusion. Owing to the effect of the Covid-19 pandemic, Knudsen diffusion measurements using the UHV-DA were not completed. Instead, a numerical approach was applied to investigate the effect of surface roughness on Knudsen diffusion, which is described in detail below. Some suggestions on experimental measurements in UHV-DA are also discussed.

7.4.1 Numerical prediction

In this study, the Knudsen diffusion in porous materials was modelled using tubes of various lengths and shapes, and the process was investigated using the COMSOL molecular flow module discussed in the previous chapter. The simulation results revealed that the deviation between the theoretical and computational results of the Knudsen diffusivity was relatively small. Therefore, the effect of the fractal surface roughness on the Knudsen diffusivity was investigated using the COMSOL molecular flow module.

7.4.1.1 Development of the COMSOL model

As the fractal surface models were complex with several small features, the direct development of the structures using COMSOL was impractical. Therefore, first, CAD models of the fractal surface pores were created using SOLIDWORKS, after which they were synchronised to COMSOL using a LiveLink add-on. Figure 7.12 shows the CAD models of the fractal surface "pores" with different surface roughness, ξ. To maintain consistency, each fractal "pore" was composed of 25 small segments. Each segment was a cube with a dimension of 18.9 mm × 18.9 mm × 18.9 mm, as discussed

in section 7.3.2.1. However, the pores had different surface roughness, and the fractal model was designed according to the description in Section 7.3.1.

Owing to the limited RAM of a personal laptop, the time required to simulate the entire fractal surface "pore" would be prohibitive, particularly, for 3rd generation fractal pores. Therefore, a fractal pore consisting of three segments was used as the simulation domain (Figure 7.12).

(a) N = 1 ξ = 1.44

(b) N = 2 ξ = 2.09

(c) N = 3 ξ = 3.01
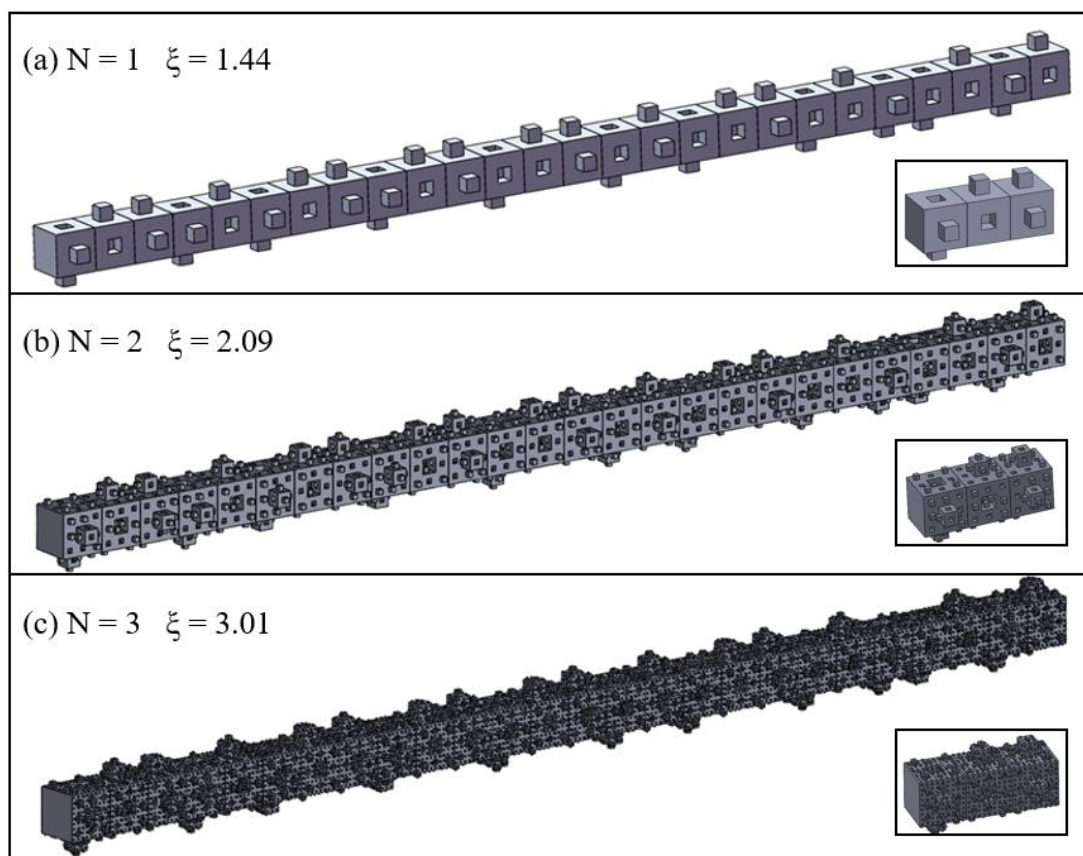
Figure 7.12 Computer-aided design (CAD) models of the fractal "pore" (a) 1st generation fractal tube; (b) 2nd generation fractal tube; and (c) 3rd generation fractal tube

7.4.1.2 Simulation procedure

Figure 7.12 shows the simulation domains modelled using the COMSOL molecular flow module. All simulation procedures were conducted using a Lenovo Air 13 IWL with 1.99 GHz Intel (R) Core (TM) i7-8565U CPU and 8 GB RAM. The molecular flow through the fractal surface "pore" was described using the parameters listed in Table 7.2. A reservoir at a certain pressure, P_0, which was used to generate the incoming flux, and a high-vacuum reservoir were used as the boundary conditions of

the models. The simulations were performed in increasing order of fractal generations to determine the effect of the surface roughness of the pore on Knudsen diffusion.

Table 7.2 Parameters used for the simulation of the Knudsen diffusivity in pores with a fractal surface

Parameter	Description	Value	Unit
Geometry			
R_S	Characteristic length	18.9×10^{-3}	m
L	Pore length	56.7×10^{-3}	m
r	1st generation smallest feature	6.3×10^{-3}	m
	2nd generation smallest feature	2.1×10^{-3}	m
	3rd generation smallest feature	0.7×10^{-3}	m
Operating conditions			
P_0	Reservoir pressure	5×10^{-5}	mbar
T_0	Temperature	293.15	K
M_w	Molecular weight	0.028	kg/mol

7.4.1.3 Simulation results and discussion

During the simulation, nitrogen gas was passed through the "three-segments" pore (Figure 7.12) from the incoming reservoir at a fixed pressure of 5×10^{-5} mbar to the high-vacuum reservoir. The flux of the molecules entering the fractal pore from the high-vacuum end was assumed to be negligible. The fixed pressure ensured that the Knudsen number of the flow was significantly higher than 1. During the COSMOL simulation, an increase in the number of the fractal generations (i.e., N) resulted in two hypotheses. First, the total complexity (surface roughness) of the pore increased with an increase in N, thus significantly increasing the number of collisions of a nitrogen molecule with the fractal surface. Second, with increasing N, a molecule entered into more fjords (surface irregularity), thereby significantly increasing the residence time of the molecule in the pore with a rougher fractal surface.

Figure 7.13 shows the Knudsen diffusion coefficients of the pores as a function of the fractal surface roughness. At lower roughness levels ($\xi < 1.5$), the effect of the surface roughness on the Knudsen diffusivity was significant, and the diffusion coefficient rapidly decreased with increasing roughness. At higher roughness levels ($\xi > 1.5$), the Knudsen diffusivity decreased more gradually. The simulation results revealed that the surface roughness of the pores had a significant effect on the Knudsen diffusivity. At a

constant fractal pore average pore cross-section, the residence time of a high-surface roughness pore was longer than that of a low-surface roughness pore, resulting in differences in the Knudsen diffusion coefficients. This also proves that the Knudsen diffusivity is a function of the pore surface roughness in a sufficiently long pore with a finite concentration gradient.
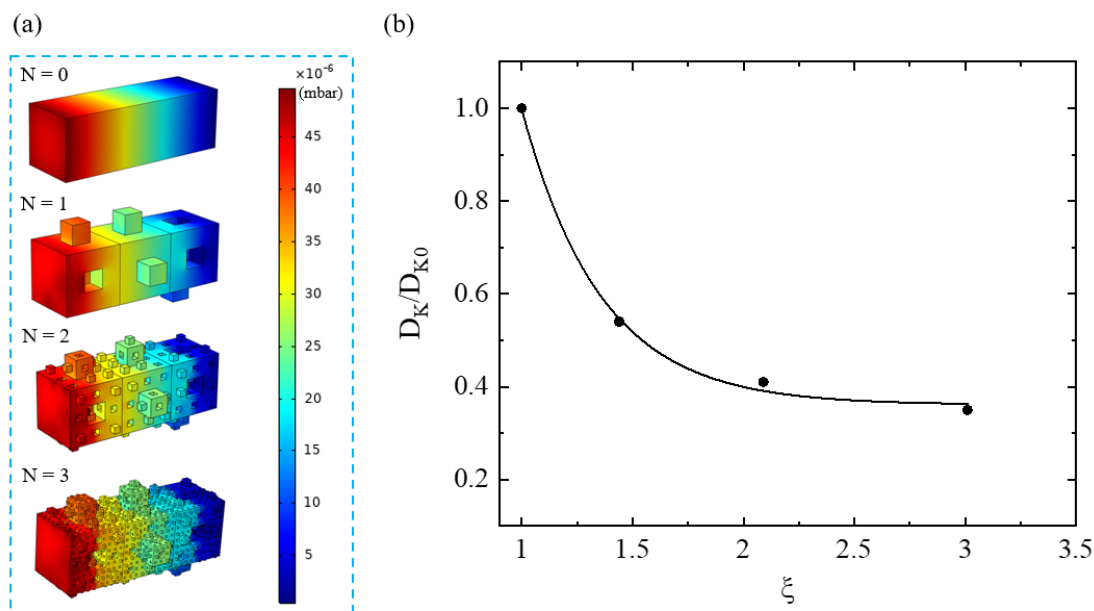
Figure 7.13 (a) Computer generated image of the pressure distribution in the rough-surface segments with fractal generation N = 1, 2, and 3. Simulations were conducted with nitrogen diffusing from the incoming reservoir at a fixed pressure of 5×10^{-5} mbar. (b) Knudsen diffusion coefficient of the fractal pores as a function of the roughness (ξ). The points represent the ratio of diffusivities in same-volume pores with a rough surface to those with a smooth surface (N = 0). The fitted line is an exponential decay function ($R^2 = 0.99775$).

A similar trend was observed by Malek and Coppens by using Monte Carlo simulations [4], however, their predictions for the Knudsen diffusion coefficients are larger than the values in Figure 7.13 (b). The reason could be the shortness of the simulated model (Figure 7.13 (a)). When the fractal pore is short, the effect of pore surface roughness is slightly weakened; there is a significant fraction of gas molecules that can exit the pore directly, resulting in a less pronounced effect of the fjords, which indicates a combination of pore length and roughness effects in the results shown here. Knudsen diffusion in a pore is directly related to the expected residence time of individual gas

molecules.

To further investigate the effect of the pore surface roughness on Knudsen diffusion, the roughness in the radial direction, in which the pore was smooth in the direction of diffusion, was simulated. The simulations of the fractal cross-sections of the smooth pore were conducted to determine the trapping of molecules in the radial direction of the pore (Figure 7.14). The results revealed that there was no significant difference between the Knudsen diffusion coefficients of the pores with a longitudinally smooth-surface and different fractal cross-sections, wherein the residence time of molecules remained approximately constant. The simulation results are in general agreement with kinetic Monte Carlo simulations by Malek and Coppens, indicating that anisotropically rough pores with fractal cross-section do not affect diffusion in axial direction [4].
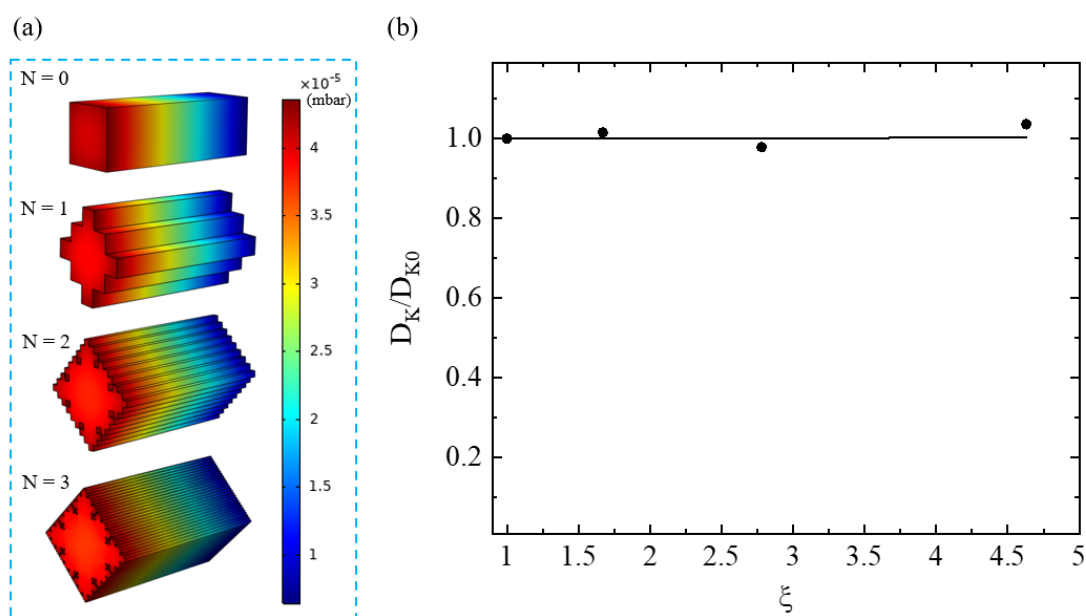
Figure 7.14 (a) Computer generated image of the pressure distribution in the smooth-surface segments with radial fractal $N = 1, 2,$ and 3; (b) Knudsen diffusion coefficient of the smooth-surface segments as a function of the roughness (ξ)

7.4.2 Suggestions for experimental measurements using the UHV-DA

The simulation results revealed that the pore surface roughness had a significant effect on the Knudsen diffusivity. Therefore, future studies should focus on the experimental investigation of the effect of pore surface roughness on the Knudsen diffusion in the

UHV-DA using fractal surface tubes with various roughness factors. In addition, there are some factors that should be carefully considered to accurately measure the Knudsen diffusion coefficient.

7.4.2.1 Vacuum properties of the 3D-printed fractal tube

The previously tested PA2200 fractal surface model was limited to two segments with a length of 37.8 mm. This indicates that any observed problem will be enormously increased by a factor of 13 for a 0.5 m tube. The expected problems of the 0.5 m PA2200 tube inside the UHV-DA are as follows:

1. Generally, plastics contain a large amount of softeners to maintain their physical properties over time [209]. These softeners are large organic molecules that evaporate under a pressure range of 1 to 10^{-4} mbar. Therefore, the material used for the 3D printed parts in UHV-DA should be pure and contain no softeners, as even a small fraction of softeners will render the fractal model unusable.

2. Under atmospheric conditions, a thick layer of water molecules builds up on the surface of PA2200 tube. Consequently, the UHV-DA will require a longer time to reach the minimum pressure (i.e., 1×10^{-8} mbar). Particularly, this problem is expected to play a dominant role at pressures below 10^{-2} mbar.

3. Generally, PA2200 nylon materials contain large amounts of water [210]. When a PA2200 tube is placed inside the UHV-DA, the diffusion in the apparatus will facilitate the gradual release of water molecules from the material. This problem is expected to play a dominant role at pressures below 10^{-4} mbar.

Although two segments of PA2200 nylon used in the laboratory experiments displayed good vacuum compatibility, as shown in Figure 7.11, the impacts of these issues mentioned before may significantly increase for a 0.5 m tube, leading to an excessively long pump time to attain 1×10^{-8} mbar or even failing to reach an ultra-high vacuum environment. To avoid these issues, the material used for 3D printing should be carefully selected and prepared before being applied in the UHV-DA. Alternatively, medical-grade nylon material can be used as a substitute for the current lab-used PA2200 nylon, as this material can exhibit a better performance with proper preparation, as discussed in Section 7.3.3.

7.4.2.2 Modification of the 3D-printed tube

The stability of the PA2200 3D-printed tube significantly affected its application in the UHV-DA. The tested PA2200 3D-printed tube had a very rough surface with a large amount of attached loose powder, which continuously shed particles. Figure 7.14 shows the microscopic images of the surface of the 3D-printed part. The PA2200 3D-printed tube exhibited a rough surface with unfused nylon particles. This indicates that the energy density transmitted to the powder particle on the surface of the printed tube was insufficient [211]. Consequently, large pores were formed on the surface of the 3D printed part, which made the part unusable for diffusion measurements and resulted in fatigue cracks [212]. In addition, a notable concavity with a depth of approximately 100 μm can be observed in the microscopic images at the right side of Figure 7.15.
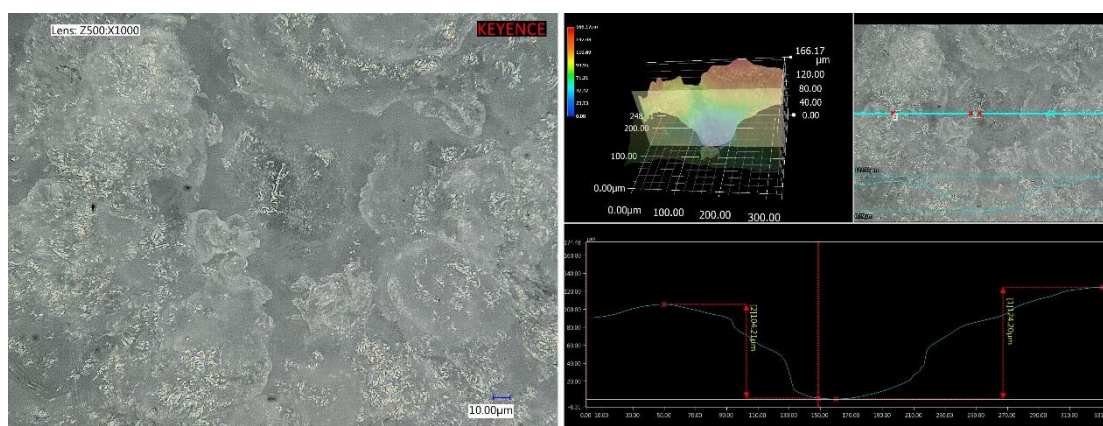
Figure 7.15 Microscopic image (left) and feature analysis obtained using KEYENCE software (right) of the PA2200 3D-printed part

To investigate the effect of roughness on Knudsen diffusion, the 3D-printed geometry should be as perfect as possible to avoid any discrepancy between the experimental and theoretical geometries, which leads to unconvincing results. Post-annealing is an effective method for obtaining a smoother geometry; however, it is important to precisely control the temperature to avoid overheating and deformation of the fractal structures. In addition, a near-perfect 3D-printed geometry can be obtained by adding carbon fibres to PA2200 to form a composite material that can be used for selective laser sintering (SLS). The added carbon fibres enable the formation of a 3D-printed part with a significantly uniform surface with smaller pores and less porosity [211]. Electroplating can also be used to improve the surface of 3D-printed part. This can be

achieved by depositing copper, gold, or stainless steel (SS) on the surface of the 3D-printed geometry to generate a conductive layer of the metal material on the surface of the 3D-printed part [213]. This procedure modifies the surface and enhances the strength of the structure.

7.4.2.3 Accuracy of the measurements

In this study, the UHV-DA was developed to accurately measure the Knudsen diffusion coefficient in the aforementioned non-fractal surface tubes. However, the vacuum features were extremely complicated for the introduction of the entire 3D-printed model into the system. Therefore, two aspects should be considered before experimentally measuring the Knudsen diffusion coefficient.

1. Although it would be extremely difficult to achieve equal ultimate pressures in the left and right chambers for every measurement, an approximate equivalence is necessary. The differences in the ultimate pressures of the left and right chambers are usually caused by gauge calibration and the turbomolecular pump working properties, which should be investigated before the measurements to avoid measurement discrepancies between each measurement. In addition, temperature and humidity are crucial factors, which should be kept constant. Therefore, monitoring these factors prior to and during the experiments is essential.

2. As discussed in Chapter 3, the accuracy of the WRG gauge and AIGX gauge was +/- 30% and +/- 15%, respectively. When a fractal surface model is introduced into the UHV-DA system, the effect of the surface roughness on the Knudsen diffusivity is related to the accuracy of the pressure gauges and could be very sensitive. Therefore, the accuracy of the pressure gauges should be further improved by employing more gauges or professional calibration using a vacuum company. Otherwise, it could be difficult to accurately determine the influence of roughness.

CHAPTER

EIGHT

8 Summary and outlook

8.1 Research summary

In this study, a novel UHV-DA was developed, and the apparatus was utilised to fundamentally understand Knudsen diffusion in complex pore channels. The novel UHV-DA was developed through a conceptual and practical design. Analytical calculations and computer simulations were employed as crucial complements to guide the detailed design of the UHV-DA, such as the pumping speed. Furthermore, a numerical simulation approach (i.e., Molflow+) was employed to quantitatively determine the system parameters to avoid empirical errors during the design process. The UHV-DA was developed based on a steady design, and the crucial vacuum components were calibrated before measuring the Knudsen diffusivity. Leakage is serious issue in ultra-high vacuum systems. Therefore, in this study, to prevent leakage in the UHV-DA, the UHV-DA was subjected to a leak test using a residual gas analyser (RGA) in both the analogue and leak detection modes to identify leaking locations.

The further investigations carried out in this study were predominantly concerned with the application of the UHV-DA for the determination of Knudsen diffusion in complex pore channels. Before using the apparatus to determine the Knudsen diffusion coefficients in various channels, the performance of the UHV-DA in a 0.5 m cylindrical SS tube with a uniform cross-section was compared to the theoretical results calculated by the pioneers. The results revealed that the UHV-DA measurements of the Knudsen diffusion coefficient in the cylindrical channel were reasonable and consistent with the

theoretical results. As previously discussed, during the experimental simulation of the UHV-DA, the effect of the channel length (i.e., 0.25 m vs. 0.5 m channels) and cross-sectional shape (i.e., circular vs. square cross-sections) were investigated. The results of the numerical investigation were compared to those of the experimental measurements using the UHV-DA, and they were found to be consistent.

Based on the experimental and numerical results, channels with a Koch fractal surface with $N = 1, 2$, and 3 generations were fabricated using the 3D printing technique *via* SLS. Owing to the limitations of 3D printing, each of the fractal surface channels was divided into several segments, which were glued together using Araldite® 2020. The surface conditions of the 3D-printed segments, such as the structural defects and blockages, were investigated using a microscope.

Although the experimental validation of the effect of the fractal surface roughness on the Knudsen diffusivity in the UHV-DA has not been completed because of COVID-19, the effect of the surface roughness was numerically investigated using COMSOL. The simulation results indicate that the performance of a channel with a fractal surface with $N = 3$ exhibited the smallest Knudsen diffusion coefficient, which could be attributed to the longer residence time caused by the complexity of the fractal surface. The simulation results reveal that the surface roughness of the pores has a significant effect on the Knudsen diffusivity. Comparing the results with Monte Carlo simulations [4], the Knudsen diffusivities attained by COMSOL are smaller, which could be caused by pore length effects.

8.2 Future directions

8.2.1 Improving the UHV-DA

Future studies should focus on improving the automation of the UHV-DA. This can be achieved using a LabView system [214]. A LabView system can be developed and implemented for the remote access and monitoring of the UHV-DA, which will not only control the systems (integrating all hardware with programme) but also acquire and analyse data. In this study, the results of the experimental analysis using the UHV-DA were obtained from the pressure gauges. Each measurement was repeated at least four times to ensure the statistical relevance of the results by (i) increasing the pressure up

to but not above the desired pressure, and (ii) decreasing the pressure down to but not below the desired pressure. Although the experimental procedure was carefully performed to obtain the most accurate data, it was difficult to avoid experimental errors from the instrument owing to the accuracy of the pressure gauges (up to 30%). Therefore, future studies should focus on replacing the WRG/AIGX with high-accuracy grade gauges.

8.2.2 Investigation of the effect of surface roughness on Knudsen diffusion

Future studies should focus on using the UHV-DA to investigate Knudsen diffusion in different fractal surface channels. To successfully employ the UHV-DA to investigate the effect of surface roughness on the Knudsen diffusion, some factors should be improved to enhance the performance of the apparatus.

1. The 3D-printed fractal model should be developed using materials without attached loose powders. Although SLS is a cheap and fast technique for printing complex structures, the use of nylon powder affects the quality of the printed structure regardless of the pre-treatment method employed. In addition, the outgassing rate of nylon is much higher than that of stainless steel. Ideally, the SLS approach could be replaced with the metal 3D printing technique to rapidly obtain reliable results in ultra-high vacuum, however, metal 3D printing is very costly. Electroplating is another way to improve the surface properties of 3D-printed nylon part by depositing a metal film, which could be used for future modification.

2. For future studies on more complex channels, the printing of the entire channel rather than gluing segments with epoxy glue should be considered. Although the outgassing effect of epoxy glue is very limited for two segments (shown in Section 7.3.3), this issue could extensively increase for a 0.5-m tube. Therefore, whole channel integral printing is recommended, as this could significantly reduce the outgassing issue and shorten the pump down time.

3. In this study, the 3D-printed fractal models were designed using SOLIDWORKS, which is a CAD program with limited patterns for each generation. For example, the third-generation pore model has over 200,000 individual surfaces. For higher generation pore models, the CAD program is not an appropriate tool for model

generation. Another programming package should be used to generate more complex models to import in COMSOL rather than the CAD program in the future.

8.2.3 Investigation of self-diffusion in complex pore channels

The application of the UHV-DA is not limited to Knudsen diffusion due to concentration gradients, but could potentially be extended to tracer or self- diffusion in the Knudsen regime, with minor modifications (Figure 8.1). A sample gas cylinder and pulse valve should be added to the current vacuum system. The pulse valve is used to generate a reproducible concentration pulse of the sample gas along with carrier gas before both gases enter the vacuum system. The residual gas analyser could detect the sample gas in the system to investigate the self- diffusivity in complex pore channels directly.
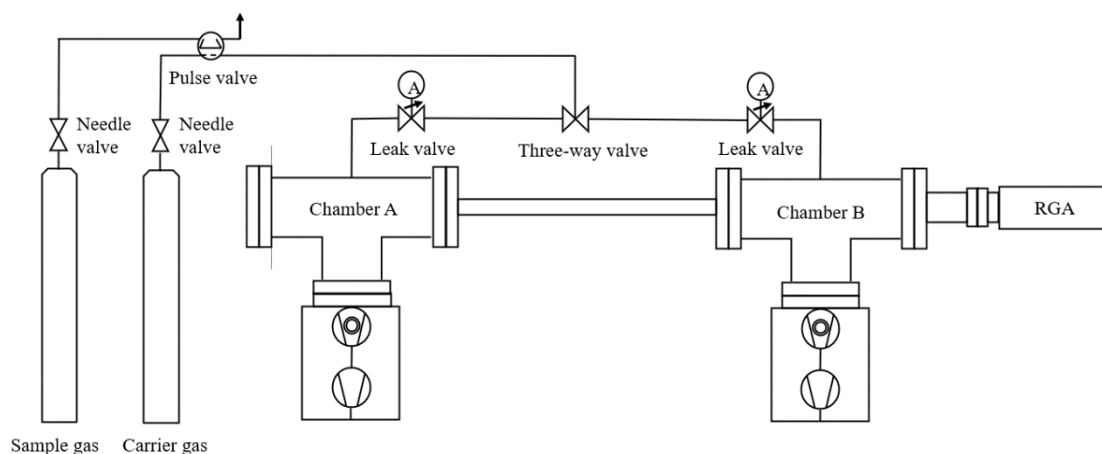
Figure 8.1 Schematic of the modified UHV-DA to enable meaurement of self- diffusion

Appendix A

Table A.1 Transmission probabilities for short tubes [41]

l/d	f
0.05	0.952399
0.25	0.801271
0.5	0.671984
1	0.514231
2	0.356572
3	0.275438
4	0.225263
5	0.190941
10	0.109304
15	0.076912
20	0.059422
25	0.048448

Table A.2 Transmission probabilities for rectangular tubes [88]

l/a	b/a				
	1	2	4	8	16
0.01	0.9902	0.9926	0.9938	0.9944	0.9947
0.1	0.9131	0.9326	0.9425	0.9475	0.9500
1	0.5363	0.6026	0.6421	0.6631	0.6737
2	0.3780	0.4444	0.4893	0.5150	0.5285
4	0.2424	0.2977	0.3404	0.3679	0.3833
7	0.1596	0.2020	0.2380	0.2639	0.2796
10	0.1195	0.1537	0.1843	0.2078	0.2230
20	0.0655	0.0864	0.1066	0.1238	0.1366
40	0.0346	0.0464	0.058	0.0695	0.078
70	0.020	0.0275	0.035	0.042	0.048
100	0.014	0.019	0.025	0.030	0.035

Table A.3 Approximate outgassing rates of various vacuum materials with different treatment [109, 112]

Materials	Treatment	Outgassing rate $(mbar \cdot L \cdot s^{-1} \cdot cm^{-2})$
Aluminium	Fresh	2.2×10^{-7}
	Baked (15hr @250°C)	4.0×10^{-13}
Brass	Cast	1.1×10^{-6}
Copper	Fresh	1.8×10^{-8}
	Mechanically polished	2.2×10^{-8}
Gold	Fresh	8.5×10^{-8}
Polystyrene		2×10^{-5}
PVC		2.4×10^{-6}
Stainless steel	Fresh	1.5×10^{-8}
	Mechanically polished	4.2×10^{-9}
	Baked (30hr @ 250°C)	3×10^{-12}
Teflon		1.1×10^{-6}
Viton A	Fresh	8.5×10^{-7}
	Baked (10hr @150°C)	1.7×10^{-9}

Appendix B

Table B.1 Technical date of EOS FORMIGA P 100 [196, 215]

FORMIGA P 100	
Effective building volume	200 mm x 250 mm x 330mm
Building speed (material-dependent)	up to 24 mm height/hour
Layer thickness (material-dependent)	0.1 mm
Support structure	not necessary
Laser type	CO_2, 30W
Scan speed during building	up to 5 m/s
Power supply	16 A
Power consumption	2 kW
Dimensions	
Printer with powder containers and touch screen	1,320 mm x 1,067 mm x 2,204 mm
Weight	600 kg
Recommended installation space	3.2 m x 3.5 m x 3 m
Data preparation	
PC	Windows operating system
Software	EOS RP Tools
CAD interface	STL Optional: converter to all common formats

Nomenclature

a_{1h}	specific outgassing rate after, mbar L s^{-1} cm^{-2}
A	cross-sectional area of the tube, m^2
$A_{surface}$	geometrical surface area, m^2
$A_{aperture}$	aperture area, m^2
A_{facet}	area of the facet
c	concentration, mol m^{-3}
C	conductance, m^3 s^{-1}
$C_{aperture}$	conductance of an aperture, m^3 s^{-1}
C_{long}	conductance of a long circular cross-section tube, m^3 s^{-1}
C_{short}	conductance of a short circular cross-section tube, m^3 s^{-1}
C_{total}	total conductance of the vacuum system, m^3 s^{-1}
C_v	conductance of a circular cross-section tube in laminar flow, m^3 s^{-1}
d	diameter of a tube, m
d_{gas}	effective diameter of a gas molecule, m
d_p	mean pore size of the porous media, m
D	diffusion coefficient in the bulk, m^2 s^{-1}
D_{eff}	effective diffusion coefficient in porous media, m^2 s^{-1}
D_K	Knudsen diffusion coefficient, m^2 s^{-1}
$D_{K,c}$	Knudsen diffusion coefficient in uniform circular cross-section cylindrical tube, m^2 s^{-1}
D^*	diffusion coefficient in transition regime, m^2 s^{-1}
f_{long}	transmission probability of a long cylindrical tube
f_{short}	transmission probability of a short cylindrical tube
$I_\perp$	orthogonal momentum, kg m s^{-1}
J	flux of the diffusing species, mol m^{-2} s^{-1}
k_B	Boltzmann constant, J K^{-1}
Kn	Knudsen number
l	length of a tube, m
L	characteristic length, m
m'	mass flow rate, kg s^{-1}

M	molecular weight of the diffusing species, kg mol^{-1}
M_i	molecular weight for the i-th species, kg mol^{-1}
N_{hit}	number of test particles hits on the facets
n	amount of gas, mol
N_{real}	total amount of real particles on the source facets
p	the pressure, Pa
p_d	downstream pressure, Pa
p_u	upstream pressure, Pa
p_{ult}	ultimate pressure, Pa
$\bar{p}$	average pressure between the entrance and exit, Pa
p_{entr}	entrance pressure, Pa
p_{exit}	exit pressure, Pa
p_{peri}	perimeter, m
Q	throughput, Pa m^3 s^{-1}
Q_{ac}	accumulated gas load, Pa m^3 s^{-1}
Q_{diff}	gas load through the tube, Pa m^3 s^{-1}
Q_{in}	gas flow entering the vacuum system (including systematic outgassing or process gas, etc.), Pa m^3 s^{-1}
Q_{leak}	leakage of the system, Pa m^3 s^{-1}
Q_{otgs}	outgassing of the system, Pa m^3 s^{-1}
Q_{out}	gas flow pumped out using a pump, Pa m^3 s^{-1}
Q_{outgas}	outgassing of all gas-particle inlet sources, Pa m^3 s^{-1}
Q_{total}	total flow rate, Pa m^3 s^{-1}
R	gas constant, J K^{-1} mol^{-1}
S_1	pumping speed of the left pump, m^3 s^{-1}
S_2	pumping speed of the right speed, m^3 s^{-1}
S_{eff}	effective pumping speed, m^3 s^{-1}
S_{manu}	pumping speed provided by manufacturer, m^3 s^{-1}
T	thermodynamic temperature, K
$v_\perp$	orthogonal velocity, m s^{-1}
$\bar{v}$	mean speed of the gas molecules, m s^{-1}
V	volume of a gas, m^3
$V_{chamber}$	volume of a chamber, m^3
V'	volumetric flow rate, m^3 s^{-1}

x diffusion path, m

Greek

α decay exponent

η viscosity of the fluid, Pa s^{-1}

θ incident angle of test particles

λ gas mean free path, m

μ chemical potential, J mol^{-1}

μ_0 standard chemical potential, J mol^{-1}

τ tortuosity of the porous media

ϕ porosity of the porous media

Ω cross-sectional area, m^2

Abbreviation

AIGX   Active ion gauge

CAD   Computer-aided design

CERN   European Organization for Nuclear Research

CF   ConFlat

CPA   Control Performance Analyzer

DMLS   Direct metal laser sintering

HV   High vacuum

KF   Klein Flansche

NASA   National Aeronautics and Space Administration

RAM   Random access memory

SLA   Stereolithograhy

SLS   Selective laser sintering

SP   Set point

SS   Stainless steel

RGA   Residual gas analyzer

TIC   Turbo & Instrument controllers

TMP   Turbomolecular pump

TPMC   Test particle Monte Carlo

UHV   Ultra-high vacuum

UHV-DA   Ultra-high vacuum diffusion apparatus

VAT   Variable leak valve

WRG   Wide range gauge

References

[1] R. Millington, *Gas diffusion in porous media.* Science, 1959. **130**(3367): p. 100-102.

[2] D.M. Tartakovsky and M. Dentz, *Diffusion in porous media: phenomena and mechanisms.* Transport in Porous Media, 2019. **130**(1): p. 105-127.

[3] K. Malek and M.-O. Coppens, *Effects of surface roughness on self-and transport diffusion in porous media in the Knudsen regime.* Physical review letters, 2001. **87**(12): p. 125505.

[4] K. Malek and M.-O. Coppens, *Knudsen self-and Fickian diffusion in rough nanoporous media.* The Journal of chemical physics, 2003. **119**(5): p. 2801-2811.

[5] M. Thommes, K. Kaneko, A.V. Neimark, J.P. Olivier, F. Rodriguez-Reinoso, J. Rouquerol, and K.S.W. Sing, *Physisorption of gases, with special reference to the evaluation of surface area and pore size distribution (IUPAC Technical Report).* Pure and Applied Chemistry, 2015. **87**(9-10): p. 1051-1069.

[6] M. Knudsen, *Die molekularströmung der gase durch offnungen und die effusion.* Annalen der Physik, 1909. **333**(5): p. 999-1016.

[7] M. v. Smoluchowski, *Zur kinetischen theorie der transpiration und diffusion verdünnter gase.* Annalen der Physik, 1910. **338**(16): p. 1559-1570.

[8] P. Clausing, *Über die Strömung sehr verdünnter Gase durch Röhren von beliebiger Länge.* Annalen der Physik, 1932. **404**(8): p. 961-989.

[9] W. Strieder and S. Prager, *Knudsen flow through a porous medium.* The Physics of Fluids, 1968. **11**(12): p. 2544-2548.

[10] P. Levitz, *Knudsen diffusion and excitation transfer in random porous media.* The Journal of Physical Chemistry, 1993. **97**(15): p. 3813-3818.

[11] J. Evans, M. Abbasi, and A. Sarin, *A Monte Carlo simulation of the diffusion of gases in porous solids.* The Journal of Chemical Physics, 1980. **72**(5): p. 2967-2973.

[12] Y. Nakano, S. Iwamoto, I. Yoshinaga, and J. Evans, *The effect of pore necking on Knudsen diffusivity and collision frequency of gas molecules with pore walls.* Chemical engineering science, 1987. **42**(7): p. 1577-1583.

[13] V.N. Burganos and A.C. Payatakes, *Knudsen diffusion in random and correlated networks of constricted pores.* Chemical engineering science, 1992. **47**(6): p. 1383-1400.

[14] M.M. Tomadakis and S.V. Sotirchos, *Ordinary, transition, and Knudsen regime diffusion in random capillary structures.* Chemical engineering science, 1993. **48**(19): p. 3323-3333.

[15] V.N. Burganos and S.V. Sotirchos, *Simulation of Knudsen diffusion in random networks of parallel pores.* Chemical engineering science, 1988. **43**(7): p. 1685-1694.

[16] Y. Shi, Y.T. Lee, and A.S. Kim, *Knudsen diffusion through cylindrical tubes of varying radii: theory and Monte Carlo simulations.* Transport in porous media, 2012.

93(3): p. 517-541.

[17] M.-O. Coppens, *The effect of fractal surface roughness on diffusion and reaction in porous catalysts–from fundamentals to practical applications.* Catalysis Today, 1999. **53**(2): p. 225-243.

[18] I. Karatzas and S.E. Shreve, *Brownian motion*, in *Brownian Motion and Stochastic Calculus.* 1998, Springer. p. 47-127.

[19] T. Graham, *A short account of experimental researches on the diffusion of gases through each other, and their separation by mechanical means.* Quarterly Journal of Science, Literature and Art, 1829. **27**: p. 74-83.

[20] J.C. Maxwell, *IV. On the dynamical theory of gases.* Philosophical transactions of the Royal Society of London, 1867(157): p. 49-88.

[21] A. Fick, *Ueber diffusion.* Annalen der Physik, 1855. **170**(1): p. 59-86.

[22] A. Einstein, *On the motion of small particles suspended in liquids at rest required by the molecular-kinetic theory of heat.* Annalen der physik, 1905. **17**(549-560): p. 208.

[23] F.J. Keil, *Diffusion and reaction in porous networks.* Catalysis Today, 1999. **53**(2): p. 245-258.

[24] R. Evans III, G.M. Watson, and E. Mason, *Gaseous diffusion in porous media at uniform pressure.* The journal of chemical physics, 1961. **35**(6): p. 2076-2083.

[25] A.S. Joshi, K.N. Grew, A.A. Peracchio, and W.K. Chiu, *Lattice Boltzmann modeling of 2D gas transport in a solid oxide fuel cell anode.* Journal of power sources, 2007. **164**(2): p. 631-638.

[26] E.A. Mason, A.P. Malinauskas, and R.B. Evans, III, *Flow and Diffusion of Gases in Porous Media.* Journal of Chemical Physics, 1967. **46**: p. 3199.

[27] S.M. Clifford and D. Hillel, *Knudsen diffusion: The effect of small pore size and low gas pressure on gaseous transport in soil.* Soil science, 1986. **141**(4): p. 289-297.

[28] E. Nagy, *Basic equations of mass transport through a membrane layer*. 2018: Elsevier.

[29] N. Dongari, A. Sharma, and F. Durst, *Pressure-driven diffusive gas flows in micro-channels: from the Knudsen to the continuum regimes.* Microfluidics and nanofluidics, 2009. **6**(5): p. 679-692.

[30] R.B. Bird, W.E. Stewart, and E.N. Lightfoot, *Transport phenomena*. Vol. 1. 2006: John Wiley & Sons.

[31] J. Kärger, D.M. Ruthven, and D.N. Theodorou, *Diffusion in nanoporous materials*. 2012: John Wiley & Sons.

[32] A. Fick, *London, Edinburgh Dublin Philos. Mag.* J. Sci, 1855. **10**(63): p. 30-39.

[33] D. Mu, Z.-S. Liu, C. Huang, and N. Djilali, *Determination of the effective diffusion coefficient in porous media including Knudsen effects.* Microfluidics and Nanofluidics, 2008. **4**(3): p. 257-260.

[34] H.L. Weissberg, *Effective diffusion coefficient in porous media.* Journal of Applied Physics, 1963. **34**(9): p. 2636-2639.

[35] A. Taghavinejad, M. Sharifi, E. Heidaryan, K. Liu, and M. Ostadhassan, *Flow*

modeling in shale gas reservoirs: A comprehensive review. Journal of Natural Gas Science and Engineering, 2020: p. 103535.

[36] W. Pollard and R.D. Present, *On gaseous self-diffusion in long capillary tubes.* Physical Review, 1948. **73**(7): p. 762.

[37] R.E. Cunningham and R. Williams, *Diffusion in gases and porous media*. Vol. 1. 1980: Springer.

[38] P. Clausing, *Über das Kosinusgesetz der Zurückwerfung als Folge des zweiten Hauptsatzes der Thermodynamik.* Annalen der Physik, 1930. **396**(5): p. 533-566.

[39] S. Dushman and S.C. Brown, *Scientific foundations of vacuum technique.* AmJPh, 1962. **30**(8): p. 612-612.

[40] R. Cole, *Complementary variational principles for Knudsen flow rates.* IMA Journal of Applied Mathematics, 1977. **20**(1): p. 107-115.

[41] J.M. Lafferty, *Foundations of vacuum science and technology*. 1998: Wiley New York.

[42] N. Wakao, S. Otani, and J. Smith, *Significance of pressure gradients in porous materials: Part I. Diffusion and flow in fine capillaries.* AIChE Journal, 1965. **11**(3): p. 435-439.

[43] W. Kast and C.-R. Hohenthanner, *Mass transfer within the gas-phase of porous media.* International Journal of Heat and Mass Transfer, 2000. **43**(5): p. 807-823.

[44] D. Davis, *Monte Carlo calculation of molecular flow rates through a cylindrical elbow and pipes of other shapes.* Journal of Applied Physics, 1960. **31**(7): p. 1169-1176.

[45] J. Feder, *The Fractal Dimension*, in *Fractals*. 1988, Springer. p. 6-30.

[46] D. Avnir, D. Farin, and P. Pfeifer, *Molecular fractal surfaces.* Nature, 1984. **308**(5956): p. 261-263.

[47] S. Stokke, S. Brainerd, and J.M. Arnemo, *Metal deposition of copper and lead bullets in moose harvested in Fennoscandia.* Wildlife Society Bulletin, 2017. **41**(1): p. 98-106.

[48] M.-O. Coppens, *Accessibility of a Catalyst's Fractal Surface to Diffusing and Reacting Molecules*, in *Fractals in Engineering*. 1997, Springer. p. 336-349.

[49] M.-O. Coppens and G.F. Froment, *Knudsen diffusion in porous catalysts with a fractal internal surface.* Fractals, 1995. **3**(04): p. 807-820.

[50] B.C. Bukowski, F.J. Keil, P.I. Ravikovitch, G. Sastre, R.Q. Snurr, and M.-O. Coppens, *Connecting theory and simulation with experiment for the study of diffusion in nanoporous solids.* Adsorption, 2021: p. 1-78.

[51] Brilliant.org. *Fractals*. No date   [cited 2020 October 19]; Available from: https://brilliant.org/wiki/fractals/.

[52] B. Mandelbrot, *How long is the coast of Britain? Statistical self-similarity and fractional dimension.* science, 1967. **156**(3775): p. 636-638.

[53] B.B. Mandelbrot, *The fractal geometry of nature*. Vol. 1. 1982: WH freeman New York.

[54] B.B. Mandelbrot and J.W. Van Ness, *Fractional Brownian motions, fractional*

noises and applications. SIAM review, 1968. **10**(4): p. 422-437.

[55] F. Hausdorff, *Dimension und äußeres Maß.* Mathematische Annalen, 1918. **79**(1-2): p. 157-179.

[56] P. Pfeifer and D. Avnir, *Chemistry in noninteger dimensions between two and three. I. Fractal theory of heterogeneous surfaces.* The Journal of chemical physics, 1983. **79**(7): p. 3558-3565.

[57] D. Avnir, *Fractal approach to heterogeneous chemistry.* 1989: Wiley.

[58] T. Elias-Kohav, S. Moshe, and D. Avnir, *Steady-state diffusion and reactions in catalytic fractal porous media.* Chemical engineering science, 1991. **46**(11): p. 2787-2798.

[59] P. Adler and J.-F. Thovert, *Fractal porous media.* Transport in porous media, 1993. **13**(1): p. 41-78.

[60] J. Cai and C. Sorensen, *Diffusion of fractal aggregates in the free molecular regime.* Physical Review E, 1994. **50**(5): p. 3397.

[61] M.-O. Coppens and G.F. Froment, *Diffusion and reaction in a fractal catalyst pore—I. Geometrical aspects.* Chemical engineering science, 1995. **50**(6): p. 1013-1026.

[62] S. Santra and B. Sapoval, *Interaction of ballistic particles with irregular pore walls, Knudsen diffusion, and catalytic efficiency.* Physical Review E, 1998. **57**(6): p. 6888.

[63] M.-O. Coppens and A.J. Dammers, *Effects of heterogeneity on diffusion in nanopores—from inorganic materials to protein crystals and ion channels.* Fluid phase equilibria, 2006. **241**(1-2): p. 308-316.

[64] Unknown, *How to Make an Experimental Geissler Tube.* Popular Science Monthly, February, 1919: p. Unnumbered page.

[65] A. Chambers, *Modern Vacuum Physics.* 2004: CRC Press.

[66] A. Chambers, *Basic vacuum technology.* 1998: CRC Press.

[67] E.A. Pozzi, G. Goubert, N. Chiang, N. Jiang, C.T. Chapman, M.O. McAnally, A.-I. Henry, T. Seideman, G.C. Schatz, and M.C. Hersam, *Ultrahigh-vacuum tip-enhanced Raman spectroscopy.* Chemical reviews, 2017. **117**(7): p. 4961-4982.

[68] K.A. Schug, I. Sawicki, D.D. Carlton Jr, H. Fan, H.M. McNair, J.P. Nimmo, P. Kroll, J. Smuts, P. Walsh, and D. Harrison, *Vacuum ultraviolet detector for gas chromatography.* Analytical chemistry, 2014. **86**(16): p. 8329-8335.

[69] Pfeiffer Vacuum. *Semiconductor.* No date   [cited 2020 June 12]; Available from: https://www.pfeiffer-vacuum.com/en/markets/semiconductor/.

[70] M.H. Hablanian, *High-vacuum technology: a practical guide.* 2017: Routledge.

[71] J.F. O'Hanlon, *A user's guide to vacuum technology.* 2005: John Wiley & Sons.

[72] C.B. Nakhosteen and K. Jousten, *Handbook of vacuum technology.* 2016: John Wiley & Sons.

[73] S. Dushman and S.C. Brown, *Scientific foundations of vacuum technique.* American Journal of Physics, 1962. **30**(8): p. 612-612.

[74] P. Danielson, *Contamination in vacuum systems, sources and remedies.* R&D Magazine, 2001.

[75] J.F. O'Hanlon and H.G. Parks, *Impact of vacuum equipment contamination on semiconductor yield.* Journal of Vacuum Science & Technology A: Vacuum, Surfaces, and Films, 1992. **10**(4): p. 1863-1868.

[76] Normandale Community College. *Gas Loads in Vacuum systems*. 2018   [cited 2020 September 1]; Available from: https://www.normandale.edu/departments/stem-and-education/vacuum-and-thin-film-technology/learning-in-a-vacuum---what-to-expect/articles/gas-loads-in-vacuum-systems.

[77] K. Jousten, Thermal outgassing, No. OPEN-2000-274, 1999.

[78] Kurt J. Lesker. *Basic Outgassing Concepts*. No date   [cited 2020 August 10]; Available from:
https://www.lesker.com/newweb/technical_info/vacuumtech/outgas_00_basicconcept.cfm.

[79] R. Elsey, *Outgassing of vacuum materials-II.* Vacuum, 1975. **25**(8): p. 347-361.

[80] W. Perkins, *Permeation and outgassing of vacuum materials.* Journal of vacuum science and technology, 1973. **10**(4): p. 543-556.

[81] P. Chiggiato, *Outgassing properties of vacuum materials for particle accelerators.* arXiv preprint arXiv:2006.07124, 2020.

[82] NASA. *Outgassing Db*. 2020   [cited 2020 October 16]; Available from: https://data.nasa.gov/Applied-Science/Outgassing-Db/r588-f7pr.

[83] L.E. Bergquist and Y.T. Sasaki, *Innovations in helium leak detector systems.* Journal of Vacuum Science & Technology A: Vacuum, Surfaces, and Films, 1992. **10**(4): p. 2650-2654.

[84] P. Vacuum. *Introduction to vacuum technology*. 2018   [cited 2020 August 12]; Available from: https://www.pfeiffer-vacuum.com/en/know-how/.

[85] A. Roth, *Vacuum technology*. 2012: Elsevier.

[86] Q. Zheng, J. Xu, B. Yang, and B. Yu, *Transmission probability for Knudsen diffusion in a single chamber-throat pore.* Vacuum, 2011. **85**(11): p. 1017-1020.

[87] A. Berman, *Free molecule transmission probabilities.* Journal of Applied Physics, 1965. **36**(10): p. 3356-3356.

[88] D. Santeler and M. Boeckmann, *Molecular flow transmission probabilities of rectangular tubes.* Journal of Vacuum Science & Technology A: Vacuum, Surfaces, and Films, 1991. **9**(4): p. 2378-2383.

[89] J. Hengevoss and W. Huber, *The influence of fore-vacuum conditions on ultra-high vacuum pumping systems with oil diffusion pumps.* Vacuum, 1963. **13**(1): p. 1-9.

[90] P. Danielson, *How To Choose a Roughing/Backing Pump for the Turbo and Drag Family.* A Journal of Practical and Useful Vacuum Technology, 2003.

[91] C. Cabuz, W.R. Herb, E.I. Cabuz, and S.T. Lu. *The dual diaphragm pump.* in *Technical Digest. MEMS 2001. 14th IEEE International Conference on Micro Electro Mechanical Systems (Cat. No. 01CH37090)*. 2001. IEEE.

[92] Graco. *Double diaphragm pumps concept and theory*. No date   [cited 2021

March 25]; Available from:
http://wwwd.graco.com/training/concept_and_theory/Double%20Dia.%20Pumps%20v3.pdf.

[93] E.S. Bayley, *Dry rotary vane pump*. 1971, Google Patents.

[94] W. Umrath, *Fundamentals of Vacuum Technology*. 2007: Oerlikon Leybold Vacuum.

[95] V.A. International. *The Oil Sealed Rotary Vane Vacuum Pump – Background and Designs*. 2018   [cited 2021 March 23]; Available from:
https://vacaero.com/information-resources/vacuum-pump-technology-education-and-training/161438-the-oil-sealed-rotary-vane-vacuum-pump-background-and-designs.html.

[96] Z. Li, L. Li, Y. Zhao, G. Bu, and P. Shu, *Theoretical and experimental study of dry scroll vacuum pump.* Vacuum, 2009. **84**(3): p. 415-421.

[97] J.P. Sung, J.H. Boo, and E.G. Jung, *Transient thermodynamic modeling of a scroll compressor using R22 refrigerant.* Energies, 2020. **13**(15): p. 3911.

[98] P.A. Redhead, *Vacuum Science and Technology: Pioneers of the 20th century*. 1997: Springer Science & Business Media.

[99] W. Becker, *The turbomolecular pump, its design, operation and theory; calculation of the pumping speed for various gases and their dependence on the forepump.* Vacuum, 1966. **16**(11): p. 625-632.

[100] M. Hablanian and J. Maliakal, *Advances in diffusion pump technology.* Journal of Vacuum Science and Technology, 1973. **10**(1): p. 58-64.

[101] G.P. Brown, *Use of Silicones as Diffusion Pump Oils.* Review of Scientific Instruments, 1945. **16**(11): p. 316-318.

[102] Enparticles. *Diffusion Pump Workiong Principle*. No date   [cited 2021 March 23]; Available from: https://diffusionpumpoil.com/pages/diffusion-pump-working-principle.

[103] F.-C. Hsieh, P.-H. Lin, D.-R. Liu, and F.-Z. Chen, *Pumping performance analysis on turbomolecular pump.* Vacuum, 2012. **86**(7): p. 830-832.

[104] S. Zheng and C. Wang, *Rotor Balancing for Magnetically Levitated TMPs Integrated With Vibration Self-Sensing of Magnetic Bearings.* IEEE/ASME Transactions on Mechatronics, 2021: p. 1-1.

[105] H. Ishimaru and H. Hisamatsu, *Turbomolecular pump with an ultimate pressure of 10^{-12} Torr.* Journal of Vacuum Science & Technology A: Vacuum, Surfaces, and Films, 1994. **12**(4): p. 1695-1698.

[106] B. Han, Z. Huang, and Y. Le, *Design aspects of a large scale turbomolecular pump with active magnetic bearings.* Vacuum, 2017. **142**: p. 96-105.

[107] L. Shen, *The Design and Performance of a High -Speed Economical Ultrahigh Vacuum Chamber Utilizing Titanium Sublimation.* Review of Scientific Instruments, 1972. **43**(9): p. 1301-1306.

[108] H. Ishimaru, *Bakable aluminium vacuum chamber and bellows with an aluminum flange and metal seal for ultrahigh vacuum.* Journal of Vacuum Science and Technology, 1978. **15**(6): p. 1853-1854.

[109] P. Chiggiato, *Materials and Properties IV Outgassing.* CERN Accelerator School (CAS) on Vacuum for Particle Accelerators, 2017.

[110] P. Danielson, *Choosing the right vacuum materials.* R&D Magazine, 2003.

[111] A.o.V.E. Manufacturers. *Surface Finish Effects on Vacuum Pumpdown Time.* 2021　[cited 2021 July 3]; Available from: https://avem.org/press-releases/featured-articles/item/77-surface-finish-effects-on-vacuum-pumpdown-time.

[112] R. Grinham and A. Chew, *A Review of Outgassing and Methods for its Reduction.* Applied Science and Convergence Technology, 2017. **26**(5): p. 95-109.

[113] D. Herring. *Evaporation.* 2015　[cited 2020 September 17]; Available from: https://vacaero.com/information-resources/the-heat-treat-doctor/1455-evaporation.html.

[114] S. Sgobba, *Vacuum for accelerators: introduction to materials and properties.* arXiv preprint arXiv:2006.02212, 2020.

[115] J.R. Davis, *Stainless steels.* 1994: ASM international.

[116] W.-S. Lee and C.-F. Lin, *Impact properties and microstructure evolution of 304L stainless steel.* Materials Science and Engineering: A, 2001. **308**(1): p. 124-135.

[117] K. Sonderegger. *Vacuum sealing technology.* in *Vacuum in Accelerators Conference.* 2006.

[118] Kurt J. Lesker. *Vacuum Flanges & Components.* No date　[cited 2020 September 11]; Available from: https://www.lesker.com/vacuum-flanges-components.cfm.

[119] A. Roth, *Vacuum sealing techniques.* 1994: Springer Science & Business Media.

[120] Kurt J. Lesker. *OFHC Copper Gaskets for CF Flanges.* No date　[cited 2020 July 16]; Available from: https://www.lesker.com/newweb/flanges/hardware_cf_gaskets.cfm?pgid=ofhc.

[121] M. Sefa, J.A. Fedchak, and J. Scherschligt, *Investigations of medium-temperature heat treatments to achieve low outgassing rates in stainless steel ultrahigh vacuum chambers.* Journal of Vacuum Science & Technology A: Vacuum, Surfaces, and Films, 2017. **35**(4): p. 041601.

[122] Edwards Vacuum. *nXDS Dry Scroll Pumps.* No date　[cited 2020 October 22]; Available from: https://www.edwardsvacuum.com/content/dam/brands/edwards-vacuum/edwards-website-assets/high-vacuum/documents/Edwards-nXDS-Dry-Scroll-Pump-Brochure-3601-0088-01.pdf.

[123] Marshall Scientific. *Edwards nXDS6i dry scroll pump.* No date　[cited 2020 September 21]; Available from: https://www.marshallscientific.com/Edwards-nXDS6i-Dry-Scroll-Pump-p/ed-a73501983.htm.

[124] P. Vacuum, *The Vacuum Technology Book.* 2008: Pfeiffer Vacuum.

[125] Edwards Vacuum. *TIC Instrument Controllers.* No date　[cited 2020 October 23]; Available from: https://shop.edwardsvacuum.com/products/r66/list.aspx.

[126] W. Jitschin, *Accuracy of vacuum gauges.* Journal of Vacuum Science & Technology A: Vacuum, Surfaces, and Films, 1990. **8**(2): p. 948-956.

[127] V.S.W. News. *Seven Factors Affecting the Sensitivity of Vacuum Gauges.* 2019

[cited 2021 July 3]; Available from:
https://www.vacuumscienceworld.com/blog/vacuum-gauge-sensitivity.

[128] A. Berman, *Total pressure measurements in vacuum technology*. 2014:
Academic Press.

[129] Edwards Vacuum. *AIGX Active Ion Gauge*. No date   [cited 2020 September
20]; Available from:
https://shop.edwardsvacuum.com/products/d04850000/view.aspx.

[130] Ideal Vacuum. *Edwards AIGX-S Active ION Gauge NW25, KF25, 10-2 to 10-10
Torr*. No date   [cited 2020 September 21]; Available from:
https://www.idealvac.com/Edwards-AIGX-S-Active-ION-Gauge-NW25/pp/P107159.

[131] Edwards Vacuum. *Wide Range Gauge*. No date   [cited 2020 September 21];
Available from: https://shop.edwardsvacuum.com/products/d14790020/view.aspx.

[132] Ideal Vacuum. *Edwards WRG-S-NW25 Active Wide Range Gauge NW25, KF25,
ATM to 10-9 Torr, PN D147-01-000*. No date   [cited 2020 September 21]; Available
from: https://www.idealvac.com/Edwards-WRG-S-NW25-Active-Wide-Range-
Gauge-NW25/pp/P106085.

[133] VAT. *Series 590 Variable leak valve*. No date   [cited 2020 September 26];
Available from: http://www.vatvalve.com/en/business/valves/catalog/E/590_1_V.

[134] BOC. *Nitrogen zero grade (N4.8)*. No date   [cited 2020 August 21]; Available
from: https://www.boconline.co.uk/en/images/nitrogen-zero-grade-n4.8-
factsheet_tcm410-450371.pdf.

[135] J.T. Jayne, D.C. Leard, X. Zhang, P. Davidovits, K.A. Smith, C.E. Kolb, and
D.R. Worsnop, *Development of an aerosol mass spectrometer for size and
composition analysis of submicron particles*. Aerosol Science & Technology, 2000.
33(1-2): p. 49-70.

[136] P. Dawson, *The quadrupole: System design and residual gas analyzer
performance*. Journal of Vacuum Science & Technology A: Vacuum, Surfaces, and
Films, 1986. **4**(3): p. 1709-1714.

[137] Stanford Research Systems. *Models RGA100, RGA200, and RGA300 (Residual
Gas AnalyzerOperating Manual and Programming Reference)*. No date   [cited 2020
July 30]; Available from:
https://www.thinksrs.com/downloads/pdfs/manuals/RGAm.pdf.

[138] General Microtechnology & Photonics. *RGA100, RGA200 and RGA300
Residual Gas Analyzer*. No date   [cited 2020 September 22]; Available from:
https://www.gmp.ch/electronic-instruments/vacuum-analytical/residual-gas-
analyzers/rga100-rga200-and-rga300-residual-gas-analyzer.

[139] R. Kersevan, *Analytical and numerical tools for vacuum systems*. 2007.

[140] Edwards Vacuum. *Edwards nEXT mechanical turbomolecular pumps*. No date
[cited 2020 October 26]; Available from: https://www.edwardsvacuum.com/en/our-
products/turbomolecular-pumps/turbomolecular-pumps.

[141] M. Ady, Monte Carlo simulations of ultra high vacuum and synchrotron
radiation for particle accelerators.

[142] CERN. *About Molflow*. No date   [cited 2020 October 26]; Available from:

https://molflow.web.cern.ch/content/about-molflow.

[143] M. Ady and R. Kersevan. *Molflow user's guide (Version 2.4.1)*. 2014   [cited 2020 November 1]; Available from: https://molflow.web.cern.ch/sites/molflow.web.cern.ch/files/molflow_user_guide.pdf.

[144] M. Ady and R. Kersevan, Introduction to the Latest Version of the Test-particle Monte Carlo Code Molflow+, CERN-ACC-2014-0249, 2014.

[145] R. Kersevan and M. Ady. *Recent Developments of Monte-Carlo Codes Molflow+ and Synrad+*. in *Proc., 10th International Particle Accelerator Conference, Melbourne, Australia*. 2019.

[146] O. Malyshev and K. Middleman, *Test Particle Monte-Carlo modelling of installations for NEG film pumping properties evaluation*. Vacuum, 2009. **83**(6): p. 976-979.

[147] R. Kersevan and J.-L. Pons, *Introduction to MOLFLOW+: New graphical processing unit-based Monte Carlo code for simulating molecular flows and for calculating angular coefficients in the compute unified device architecture environment*. Journal of Vacuum Science & Technology A: Vacuum, Surfaces, and Films, 2009. **27**(4): p. 1017-1023.

[148] R. Kersevan, *Molflow user's guide*. available from one of the authors (RK), 1991.

[149] T.W. Tuer and G.S. Springer, *A test particle Monte Carlo method*. Computers & Fluids, 1973. **1**(4): p. 399-417.

[150] R. Calder and G. Lewin, *Reduction of stainless-steel outgassing in ultra-high vacuum*. British Journal of Applied Physics, 1967. **18**(10): p. 1459.

[151] C.C. Spackman, C.R. Frank, K.C. Picha, and J. Samuel, *3D printing of fiber-reinforced soft composites: Process study and material characterization*. Journal of Manufacturing Processes, 2016. **23**: p. 296-305.

[152] J.R. Vail, B.A. Krick, K.R. Marchman, and W.G. Sawyer, *Polytetrafluoroethylene (PTFE) fiber reinforced polyetheretherketone (PEEK) composites*. Wear, 2011. **270**(11): p. 737-741.

[153] Edwards Vacuum. *nEXT300D Turbomolecular Pump CF100 Inlet Flange, 160W*. No date   [cited 2020 October 26]; Available from: https://shop.edwardsvacuum.com/products/b82200200/view.aspx.

[154] B. Albers and H. Rose, *Nitrogen/helium leak detection used on North Rankin'A'Platform*. The APPEA Journal, 1985. **25**(1): p. 123-128.

[155] K. Zapfe, *Leak detection*. CAS - CERN Accelerator School : Vacuum in Accelerators, 2007: p. 227-240.

[156] B. Gu and X. Huang, *Investigation of leak detection method by means of measuring the pressure increment in vacuum*. Vacuum, 2006. **80**(9): p. 996-1002.

[157] N. Hilleret, Leak detection.

[158] H. Rottländer, W. Umrath, and G. Voss, *Fundamentals of leak detection*. Leybold GMBH (ed) Cat, 2016(199): p. 1-49.

[159] W.G. Bley, *Helium leak detectors: from a laboratory device to dedicated*

industrial leak test units. Vacuum, 1993. **44**(5-7): p. 627-632.

[160] D. Holkeboer, T. Karandy, F. Currier, L. Frees, and R. Ellefson, *Miniature quadrupole residual gas analyzer for process monitoring at milliTorr pressures.* Journal of Vacuum Science & Technology A: Vacuum, Surfaces, and Films, 1998. **16**(3): p. 1157-1162.

[161] O. Malyshev and K. Middleman, *In situ ultrahigh vacuum residual gas analyzer "calibration".* Journal of Vacuum Science & Technology A: Vacuum, Surfaces, and Films, 2008. **26**(6): p. 1474-1479.

[162] W.D. Davis, *Ultrahigh vacuum gauge calibration.* Journal of Vacuum Science and Technology, 1968. **5**(1): p. 23-33.

[163] P. Nash and T. Thompson, *A system for vacuum gauge calibration using the comparison technique.* Journal of Vacuum Science & Technology A: Vacuum, Surfaces, and Films, 1983. **1**(2): p. 172-174.

[164] P. Clausing, *Über die Strahlformung bei der Molekularströmung.* Zeitschrift für Physik, 1930. **66**(7-8): p. 471-476.

[165] W. He, W. Lv, and J. Dickerson, *Gas transport in solid oxide fuel cells*. 2014: Springer.

[166] J.A. Dreyer, N. Riefler, G.R. Pesch, M. Karamehmedović, U. Fritsching, W.Y. Teoh, and L. Mädler, *Simulation of gas diffusion in highly porous nanostructures by direct simulation Monte Carlo.* Chemical Engineering Science, 2014. **105**: p. 69-76.

[167] S. Varoutis, D. Valougeorgis, and F. Sharipov. *Rarefied gas flow through tubes of finite length*. in *AIP Conference Proceedings*. 2008. American Institute of Physics.

[168] V. Titarev, *Rarefied gas flow in a circular pipe of finite length.* Vacuum, 2013. **94**: p. 92-103.

[169] COMSOL, *Introduction to COMSOL multiphysics®.* COMSOL Multiphysics, Burlington, MA, accessed Feb, 1998. **9**: p. 2018.

[170] J. Jin, S. Di, W. Hao, X. Li, X. Wang, and X. Sun, *Process simulation of nano-channel forming by thin film deposition*, in *Journal of Physics: Conference Series*. 2020, IOP Publishing. p. 012023.

[171] COMSOL Multiphysics. *Introduction To Molecular Flow Module*. 2018   [cited 2020 November 6]; Available from: https://doc.comsol.com/5.4/doc/com.comsol.help.molec/IntroductionToMolecularFlowModule.pdf.

[172] COMSOL Multiphysics. *Molecular FLow Module User's Guide*. 2018   [cited 2020 November 6]; Available from: https://doc.comsol.com/5.4/doc/com.comsol.help.molec/MolecularFlowModuleUsersGuide.pdf.

[173] A.W. Thornton, T. Hilder, A.J. Hill, and J.M. Hill, *Predicting gas diffusion regime within pores of different size, shape and composition.* Journal of Membrane Science, 2009. **336**(1-2): p. 101-108.

[174] E. Petersen, *Diffusion in a pore of varying cross section.* AIChE Journal, 1958. **4**(3): p. 343-345.

[175] W. Steckelmacher, *Knudsen flow 75 years on: the current state of the art for*

flow of rarefied gases in tubes and systems. Reports on Progress in Physics, 1986. **49**(10): p. 1083.

[176] M. Knudsen, *Die Gesetze der Molekularströmung und der inneren Reibungsströmung der Gase durch Röhren.* Annalen der Physik, 1909. **333**(1): p. 75-130.

[177] C. Barnatt, *3D Printing.* 2014: ExplainingTheFuture. com Wroclaw, Poland.

[178] H. Lipson and M. Kurman, *Fabricated: The new world of 3D printing.* 2013: John Wiley & Sons.

[179] E. MacDonald and R. Wicker, *Multiprocess 3D printing for increasing component functionality.* Science, 2016. **353**(6307).

[180] J.-Y. Lee, J. An, and C.K. Chua, *Fundamentals and applications of 3D printing for novel materials.* Applied materials today, 2017. **7**: p. 120-133.

[181] T.D. Ngo, A. Kashani, G. Imbalzano, K.T. Nguyen, and D. Hui, *Additive manufacturing (3D printing): A review of materials, methods, applications and challenges.* Composites Part B: Engineering, 2018. **143**: p. 172-196.

[182] J. Delgado, J. Ciurana, and C.A. Rodríguez, *Influence of process parameters on part quality and mechanical properties for DMLS and SLM with iron-based materials.* The International Journal of Advanced Manufacturing Technology, 2012. **60**(5-8): p. 601-610.

[183] B. Redwood, F. Schöffer, and B. Garret, *The 3D printing handbook: technologies, design and applications.* 2017: 3D Hubs.

[184] S. Rahmati, *10.12 - Direct Rapid Tooling*, in *Comprehensive Materials Processing*, S. Hashmi, et al., Editors. 2014, Elsevier: Oxford. p. 303-344.

[185] F. Calignano, D. Manfredi, E. Ambrosio, L. Iuliano, and P. Fino, *Influence of process parameters on surface roughness of aluminum parts produced by DMLS.* The International Journal of Advanced Manufacturing Technology, 2013. **67**(9-12): p. 2743-2751.

[186] P.J. Bártolo, *Stereolithography: materials, processes and applications*. 2011: Springer Science & Business Media.

[187] Formlabs. *Guide to Stereolithography (SLA) 3D Printing*. No date [cited 2021 January 18]; Available from: https://formlabs.com/blog/ultimate-guide-to-stereolithography-sla-3d-printing/.

[188] J.C. Najmon, S. Raeisi, and A. Tovar, *Review of additive manufacturing technologies and applications in the aerospace industry*, in *Additive manufacturing for the aerospace industry*. 2019, Elsevier. p. 7-31.

[189] C.R. Deckard, *Method and apparatus for producing parts by selective sintering*. 1989, Google Patents.

[190] M. Schmid, A. Amado, and K. Wegener. *Polymer powders for selective laser sintering (SLS)*. in *AIP Conference proceedings*. 2015. AIP Publishing LLC.

[191] F. Fina, A. Goyanes, S. Gaisford, and A.W. Basit, *Selective laser sintering (SLS) 3D printing of medicines.* International journal of pharmaceutics, 2017. **529**(1-2): p. 285-293.

[192] J.P. Kruth, P. Mercelis, J. Van Vaerenbergh, L. Froyen, and M. Rombouts, *Binding mechanisms in selective laser sintering and selective laser melting.* Rapid prototyping journal, 2005.

[193] M. Schmidt, D. Pohle, and T. Rechtenwald, *Selective laser sintering of PEEK.* CIRP annals, 2007. **56**(1): p. 205-208.

[194] A.M. D'Altri, S. de Miranda, G. Milani, and G. Castellazzi, *A numerical procedure for the force-displacement description of out-of-plane collapse mechanisms in masonry structures.* Computers & Structures, 2020. **233**: p. 106234.

[195] COMSOL, *LiveLink™ for SolidWorks®.* User's Guide, Version. **4**.

[196] M. Paulic, T. Irgolic, J. Balic, F. Cus, A. Cupar, T. Brajlih, and I. Drstvensek, *Reverse engineering of parts with optical scanning and additive manufacturing.* Procedia Engineering, 2014. **69**: p. 795-803.

[197] The Bartlett workshops. *B-made 3D printing*. No date   [cited 2020 December 28]; Available from: https://www.ucl.ac.uk/bartlett/about-us/our-resources/b-made-bartlett-workshops/b-made-3d-printing.

[198] M. Mao, J. He, X. Li, B. Zhang, Q. Lei, Y. Liu, and D. Li, *The emerging frontiers and applications of high-resolution 3D printing.* Micromachines, 2017. **8**(4): p. 113.

[199] C. May, *Epoxy resins: chemistry and technology*. 2018: Routledge.

[200] L. Zhai, G. Ling, J. Li, and Y. Wang, *The effect of nanoparticles on the adhesion of epoxy adhesive.* Materials Letters, 2006. **60**(25-26): p. 3031-3033.

[201] A. De Morais, A. Pereira, J. Teixeira, and N. Cavaleiro, *Strength of epoxy adhesive-bonded stainless-steel joints.* International journal of adhesion and adhesives, 2007. **27**(8): p. 679-686.

[202] A.M. Glauert and R. Glauert, *Araldite as an embedding medium for electron microscopy.* The Journal of biophysical and biochemical cytology, 1958. **4**(2): p. 191-194.

[203] Farnell. *Araldite® 2020 (XW 396 / XW 397)*. No date   [cited 2021 January 10]; Available from: http://www.farnell.com/datasheets/1640467.pdf?_ga=2.73488404.723075601.156526 1557-238420828.1565261557.

[204] A. Ghumatkar, S. Budhe, R. Sekhar, M. Banea, and S.d. Barros, *Influence of adherend surface roughness on the adhesive bond strength.* Latin American Journal of Solids and Structures, 2016. **13**(13): p. 2356-2370.

[205] L. Ouyang, J.P. Armstrong, Q. Chen, Y. Lin, and M.M. Stevens, *Void-free 3d bioprinting for in situ endothelialization and microfluidic perfusion.* Advanced functional materials, 2020. **30**(1): p. 1908349.

[206] B. Halliday, *An introduction to materials for use in vacuum.* Vacuum, 1987. **37**(8-9): p. 583-585.

[207] A.P. Povilus, C.J. Wurden, Z. Vendeiro, M. Baquero-Ruiz, and J. Fajans, *Vacuum compatibility of 3D-printed materials.* Journal of Vacuum Science & Technology A: Vacuum, Surfaces, and Films, 2014. **32**(3): p. 033001.

[208] W. Lindquist and A. Venkatarangan, *Investigating 3D geometry of porous media*

from high resolution images. Physics and Chemistry of the Earth, Part A: Solid Earth and Geodesy, 1999. **24**(7): p. 593-599.

[209] R. Melnikova, A. Ehrmann, and K. Finsterbusch. *3D printing of textile-based structures by Fused Deposition Modelling (FDM) with different polymer materials*. in *IOP conference series: materials science and engineering*. 2014. IOP publishing.

[210] F. Paolucci, G.W. Peters, and L.E. Govaert, *Plasticity-controlled failure of sintered and molded polyamide 12: Influence of temperature and water absorption.* Journal of Applied Polymer Science, 2020. **137**(14): p. 48525.

[211] G. Flodberg, H. Pettersson, and L. Yang, *Pore analysis and mechanical performance of selective laser sintered objects.* Additive Manufacturing, 2018. **24**: p. 307-315.

[212] M. Wyzgoski, G. Novak, and D. Simon, *Fatigue fracture of nylon polymers.* Journal of Materials Science, 1990. **25**(10): p. 4501-4510.

[213] P. Liu and K. Liang, *Review Functional materials of porous metals made by P/M, electroplating and some other techniques.* Journal of materials science, 2001. **36**(21): p. 5059-5072.

[214] C. Elliott, V. Vijayakumar, W. Zink, and R. Hansen, *National instruments LabVIEW: a programming environment for laboratory automation and measurement.* JALA: Journal of the Association for Laboratory Automation, 2007. **12**(1): p. 17-24.

[215] EOS. *FORMIGA P 100.* [cited 2021 January 3]; Available from: https://rpl.mechse.illinois.edu/img/printers/sls.pdf.